Research on the fabrication of three-dimensional periodic nanostructure in solution-derived semiconductor materials toward lowering of thermal conductivity

低熱伝導率化に向けた 塗布型半導体材料内への 三次元周期的ナノ構造形成に関する研究

January 2021

Xudongfang Wang

Program of Materials Science and Engineering
Graduate School of Science and Technology
Nara Institute of Science and Technology

Table of Contents

Chapter.1 Introduction 6

1.1 Current situation of global energy 6

1.2 Thermoelectric devices 9

1.2.1 Introduction of thermoelectric effect 9

1.2.2 Different structures of the TEGs 10

1.2.3 The thermoelectric figure of merit 13

1.3 Nanostructure thermal conduction 14

1.3.1 High porosity 3D nanostructures 16

1.3.2 Phononic crystal 18

1.4 Laser process technologies for the fabrication of 3D periodic nanostructures 19

1.5 Purpose of this study 23

References 25

Chapter.2 Fabrication of 3D periodic nanostructures 33

2.1 Proximity nanopatterning process (PnP) 33

2.1.1 Mechanism of PnP process 34

2.1.2 Photoresist 36

2.1.3 Polydimethylsiloxane (PDMS) phase shift mask (PSM) 37

2.1.4 Construction of laser irradiation (exposure) system 39

2.1.5 The procedures of PnP process 43

2.2 3D periodic nanostructures fabricated by PnP process with KMPR 45

2.2.1 Fabrication procedures of KMPR nanostructure 45

2.2.2 Surface uniformity of photoresist 47

2.2.3 Effects of different soft-bake conditions 49

2.2.4 Effects of different UV exposure conditions 51

2.2.5 Reproducibility of KMPR 3D nanostructures 55

2.3 3D periodic nanostructures fabricated by PnP process with SU8 57

2.3.1 Fabrication procedures of SU8 nanostructure 57

2.3.2 Effects of different soft-bake conditions 58

2.3.3 Effects of different UV exposure conditions 60

2.3.4 Reproducibility of SU8 3D nanostructures 64

2.4 KMPR & SU8 3D nanostructures investigation and comparison 66

2.4.1 Talbot distance 66

2.4.2 The height and periodicity of the nanostructures 69

2.5 Summary 73

References 74

Chapter.3 Fabrication of 3D periodic ZnO nanostructure via infiltration process 77

3.1 Introduction 77

3.2 Fabrication of 3D periodic ZnO nanostructure via infiltration process 80

3.2.1 Fabrication procedures of 3D periodic ZnO nanostructure 80

3.2.2 Reproducibility of ZnO 3D inverse nanostructure 82

3.2.3 Optimization of infiltration process by usingSU8 template 85

3.2.4 Optimization of infiltration process by using KMPR template 93

3.3 Characteristics of 3D periodic ZnO nanostructure 95

3.3.1 Comparison between calculation of shrinkage rate by structural size evaluation and theoretical calculation 95

3.3.2 Crystallographic analysis of ZnO nanostructure by XRD 100

3.4 Summary 103

References 105

Chapter.4 Fabrication of 3D periodic a-Si:H nanostructure via infiltration process 108

4.1 Introduction 108

4.2 Fabrication of 3D periodic a-Si:H nanostructure via infiltration process 109

4.2.1 Fabrication of the a-Si:H film by a solution-derived silicon 109

4.2.2 Fabrication procedures of 3D periodic a-Si:H nanostructure 112

4.2.3 Fabrication of 3D periodic a-Si:H nanostructure with KMPR template 115

4.2.4 Fabrication of 3D periodic a-Si:H nanostructure with SU8 template 121

4.2.5 Reproducibility of the a-Si:H 3D nanostructures 125

4.3 Characteristics of 3D periodic a-Si:H nanostructure 126

4.3.1 Comparison between calculation of shrinkage rate by structural size evaluation and theoretical calculation 126

4.3.2 Crystallographic analysis of a-Si:H nanostructure by XRD.................................... 128

4.4 Summary 130

References 132

Chapter.5 Characteristics of the ZnO and a-Si:H 3D nanostructures 134

5.1 Optical characteristics of the ZnO and a-Si:H 3D nanostructures 134

5.1.1 Reflectance and transmittance of the ZnO 3D nanostructures 134

5.1.2 Reflectance and transmittance of the a-Si:H 3D nanostructures 135

5.2 Seebeck coefficient and electric conductivity of the ZnO and a-Si:H 3D nanostructures 136

5.2.1 Evaluation methodology 136

5.2.2 Preparation of the electrodes 138

5.2.3 Seebeck coefficient and electric conductivity of the ZnO 3D nanostructure 139

5.2.4 Seebeck coefficient and electric conductivity of the a-Si:H 3D nanostructure 142

5.3 Thermal conductivity of the ZnO 3D nanostructures 144

5.3.1 Effective thermal conductivity simulation by COMSOL 144

5.3.2 Evaluation methodology of thermal conductivity 147

5.3.3 Mechanism and implementation of 3ω method 149

5.3.4 Preparation of the electrodes on the ZnO 3D nanostructures 151

5.4 Summary 156

References 157

Chapter.6 Conclusions and future works 159

6.1 Conclusions 159

6.2 Suggestions for future works 161

List of publications 165

Acknowledgement 168

Chapter.1 Introduction

1.1 Current situation of global energy

With the rapid development of the technology and society, the requirement for energy is also swiftly increasing. Although fossil resources' reserves are slowly increasing every year, however, as time goes by, fossil resources will slowly be depleted. Moreover, the current situation still cannot achieve 100% utilization efficiency in the use of fossil resources, which means that the actual use of fossil resources is far shorter than estimated.

BP's statistical review of world energy of 2016 gave estimated remaining years of fossil resources as seen in Fig. 1.1 [1], which is foreseeable that it will be exhausted soon. Therefore, renewable energy, which collected energy from renewable resources such as sunlight, rain, wind, and geothermal heat, is crucial.

Starting from the first oil shock in 1973, people began to pay more

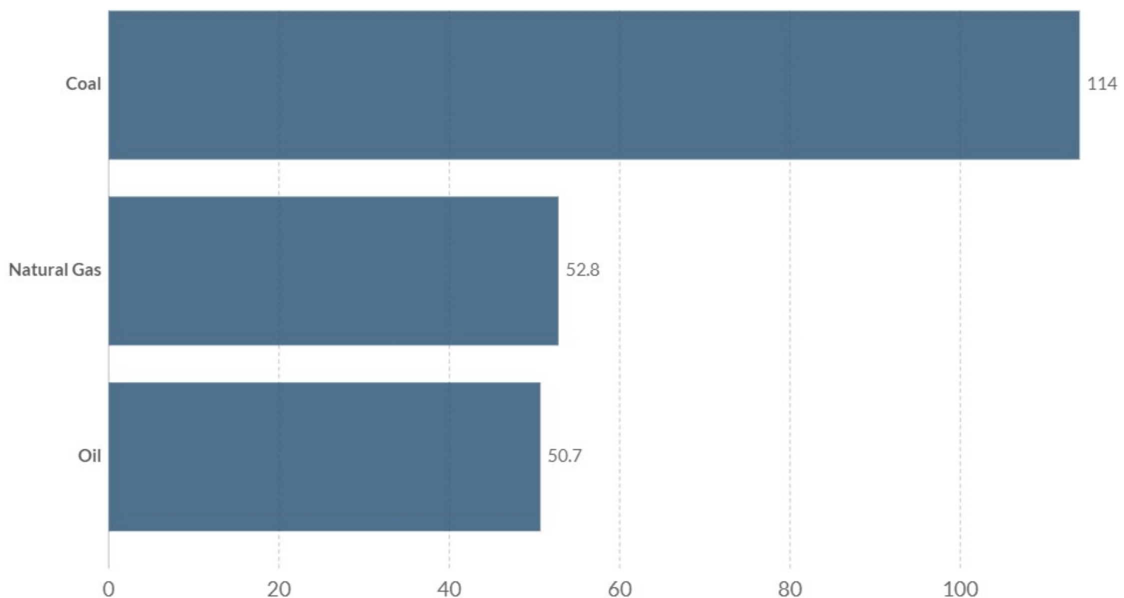

Figure 1.1 Years of global coal, oil and natural gas left [1].

attention to low-carbon energy, nuclear energy and various renewable energies. The wind energy and solar energy can reach a share of about 20% from 2010 (Fig. 1.2).

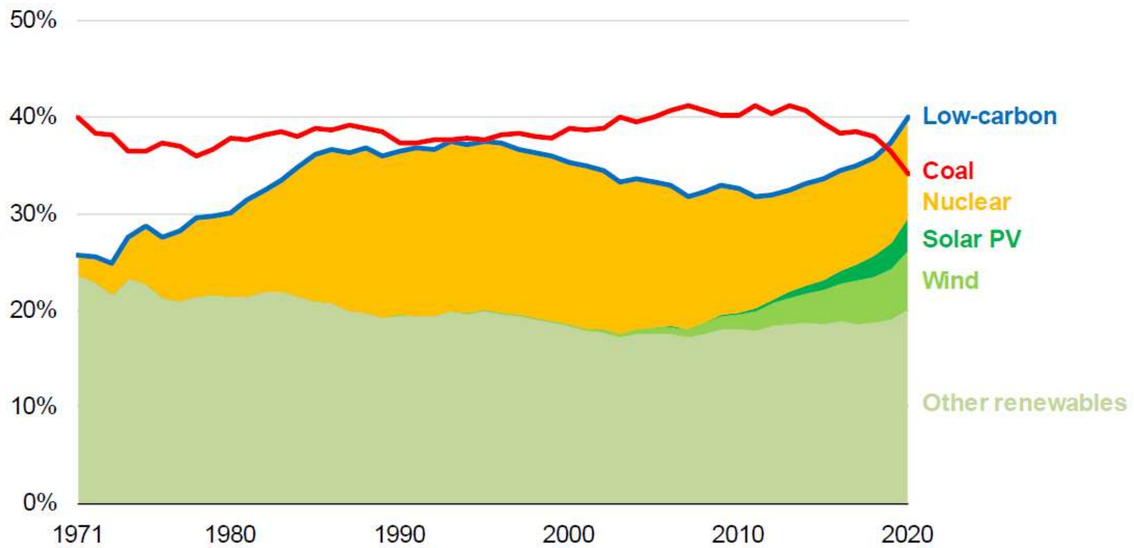

Figure 1.2 Global generation shares from coal and low-carbon energy, 1971-2020 [2].

A concept called energy harvesting has caught the eye of researchers as a means of utilizing renewable energy. Energy harvesting derived energy from external sources such as thermal energy, solar power, and wind energy. It can work as a power supply for small, wireless, wearable autonomous devices.

Energy is commonly used in our everyday life; a common example is a fossil fuel power station that generates electricity by burning fossil fuels. In connection to this, due to the second law of thermodynamics, the conversion efficiency is limited. All processes or machines that use energy will produce a surplus of heat called waste heat or “secondary heat.” This comes from all manner of human activities, natural system, and all organisms. As a consequence, it is often released into the environment. Research has already discussed the quantification of global waste heat, and after energy

conversion, 72% of primary energy consumption is lost. Among these losses, electricity generation accounts for the largest share, followed by transportation and industry [3]. The high-temperature waste heat can be pragmatic to use in the current situation, due to the energy is highly concentrated in a small range.

Nevertheless, the waste heat lower than 100°C has the largest share compared to medium (100 – 299 °C) and high temperature (≥ 300°C) [4]. Thus, it is crucial to find some methods that can take advantage of those waste heat.

Converting waste heat directly into electricity is a simple and effective method to transfer waste heat (which also means thermal energy) to electricity. Two mainstream methods have been adopted in recent decades. The first one is the organic Rankine cycle which can convert low-temperature heat into useful work, and itself can be transformed into electricity at the same time [5]. Thermoelectric generators (TEGs) as one kind of thermoelectric devices, are another well-known approach that can generate a voltage from temperature difference through the Seebeck effect phenomenon. Some applications already has existed which can utilize this kind of waste heat, such as satellites, thermal energy storage tower, camp-stove charges and body temperature power watch as shown in Fig. 1.3(a-d) [6–10]. However, due to low conversion efficiency, large-scale applications are still an enormous challenge.

Figure 1.3 TEGs with different applications [6−10].

1.2 Thermoelectric devices

1.2.1 Introduction of thermoelectric effect

Nowadays thermoelectric (TE) materials can be used as coolers, heaters, and generators, which are from the study of the thermoelectric effects. It includes three separately effects: Seebeck effect, the Peltier effect, and the Thomason effect. The Seebeck effect is the start of the thermoelectric effect from 1821 when Thomas Johann Seebeck found that a voltage will be produces when a temperature gradient is formed between two different conductors. It is due to the accumulation of the charge carriers, which

because of that, charge carriers will migrate from high to low temperature with a temperature gradient. On the contrary, the heat flow generated by the electrical current is called the Peltier effect [11–13]. As aforementioned, TEGs are the most promising devices that can convert waste heat into electricity, which takes advantage of the Seebeck effect. Therefore, this study concentrates on the Seebeck effect. And the schematic and general structure are shown in Fig. 1.4.

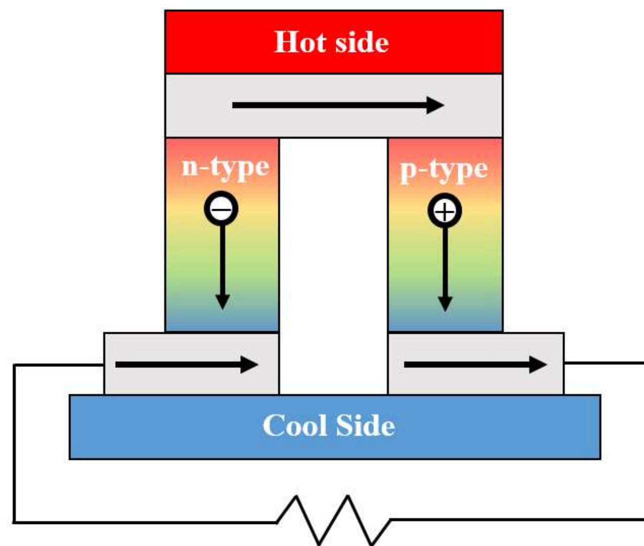

Figure 1.4 π structure of TE device.

1.2.2 Different structures of the TEGs

The different structures of the TEGs will greatly affect its performance, such as the electrical, thermal, and power generation characteristics. Therefore, the TEGs have the following constructs:

① Bulk-type TEGs: The bulk-type TEGs are normally composed of p-type and n-type semiconductor materials, which employ the longitudinal Seebeck effect for high power generation [14]. Generally, the efficiency

of the bulk-type TEGs will be improved by geometric factors, the shape, and the number of TE legs. It can already generate 1kW power from experiments [15–18]. (Fig. 1.5)

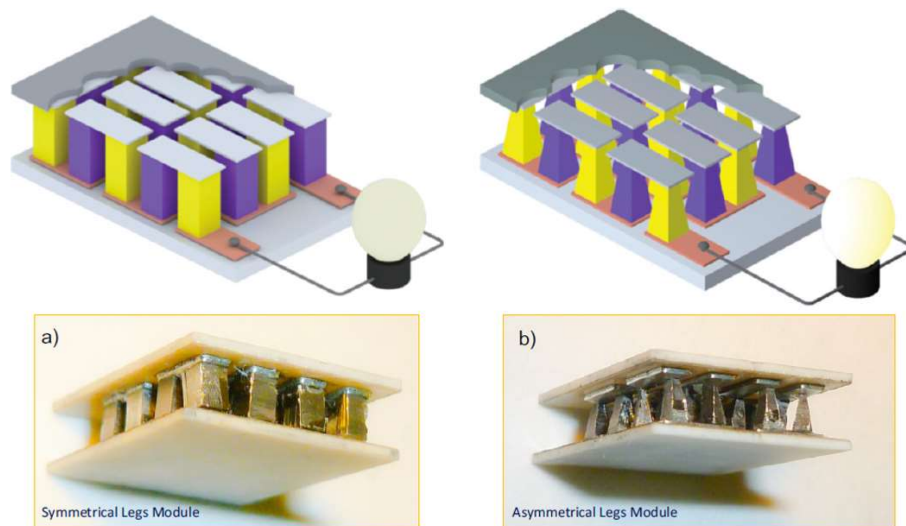

Figure 1.5 Bulk-type TEGs [14,17].

② Cylindrical Bulk-type TEGs: The cylindrical bulk-type TEGs have a radial direction of heat flow, which are very useful for special occasions such as automotive exhaust pipes, oil pipelines, and cooling channels. These TEGs are always fabricated via a sintering process that requires the isolation layers, metallization layers, and p-type (n-type) semiconductor materials [19–21]. In recent years, it has been applied in the automotive field to convert waste heat, and the maximum power can reach approximately 2 kW [22]. (Fig. 1.6)

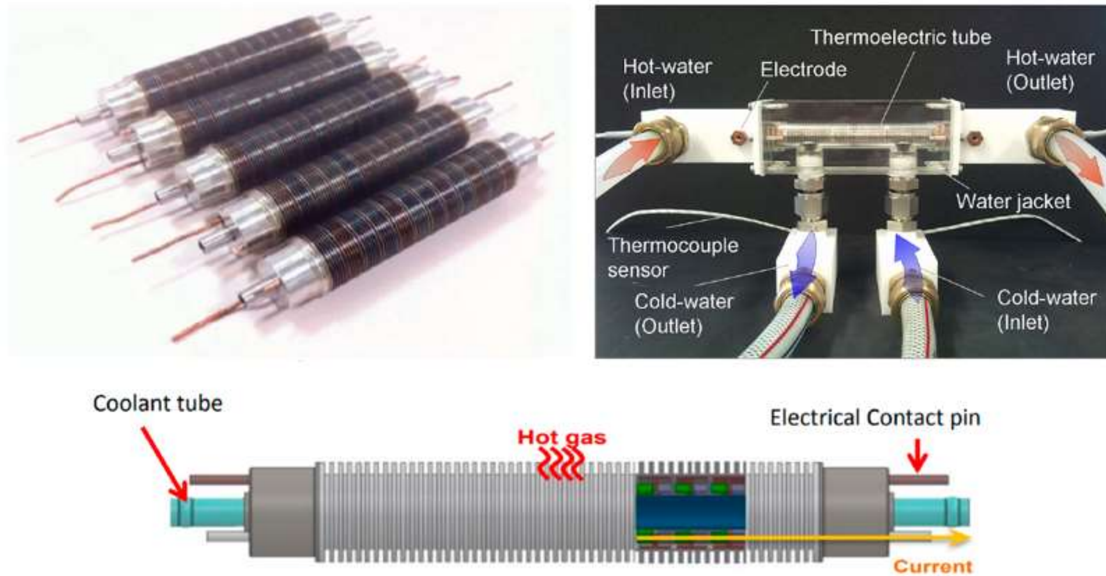

Figure 1.6 Cylindrical Bulk-type TEGs [19–21].

③ Thin film-type (Flexible-type) TEGs: The thin film-type TEGs possess a high heat flux that can obtain the high densities of cooling power. The flexible-type in thin film-type TEGs attract the attentions of many researchers due to a high requirement for flexible power supplies, which are beneficial for wearable sensors. Different from the conventional fabricate methods, the flexible-type TEGs employ novel manufacturing

Figure 1.7 Thin film-type (Flexible-type) TEGs [23,24].

methods such as printing and thermal spraying by using innovative polymers and composites [23–27]. (Fig. 1.7) However, large-scale applications have not been realized primarily due to low efficiencies. Therefore, this research aims to improve the efficiency of the micron scale thin-film materials.

1.2.3 The thermoelectric figure of merit

Thermoelectric figure-of-merit (*ZT*) is an element that determines the maximum efficiency of a thermoelectric material as shown in Eq. 1.1:

$$ZT = (S^2\sigma/\kappa)T \tag{1.1}$$

where S is the Seebeck coefficient, σ is the electric conductivity, κ is the thermal conductivity, and T is temperature. Additionally, power factor *(PF*) in Eq. 1.2:

$$PF = S^2\sigma \tag{1.2}$$

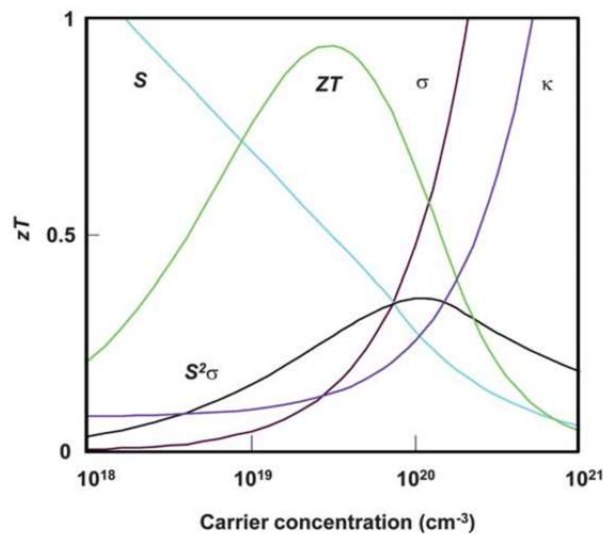

Figure 1.8 Interdependence of the S, σ and κ [28].

also claims the ability of energy generation for a TE device. However, those parameters are both related with carrier concentration as shown in Fig. 1.8 [28]. Electric conductivity and Seebeck coefficient are positive and inversely proportional to carrier concentration, respectively, which means that after optimization, the maximum *PF* can be obtained. For thermal conductivity (κ), it has two main elements: electron thermal conductivity and lattice thermal conductivity (Eq. 1.3).

$$\kappa = \kappa_{electron} + \kappa_{lattice} \tag{1.3}$$

From the Wiedemann-Franz law, the electron thermal conductivity is positively correlated with the carrier concentration as well (Eq. 1.4).

$$\kappa_{electron} = LT\sigma \tag{1.4}$$

Where L is the Lorenz number, T is temperature, σ is the electrical conductivity. Therefore, reducing $\kappa_{lattice}$ is becoming critical.

1.3 Nanostructure thermal conduction

In recent years, nanostructures have attracted the attention of many researchers due its ability to greatly reduce $\kappa_{lattice}$. The reason why these nanostructures can lower the $\kappa_{lattice}$ is because the spacing between material boundaries is small. When the material boundary intervals are smaller than the mean free path (MFP) of generated phonons (quantized lattice vibrations, which are thermal carriers), it will collide with the barrier, which causes scattering and hindering thermal carrier propagation. After scattering, the phonons are mirror-reflected or energetically split into multiple phonons with low frequencies and act as thermal carriers again. As

a result, phonons with a longer MFP than bulk materials will be the thermal carriers, which will be trapped in the nanostructure again, therefore reducing the $\kappa_{lattice}$.

Compared to bulk materials in TEGs, which have the same chemical composition, nanostructured materials can achieve higher power factors [29]. It is because the quantum confinement effect in nanostructures is helpful in increasing the *PF*, as well as the different scattering lengths which are beneficial for decreasing $\kappa_{lattice}$ [30-32]. Here are some examples with different dimensions that have been widely used:

① One-dimension (1D): Nanowires and nanotubes [33–36],

② Two-dimension (2D): Nanosheet [37], graphene [38,39], transition metal dichalcogenides (TMDCs) [40], black phosphorus (BP) [41], and nano-composites [42–46],

③ Three-dimension (3D): Superlattices [47,48], 3D structure assembled by nanowire arrays [49], random porous structures [50–53], uniform patterning porous nanostructures (3D periodic nanostructure) [54–56].

As a summary in Fig. 1.9, all of those nanostructures can have higher *ZT*, especially in high porosity, 3D nanostructures. In addition, the phononic crystal, which can significantly reduce the $\kappa_{lattice}$ is also another approach that can be expected [57].

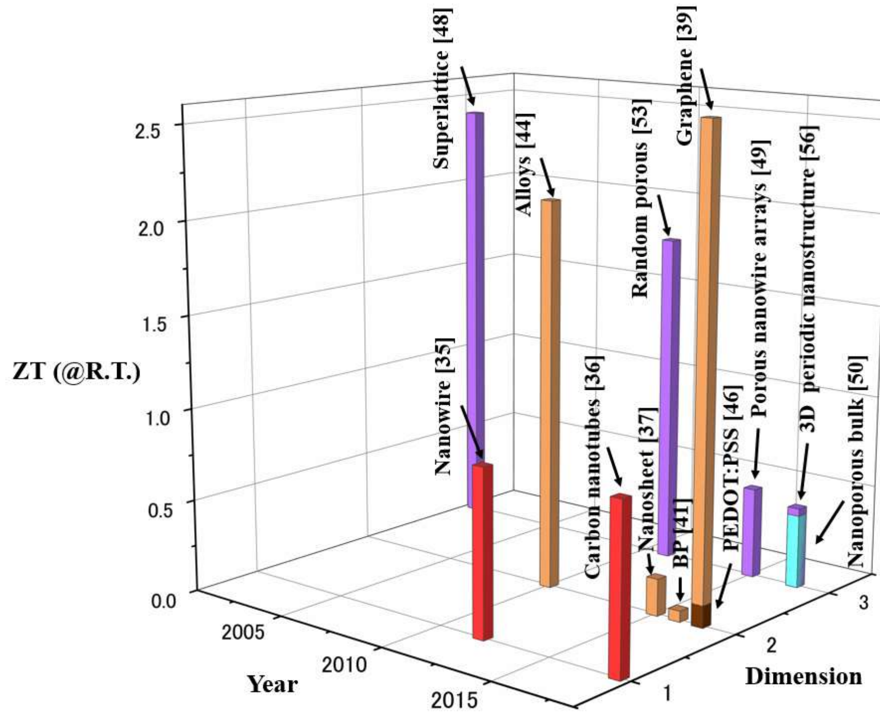

Figure 1.9 Summary of relatively high ZT in recent years with different dimensions.

1.3.1 High porosity 3D nanostructures

The 3D porous nanostructures can easily increase the porosity by increasing the thickness. These structures also have larger cross-sectional areas (A) which will contribute to the enhancement of the heat flow and charge generation. Moreover, the temperature gradient required for thermoelectric power generation is also related to A. The 3D nanostructures with high porosity can greatly enhance the effective A, which can also decrease the κ with increasing porosity as shown in Fig. 1.10 [58]. The reason why the κ decreases with increasing porosity is due to the increased frequency of phonon boundary scattering at the porous nanostructure interface. However, the problem is that as the porosity increases, the σ will

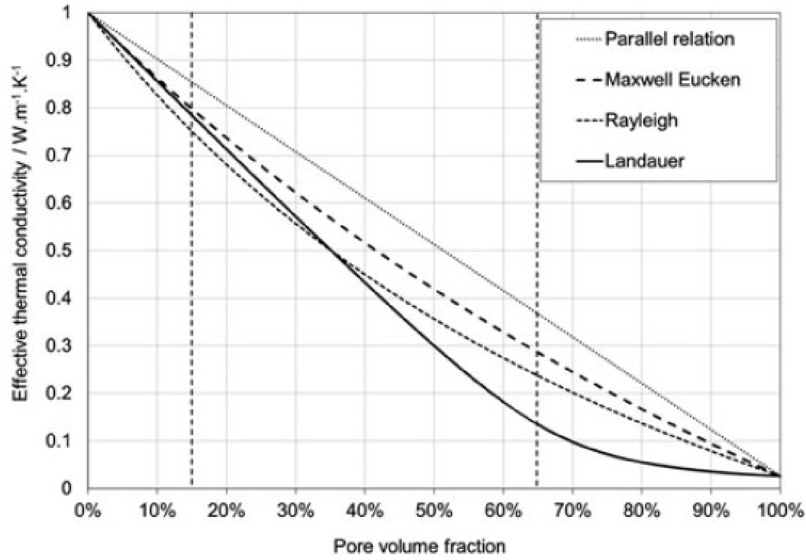

Figure 1.10 The relationship between effective thermal conductivity and pore volume fraction (Porosity) [58].

also decrease. Therefore, in order to solve this problem, it is conceivable to suppress the decrease in σ. Another approach is to reduce the κ more than the σ by interface scattering. Furthermore, increasing the S more than decreasing the σ via quantum confinement is another approach. There are also reports that the use of continuous, periodic, and uniform structures in 3D materials prevents the decrease in electrical conductivity. The 3D nanostructures developed with monolithic $Bi_{1.5}Sb_{0.5}Te_3$ ternary alloys in this reference can maintain the transports of electrons due to the size of the thermoelectric struts in the structural unit cell that is larger (> 140 nm) than the MFP of electrons which generally in the range of 40 nm – 60 nm [55].

Therefore, to suppress the decrease in σ, the size of the formed 3D nanostructures should be larger than the MFP of the electrons. Congruently, if the size of the nanostructure smaller than the MFP of the phonons, then the $\kappa_{lattice}$ is reduced and the ZT of the nanostructure can be considered as the highest.

1.3.2 Phononic crystal

The phonon propagation – which also means quanta of lattice vibrations – can be controlled through an artificial periodic structure called a phononic crystal (PnC). PnCs are nanostructures with highly ordered periodicity; it can control the heat flow by forming a new phonon band. In PnCs, the main heat conduction is coherent which is caused by the inherent wave nature of phonons [59]. There are various device application examples using PnCs as shown in Fig. 1.11 [60].

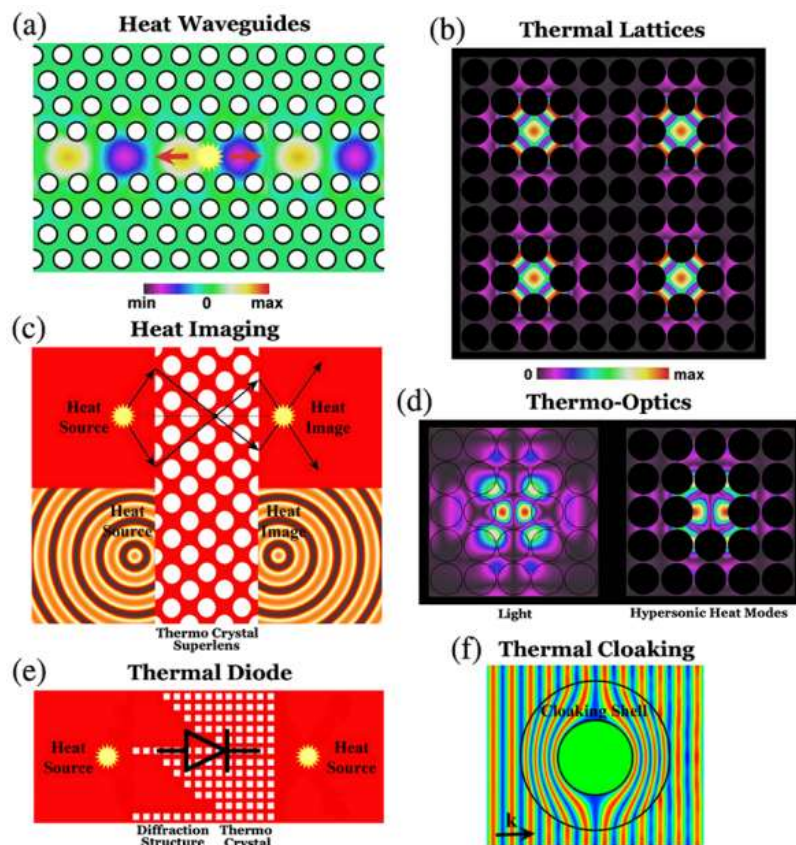

Figure 1.11 Different applications of PnC [60].

Because PnCs can affect phonons the same way that photons are controlled by photonic crystal, PnCs have received a lot of attention in the

applications for thermoelectric conversion [57, 61–69]. It is because phonons' contribution to the lattice thermal conductivity is described by the following formula: (Eq. 1.5)

$$\kappa_{lattice} = \frac{1}{3}\int_0^{\theta_D/T} C(x) v l(x) dx \quad (1.5)$$

Where θ_D is the Debye temperature, $C(x)$ is the specific heat for phonons at frequency x, v is the group velocity of phonons, $l(x)$ is the MFP for phonons at frequency x. This is based on the Debye approximation that fits acoustic phonon modes by ignoring the optical phonon mode, which has minute contributions to thermal conductivity due to the low group velocity. The principle of reducing the $\kappa_{lattice}$ by PnCs is that the design of the PnCs periodicity can cause phonon band folding so that the band becomes flat, therefore reducing the phonon group velocity, and creating a bandgap. It has also been reported that the introduction of PnCs can result in a significant reduction in $\kappa_{lattice}$ without significantly affecting *PF*. This is because the MFPs of phonons is generally lower than that of electronic MFPs [69]. When the PnCs were designed with 3D nanostructures, the group velocity of phonons can be further reduced due to the existence of the multilayer structures, thereby greatly reducing the $\kappa_{lattice}$. Therefore, the applications of PnC in thermoelectric filed will become extremely vital in future research.

1.4 Laser process technologies for the fabrication of 3D periodic nanostructures

As mentioned, the high porosity 3D nanostructure with periodic patterns

will be the best way to improve the *ZT* of the thermoelectric devices. However, the traditional manufacturing process always requires high vacuum, high pressure, and high temperature such as electron beam lithography, atomic layer deposition and reactive ion etching [70–72]. This is an urgent problem to be solved as these processes incur significant production time and overhead costs. In this section, the fabrication process of 3D periodic nanostructures by laser process through a non-vacuum system is briefly described below:

① The direct laser drawing method:

The direct laser drawing method is a laser process which directly draws a preferred structure on a photoresist. [73–77] Moreover, it has a high degree of freedom in design that can use ink materials and inorganic materials based on photosensitive materials as precursors that form a 3D structure [78–81]. The problem is that the large-scale patterning is almost impossible due to the limitations of the equipment (Fig. 1.12).

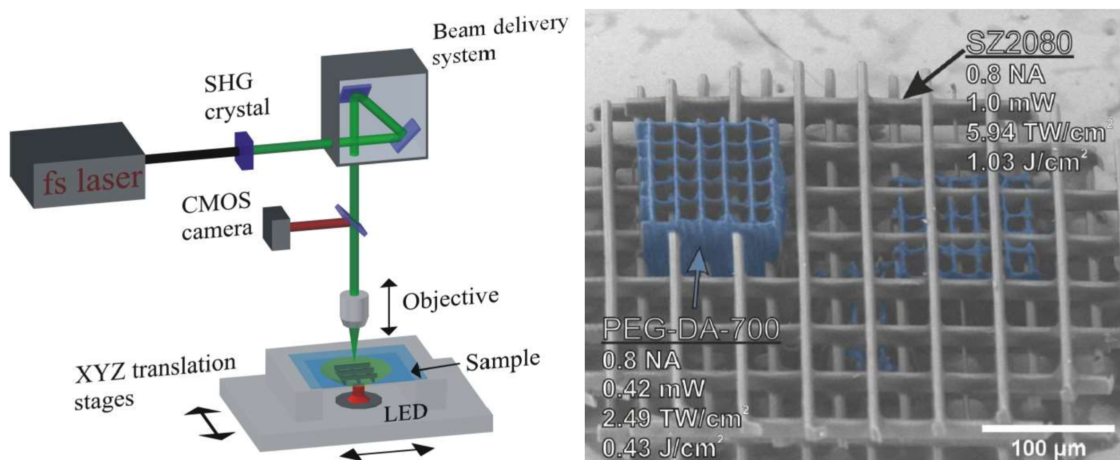

Figure 1.12 The direct laser drawing method [77].

② Interference lithography:

Interference lithography is a single laser irradiation process that uses

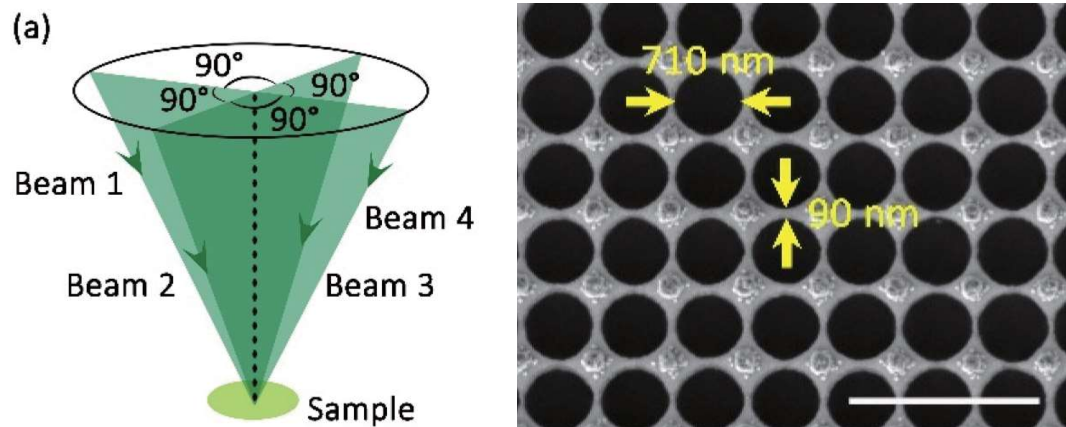

Figure 1.13 Interference lithography [87].

complicated and precise optical systems. The periodic structure will be produced through an interference pattern inside a photoresist, which comes from the multiple laser beams' interferences by using a beam splitter (Fig. 1.13) [82–87].

③ Phase shift lithography

Phase shift lithography is interference lithography which generates a 3D periodic structure through a phase shift mask (PSM). Generally, the self-assembly of colloidal particles arranged two dimensionally on the photoresist's surface acts as a PSM to generate a 3D periodic structure. Nevertheless, this kind of structures is limited due to the diameter, period, and arrangement of the colloidal particles, resulting in a high probability of producing defects in crystal structure and cracks [88–91] (Fig. 1.14).

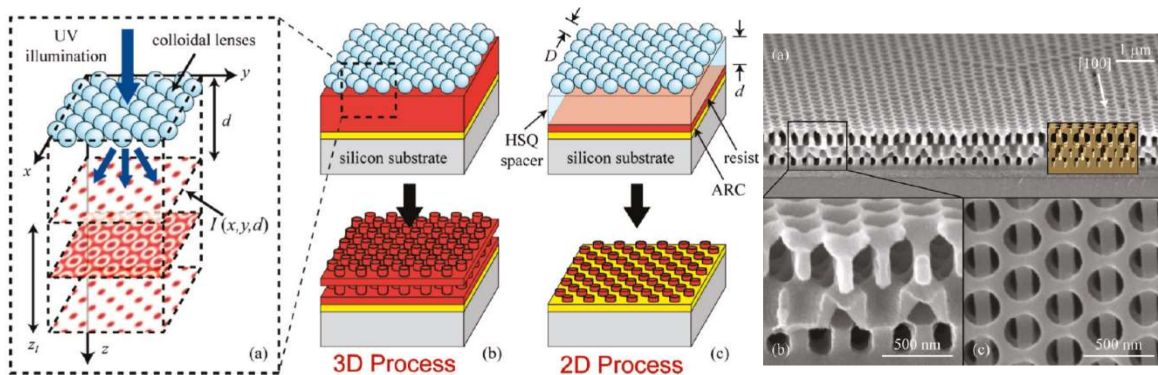

Figure 1.14 Phase shift lithography [88].

The methods described above can make high porosity 3D periodic nanostructures relatively simple, but also have corresponding shortcomings. Proximity field nanopattering (PnP) is one kind of phase shift lithography process which can form high porosity 3D nanostructures by generating a light intensity distribution via 3D diffraction of incident light on a photoresist through a PSM with periodic 2D patterns. At the same time, the periodic 2D patterns on the PSM can improve the design freedom of the 3D structure by adjusting the patterns and ensuring the high integrity of the formed structure by changing the mask regularly. After that, the fabricated 3D nanostructure is used as a template, and a non-vacuum penetration process using a solution-derived semiconductor material is introduced to fill the template. After filling, removal of the template allows the formation of 3D inverse nanostructure of the semiconductor material. This not only reduces the power consumption of the manufacturing process, but also reduces the manufacturing cost, shortens the process time, and simplifies the maintaining. Therefore, it is considered a low-cost and non-vacuum method to fabricate 3D periodic nanostructures with a high degree of freedom.

1.5 Purpose of this study

This study focuses on a 3D periodic nanostructure that can maintain high levels of *PF* and lower the κ by adjusting the size of the nanostructure within a specific range. The solution-derived semiconductor materials penetrates a highly uniform and porous 3D nanostructure fabricated by a non-vacuum process so as to create a 3D inverse nanostructure. This process aims to break the mutual restriction between the key factors and improve the *ZT* of the thermoelectric materials by using high porosity 3D periodic nanostructures. The following four themes were taken up as research themes for achieving this main purpose, and minor purposes were set for each subject as well:

① Fabrication of 3D periodic nanostructure template by non-vacuum process.

A 3D periodic nanostructure prepared by a photoresist was used as a template to fill the solution-derived semiconductor materials, so as to form a 3D inverse nanostructure. For template fabrication the laser system was constructed, and the fabrication process was optimized first.

② Optimization and evaluation of 3D periodic nanostructures with solution-derived ZnO.

The repetitive verification of the previous process was carried out and the infiltration process was optimized. After that, the ZnO 3D periodic nanostructure was repeatedly produced under different ZnO concentrations. Furthermore, the structure size and crystallinity of the

obtained nanostructure were evaluated.

③ Fabrication and evaluation of 3D periodic nanostructure with solution-derived Silicon.

The same infiltration process was performed on a 3D template of the photoresist for the purpose of fabricating a a-Si:H 3D periodic nanostructure to confirm if this method is equally applicable to other materials. The structure size evaluation and crystallinity analysis were carried out similar to the previous section.

④ Characterization of the prepared ZnO and Si periodic nanostructures.

The optical (reflectance and transmittance) and thermoelectric (S and σ) properties of the prepared ZnO and Si 3D periodic nanostructures were evaluated.

References

[1] Statistical Review of World Energy 2016, BP, http:// https://ourworldindata.org/how-long-before-we-run-out-of-fossil-fuels.

[2] Global Energy Review 2020, IEA, http:// https://www.iea.org/reports/global-energy-review-2020.

[3] C. Forman, I. K. Muritala, R. Pardemann, and B. Meyer, Renewable and Sustainable Energy Reviews., 57, 1568 (2016).

[4] A. Firth, B. Zhang, and A. Yang, Applied Energy., 235, 1314 (2019).

[5] Harry Zvi Tabor, Cleveland Cutler, Encyclopedia of the Earth, 2007.

[6] A 3D model of NASA's New Horizons, a mission to Pluto and the Kuiper Belt, http://pluto.jhuapl.edu.

[7] M. V. Lukowica, E. Abbe, T. Schmiel, and M. Tajmar, Energies., 9, 541 (2016).

[8] Sustainability and Outstanding architecture: Bolzano's new thermal storage tower, http://atzwanger.net/en/news.

[9] CampStove 2, http://bioliteenergy.jp.

[10] PowerWatch, http://powerwatch.com.

[11] V. Alessandro, Annals of Chemistry and Natural History., 5, 132 (1794).

[12] T. J. Seebeck, Abhandlungen der Koniglichen Akademie der Wissenschaften zu Berlin (In German)., 265 (1822).

[13] J. C. A. Peltier, Annales de Chimie et de Physique (in French)., 56, 371 (1834).

[14] K. Uchida, M. Ishida, T. Kikkawa, A. Kirihara, T. Murakami, and E.

Saitoh, J. Phys. Condens. Matter., 26, 343202 (2014).

[15] H. Fateh, C. A. Baker, M. J. Hall, and L. Shi, Appl. Energy., 129, 373 (2014).

[16] M. Hodes, IEEE Trans. Compn. Packag. Technol., 33, 307 (2010).

[17] A. F. –Mijangos, G. Min, and J. A. –Quintana, Energy Convers. Manag., 148, 1372 (2017).

[18] Y. Kishita, Y. Ohishi, M. Uwasu, M.Kuroda, H. Takeda, and K. Hara, J. Clean. Pord., 126, 607 (2016).

[19] A. Schmitz, C. Stiewe, and E. Muller, J. Electron. Mater., 42, 1702 (2013).

[20] G. Min, and D. M. Rowe, Semicond. Sci. Technol., 22, 880 (2007).

[21] K. Takahashi, T. Kanno, A. Sakai, H. Tamaki, H. Kusada, and Y. Yamada, Science Reports., 3, 1501 (2013).

[22] V. Jovovic, Thermoelectric Waste Heat Recovery Program for Passenger Vehicles; Gentherm Incorporated: Azusa, CA, USA, 2015.

[23] M. Uenuma, K. Umeda, J. Felizco, D. Senaha, and Y. Uraoka, Journal of Electronic Materials., 48, 6 (2018).

[24] K. K. Jung, Y. Jung, C. J. Choi, J. M. Lee, and J. S. Ko, Current Applied Physics., 16, 1442 (2016).

[25] J. Weber, K. P. –Kamloth, F. Haase, P. Detemple, F. Volklein, and T. Doll, Sens. Actuators A Phys., 132, 325 (2006).

[26] S. Jo, M. Kim, M. Kim, and, Y. Kim, Electron. Lett., 48, 16 (2012).

[27] J. P. Rojas, D. Conchouso, A. Arevalo, D. Singh, I. G. Foulds, and M. M. Hussain, Nano Energy., 31, 296 (2017).

[28] J. R. Szczech, J. M. Higgins, and S. Jin, J. Mater. Chem., 21, 4037 (2011).

[29] M. Y. Tang, and M. S. Dresselhaus, MRS Proc., 886, 0886-F01-01 (2005).

[30] G. J. Snyder, and E. S. Toberer, Nat. Mater., 7, 105 (2008).

[31] M. S. Dresselhaus, G. Chen, M. Y. Tang, R. G. Yang, H. Lee, D. Z. Wang, Z. F. Ren, J. P. Fleurial, and P. Gogna, Adv. Mater., 19, 1043 (2007).

[32] G. Chen, Phys. Rev. B., 57, 23, 14958 (1998).

[33] A. I. Hochbaum, R. Chen, R. D. Delgado, W. Liang, E. C. Garnett, M. Najarian, A. Majumdar, and P. Yang, Nature., 451, 163 (2008).

[34] A. I Boukai, Y. Bunimovich, J. T. –Kheli, J. –K. Yu, W. A. Goddard III, and J. R. Heath, Nature., 451,168 (2008).

[35] E. K. Lee, L. Yin, Y. Lee, J. W. Lee, S. J. Lee, J. Lee, S. N. Cha, D. Whang, G. S. Hwang, K. Hippalgaonkar, A. Majumdar, C. Yu, B. L. Choi, J. M. Kim, and K. Kim, Nano Lett., 12, 2918 (2012).

[36] J. Lei, D. Zhang, W. Guan, Z. Ma, Z. Cheng, C. Wang, and Y. Wang, Appl. Phys. Lett., 113, 083901 (2018).

[37] M. –J. Lee, J. –H. Ahn, J. H. Sung, H. Heo, S. G. Jeon, W. Lee, J. Y.. Song, K. –H. Hong, B. Choi, S. –H. Lee, and M. –H. Jo, Nat Comm., 7, 12011 (2016)

[38] H. Sevincli, and G. Cuniberti, Phys. Review. B., 81, 113401 (2010).

[39] D. Olaya, M. H. –Morales, D. Gomez, O. A. C. –Uribe, Z. –Y. Juang, and Y. Hernandez, 2D Mater., 5, 011004 (2017).

[40] A. N. Gandi, and U. Schwingenschlogl, Chem. Mater., 26, 6628,

(2014).

[41] J. Zhang, H. J. Liu, L. Cheng, J. Wei, J. H. Liang, D. D. Fan, P. H. Jiang, L. Sun, and J. Shi, J. Mater. Chem. C., 4, 991, (2016).

[42] Y. Ma, Q. Hao, B. Poudel, Y. Lan, B. Yu, D. Wang, G. Chen, and Z. Ren, Nano Lett., 8, 2580, (2008).

[43] B. Poudel, Q. Hao, Y. Ma, Y. Lan, A. Minnich, B. Yu, X. Yan, D. Wang, A. Muto, D. Vashaee, X. Chen, J. Liu, M. S. Dresselhaus, G. Chen, Z. Ren, Science., 320, 634, (2008).

[44] K. Hasezaki, T. Hamachiyo, M. Ashida, T. Ueda, and Y. Noda, Mater. Trans., 51, 5, 863 (2010).

[45] J. Xiong, F. Jiang, H. Shi, J. Xu, C. Liu, W. Zhou, Q. Jiang, Z. Zhu, and Y. Hu, ACS Appl. Mater. Interfaces., 7, 14917 (2015).

[46] X. Wang, F. Meng, H. Tang, Z. Gao, S. Li, F. Jiang, and J. Xu, J. Mater. Sci., 52, 9806 (2017).

[47] T. C. Harman, P. J. Taylor, M. P. Walsh, and B. E. LaForge, Science., 297 2229 (2002).

[48] R. Venkatasubrammanian, E. Siivola, T. Colpitts, and B. O. Quinn, Nature., 413, 597 (2001).

[49] T. Zhang, S. Wu, J. Xu, R. Zheng, and G. Cheng, Nano Energy, 13, 433 (2015).

[50] K. Zhao, H. Duan, N. Raghavendra, P. Qiu, Y. Zeng, W. Zhang, J. Yang, X. Shi, and L. Chen, Adv. Mater., 29, 1701148 (2017).

[51] B. Xu, T. Feng, Z. Li, S. T. Pantelides, and Y. Wu, Nano Lett., 18, 4034 (2018).

[52] H. Yang, P. Wen, X. Zhou, Y. Li, B. Duan, P. Zhai, and Q. Zhang, Scr. Mater., 159, 68 (2019).

[53] M. Kashiwagi, S. Hirata, K. Harada, Y. Zheng, K. Miyazaki, M. Yahiro, and C. Adachi, Appl. Phys. Lett., 98, 023114 (2011).

[54] J. Tang, H. –T. Wang, D. H. Lee, M. Fardy, Z. Huo, T. P. Russell, and P. Yang, Nano Lett., 10, 4279 (2010).

[55] S. Hong, J. Park, S. G. Jeon, K. Kim, S. H. Park, H. S. Shin, B. Kim, S. Jeon, and J. Y. Song, J. Mater. Chem. C., 5, 8974 (2017).

[56] K. Kim, J. Park, S. Hong, S. H. Park, S. G. Jeon, C. Ahn, J. Y. Song and S. Jeon, Nanoscale., 10, 3046 (2018).

[57] J. Maire, and M. Nomura, Japanese Journal of Applied Physic., 53, 06JE09 (2014).

[58] D. S. Smith, A. Alzina, J. Bourret, B. N. –Ali, F. Pennec, N. T. –Doyen, K. Otsu, H. Matsubara, P. Elser, and U. T. Gonzenbach, J. Mater. Res., 28, 17 (2013).

[59] R. Anufriev, and M. Nomura, Science and Technology of Advanced Materials, 19, 1, 863 (2018).

[60] M. Maldovan, Phys. Rev. Lett., 110, 025902 (2013).

[61] T. Gorishnyy, M. Maldovan, C. Ullal, and E. Thomas, Phys. World., 2 (2005).

[62] M. –H. Lu, L. Feng, and Y. –F. Chen, Mater. Today., 12, 12, 34 (2009).

[63] J. –K Yu, S. Mitrovic, D. Tham, J. Varghhese, and R. Heath, Nat. Nanotechnol., 5, 718 (2010).

[64] G. –S. Kim, M. –R. Lee, S. –Y. Lee, J. –H. Hyung, N. –W. Park, E. S. Lee, and S. –K. Lee, Nanoscale Res. Lett., 8, 371 (2013).

[65] P. E. Hopkins, C. M. Reinke, M. F. Su, R. H. Olsson III, E. A. Shaner, Z. C. Leseman, J. R. Serrano, L. M. Phinney, and I. E. –Kady, Nano Lett., 11, 107 (2011).

[66] L. Yang, N. Yand, and B. Li, Sci. Rep., 3, 1143, 1 (2013).

[67] M. Maldovan, Nature., 503, 209 (2013).

[68] M. Nomura, and J. Maire, J. Electron. Mater., 44, 6, 1426 (2014).

[69] R. Anufriev, and M. Nomura, Phys. Rev. B, 91, 245417 (2015).

[70] S. Takahashi, M. Okano, M. Imada, and S. Noda, Appl. Phys. Lett., 89, 123106 (2006).

[71] S. Takahashi, K. Suzuki, M. Okano, M. Imada, T. Nakamori, Y. Ota, K. Ishizaki, and S. Noda, Nat. Mater., 8, 721 (2009).

[72] Y. –J. Hung, S. –L. Lee, and L. A. Coldren, Opt. Express., 18, 7, 6841 (2010).

[73] M. Deubel, M. Wegener, A. Kaso, and S. John, Appl. Phys. Lett., 85, 11, 1895 (2004).

[74] M. Deubel, G. V. Freymann, M. Wegener, S. Pereira, K. Busch, and C. M. Soukoulis, Nat. Mater., 3, 444 (2004).

[75] N. Tetreault, G. V. Freymann, M. Deubel, M. Hermatschweiler, F. P. –Willard, S. John, M. Wegener, and G. A. Ozin, Adv. Mater., 18, 457 (2006).

[76] M. S. Rill, C. Plet, M. Thiel, I. Staude, G. V. Freymann, S. Linder, M. Wegener, Nat. Mater., 7, 543 (2008).

[77] S. Rekstyte, E. Kaziulionyte, E. Balciunas, D. Kaskelyte, and M. Malinauskas, J. Laser. Micro. Nanoeng., 9, 1, 25 (2014).

[78] K. Terzaki, N. Vasilantonakis, A. Gaidukeviciute, C. Reinhardt, C. Fotakis, M. Vamvakaki, and M. Farsari, Opt. Mater. Express., 1, 4, 586 (2011).

[79] S. H. Wong, M. Thiel, P. Brodersen, D. Fenske, G. A. Ozin, M. Wegener, and G. V. Freymann, Chem. Mater., 19, 4213 (2007).

[80] F. G. –Santamaria, M. Xu, V. Lousse, S. Fan, P. V. Braun, and J. A. Lewis, Adv. Mater., 19, 1567 (2007).

[81] Y. Jun, P. Nagpal, and D. J. Norris, Adv. Mater., 20, 606 (2008).

[82] M. Campbell, D. N. Sharp, M. T. Harrison, R. G. Denning, and A. J. Turberfield, Nature., 404, 53 (2000).

[83] J. H. Moon, S. Yang, W. Dong, J. W. Perry, A. Adibi, and S. –M. Yang, Opt. Express., 14, 13, 6297 (2006).

[84] Y. C. Chen, J. B. Geddes III, J. T. Lee, P. V. Braun, and P. Wiltzius, Appl. Phys. Lett., 91, 241103 (2007).

[85] V. Ramanan, E. Nelson, A. Brzezinski, P. V. Braun, and P. Wiltzius, Appl. Phys. Lett., 92, 173304 (2008).

[86] J. –H. Jang, C. K. Ullal, M. Maldovan, T. Gorishnyy, S. Kooi, C. Koh, and E. L. Thomas, Adv. Funct. Mater., 17, 3027 (2007).

[87] L. Dong, L. Wang, M. Liu, M. Yu, Z. Wang, Z. Wang, Z. Zhang, D. Li, and Z. Zhang, IEEE international Conference on Manipulation, Manufacturing and Measurement on the Nanoscale, (2018).

[88] C. –H. Chang, L. Tian, W. R. Hesse, H. Gao, H. J. Choi, J. –G. Kim,

M. Siddiqui, and G. Barbastathis, Nano Lett., 11, 2533 (2011).

[89] T. Y. Jeon, H. C. Jeon, S. Y. Lee, T. S. Shim, J. –D. Kwon, S. –G. Park, and S. –M. Yang, Adv. Mater., 26, 1422 (2014).

[90] J. E. Elek, X. A. Zhang, B. Dai, Z. Xu, and C. –H. Chang, Nanoscale., 7, 10, 4406 (2015).

[91] J. –H. Min, X. A. Zhang, and C. –H. Chang, Opt. Express, 24, 2, A276 (2015).

Chapter.2 Fabrication of 3D periodic nanostructures

2.1 Proximity nanopatterning process (PnP)

The PnP process fabricates 3D periodic nanostructure via a phase shift mask (PSM) with 2D periodic pattern. It is a method similar to the traditional photolithography, which uses a laser as a light source that passes through the PSM to generate a unique light intensity distribution via diffraction and interference effects. The optics of this system has a very simple configuration. The fabrication of 3D periodic nanostructures by the PnP process was first reported in 2004 by S. Jeon, J. A. Rogers and others as a process based on phase shift lithography [1]. The process of the 3D periodic nanostructure uses a region of light intensity distribution from the PSM and a photosensitive resin with a low absorption coefficient. The major characteristic is that 3D nanostructure can be easily formed by single laser irradiation. Moreover, there are reports on the fabrication of 3D structures with hierarchical structure size by changing the periodic structure easily via PSMs with different designs and increasing the absorption coefficient of the photosensitive material. [2–5]

In this study, a laser system using a UV laser with a wavelength of 355 nm was constructed to establish a PnP process aiming at 3D PhC and 3D PnC applications. Also, the process conditions were optimized to form a 3D periodic nanostructure with negative photosensitive resins. The overall schematic of the process is shown in Fig. 2.1.

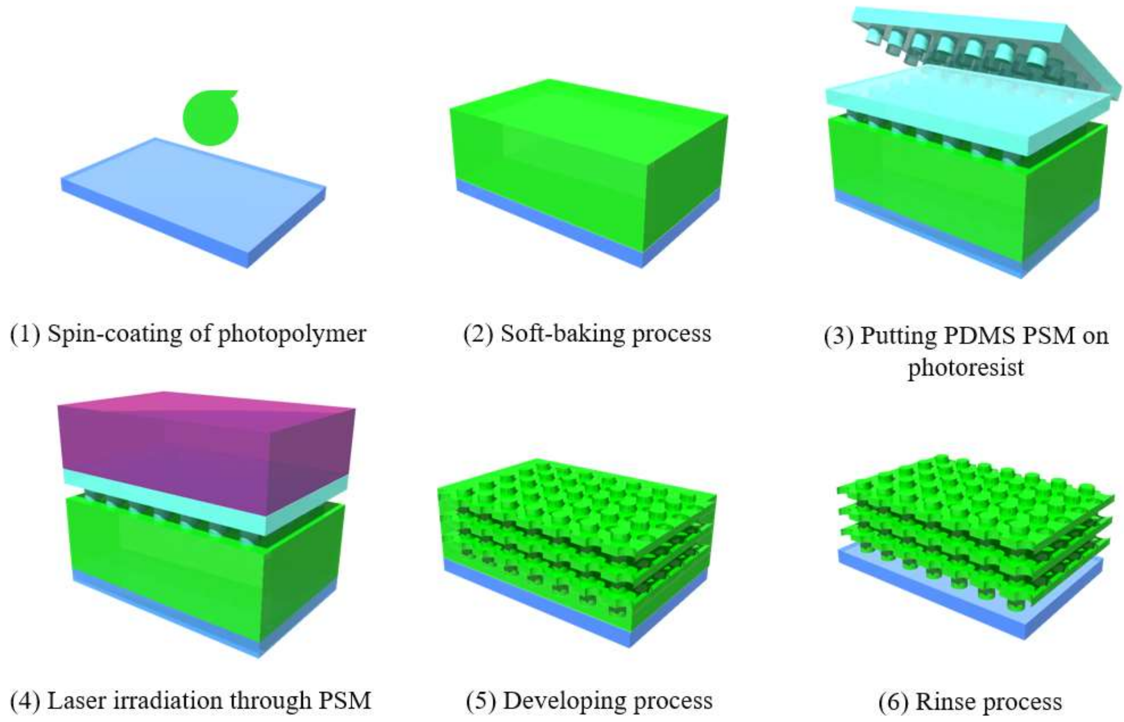

Figure 2.1 Schematic diagram of PnP process.

2.1.1 Mechanism of PnP process

The formation of a 3D light intensity distribution via PSM used in the PnP process is known as the Talbot effect [6]. It is a phenomenon that forms an intensity pattern (self-image) with the same period as the diffraction grating when coherent light (laser light, etc.) passes through the diffraction grating (PSM, etc.) and propagates for a specific distance (Talbot distance) [7–11]. The specific distance called Talbot distance Z_T is given by

$$Z_{\mathrm{T}} = \frac{\lambda_{\mathrm{mid}}}{1-\sqrt{1-\left(\lambda_{\mathrm{mid}}/p\right)^2}} \cong \frac{2p^2}{\lambda_{\mathrm{mid}}} \quad \left(\text{when } \lambda_{\mathrm{mid}}/p \text{ is small}\right) \tag{2.1}$$

and the wavelength λ_{mid} of coherent light in the medium is expressed by

$$\lambda_{\mathrm{mid}} = \lambda_0/n_{\mathrm{m}} \tag{2.2}$$

[12] The parameters of this formula are associated with the wavelength of coherent light in free space: λ_0, the refractive index of the medium: n_m, and the period of the diffraction grating: p. When the same laser wavelength and medium are used, the periodic structure size in the direction of laser exposure can be altered by changing the period of the diffraction grating. In the in-plane direction, the periodic structure size will be the same as the period of the diffraction grating. The formation of the 3D light intensity distribution in the PnP process is largely contributed by the 0th-order diffracted light, the +1st-order diffracted, and the −1st-order diffracted light [13–15]. As shown in Fig. 2.2, a unique light intensity distribution is obtained due to the interference effect at the part where these three diffracted lights overlap [16,17].

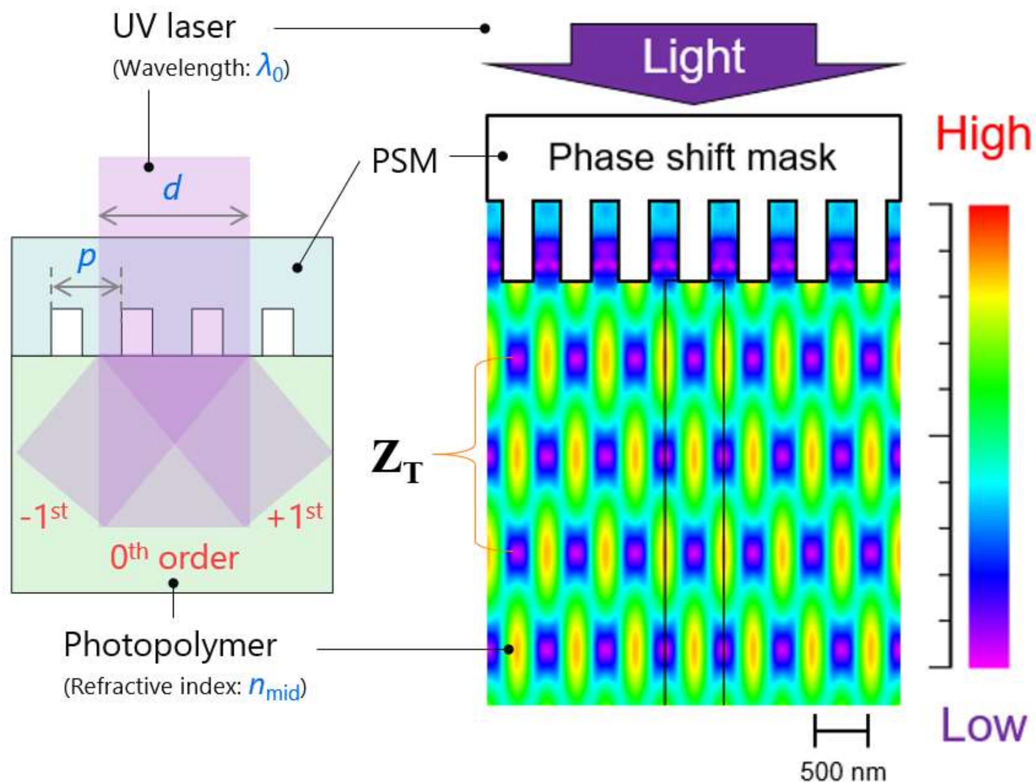

Figure 2.2 Schematic diagram of PSM (left) [15] and cross-section intensity distribution diagram simulated by Roft simulation software (right) [16].

2.1.2 Photoresist

A light-sensitive material called a photoresist is widely used in several processes such as photolithography photoengraving, and especially in the field of microelectronics [18]. It is the most basic and important element, which can is classified positive and negative types; the mechanism of those two are different. For positive resists, the portions of the photoresist exposed with a specific wavelength of light will photo-decompose and become soluble to the photoresist developer, and the unexposed part will remain unsolvable to the developer which will serve as the skeleton of structure. The negative type is the opposite of the positive type. The areas exposed to the light source cause the photoresist to crosslink or polymerize, making it insoluble to the developer. The unexposed part will be removed after developing step [19]. In this study, the negative photoresist was used due to its excellent properties:

I. High aspect ratio imaging with near vertical side walls,
II. Near UV (350–400 nm) processing,
III. Film thicknesses from 1 to > 200 μm by single spin coat processes,
IV. Superb chemical and temperature resistance.

Two negative type photoresists that meet these characteristics were used to fabricate the nanostructures. SU8 (MicroChem) is a commonly used epoxy-based negative photoresist. Its maximum absorption is under ultraviolet light at 365 nm wavelength and it also has high thermal stability.

It is mainly used in the fabrication of microfluidics, nanoimprint lithography, microelectromechanical systems (MEMS) and bio-MEMS [20–23]. To fabricate the 3D inverse nanostructure, the solution-derived semiconductor material is deposited on the SU8 nanostructure; voids inside the structure are filled by capillary action. Then with high-temperature annealing treatment, the solution-derived material solidifies and SU8 structure sublimates. Another photoresist is KMPR (MicroChem), which is a high contrast photosensitive, epoxy-based photoresist that can be developed in a conventional aqueous alkaline developer (TMAH) and readily stripped from the wafer [24]. The most attractive characteristic of KMPR is that after fully curing, it can be removed by solution process which provides a method to make a 3D inverse structure without high-temperature annealing. Therefore, heat-sensitive thermoelectric materials can be expected to be used to form this kind of inverse nanostructure.

2.1.3 Polydimethylsiloxane (PDMS) phase shift mask (PSM)

PDMS belongs to a group of polymeric organosilicon compounds that are commonly referred to as silicones [25]. It is the most widely used silicon-based organic polymer and is particularly known for its unusual rheological properties. As described in Sec. 2.1.1, the structural size of the 3D periodic nanostructure formed in the PnP process largely depends on the design of the nanopattern possessed by the PSM. The size of the periodic structure in the in-plane direction should be theoretically the same size as the PSM. In relation to the film thickness direction, it will be the Talbot distance which

derived from Eq. 2.1. Therefore, the Talbot distance can be controlled through the period of the nanopattern possessed by PSM.

The fill factor (*FF*) is defined as the ratio of the area of the grating structure (*S*) to the area of the unit cell (p^2), to discuss the intensity contrast was generated between different fill factors:

$$FF = S/p^2 \tag{2.3}$$

where p is the period as shown in Fig. 2.3. The *FF* will affect the diffraction

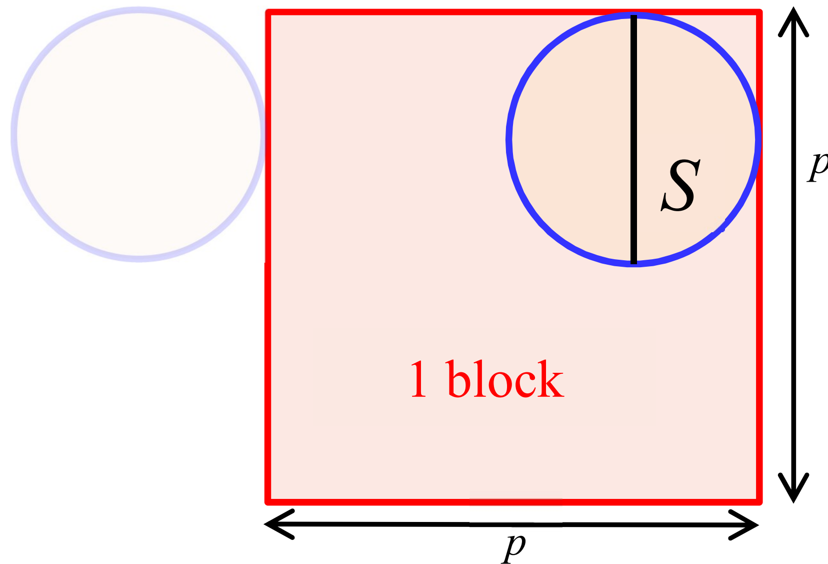

Figure 2.3 PDMS pattern design principles.

resolution by affecting the intensity contrast during the exposure process as seen in Fig. 2.4, and when the area of the grating structure is half of that of the unit cell (*FF* reaches to 0.5), the maximum intensity contrast can be achieved resulting in high-resolution diffraction patterns that guarantees the quality of the 3D nanostructure [26]. As a result, the diameter of the circle was set to 480 nm and periodicity was set to 600 nm so that *FF* will be near 0.5. The PSM (2.1 cm × 2.1 cm) used under these parameters are by far the most repeatable parameter of the formed nanostructures, which was

produced with collaboration works at KAIST FDML laboratory. Due to limitations of the experimental equipment, this study did not discuss other sizes of PSMs.

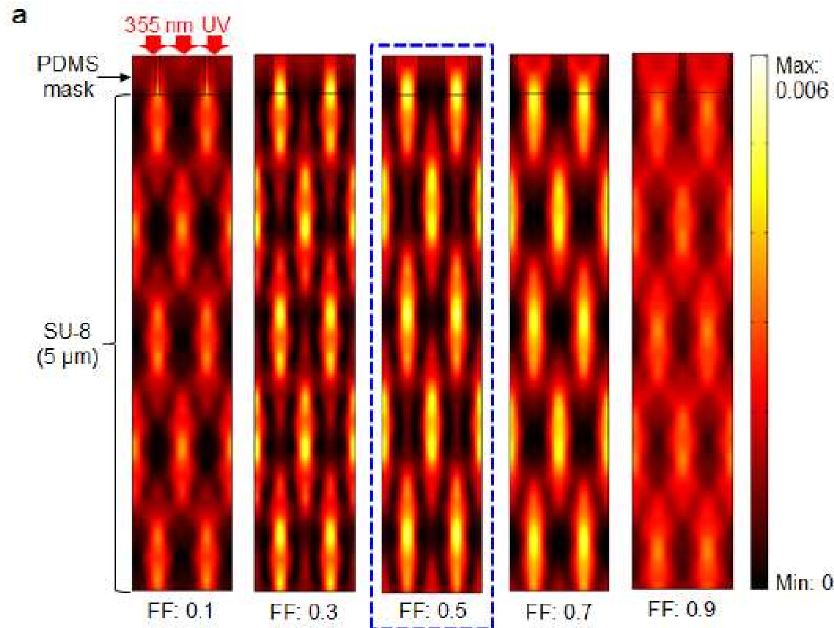

Figure 2.4 Calculated intensity distributions of interference patterns with different areal fill factors [26].

2.1.4 Construction of laser irradiation (exposure) system

The light source is another important element of PnP process. During the

Table 2.1 Basic specifications of UV laser light source.

Dimensions	186 mm x 60 mm x 36 mm
Wavelength	355 nm
Average Power	4 mW
Pulse Repetition Rate	Up to 4 kHz
Pulse width (FWHM)	<0.4 ns
Output energy	> 1 μJ

optimization experiment in this article, 4 versions of laser system were used. Nd:YAG 355 nm UV laser (STV-01E-100, TeemPhotonics, Table 2.1) is introduced as the laser source in versions 1 to 3. The PnP process requires vertical laser irradiation from above the sample with the PSM. Therefore, the laser system is built horizontally on an anti-vibration table. The purpose is to keep the laser as horizontal and uniform as possible when the beam expands. Mirror reflection is used to expose the sample surface, and the light beam is reflected at 90° and incidents vertically onto the sample. The first

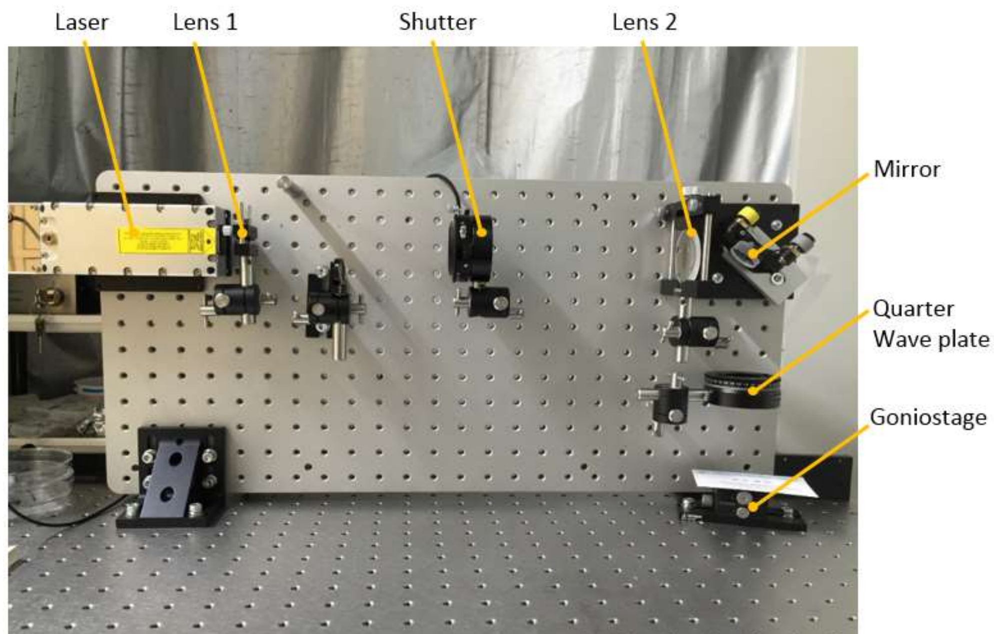

Figure 2.5 Laser system version 1.

laser system is shown in Fig. 2.5 which has an intensity of 1.2 mW/cm^2.

In order to have a large exposure spot which can have more uniform energy distribution, lens 2 was removed, and the distance between the lens 1 and the mirror was also increased in version 2. Also, the mirror was changed to a larger one, which caused a decrease in exposure intensity to 0.18 mW/cm^2 (Fig. 2.6).

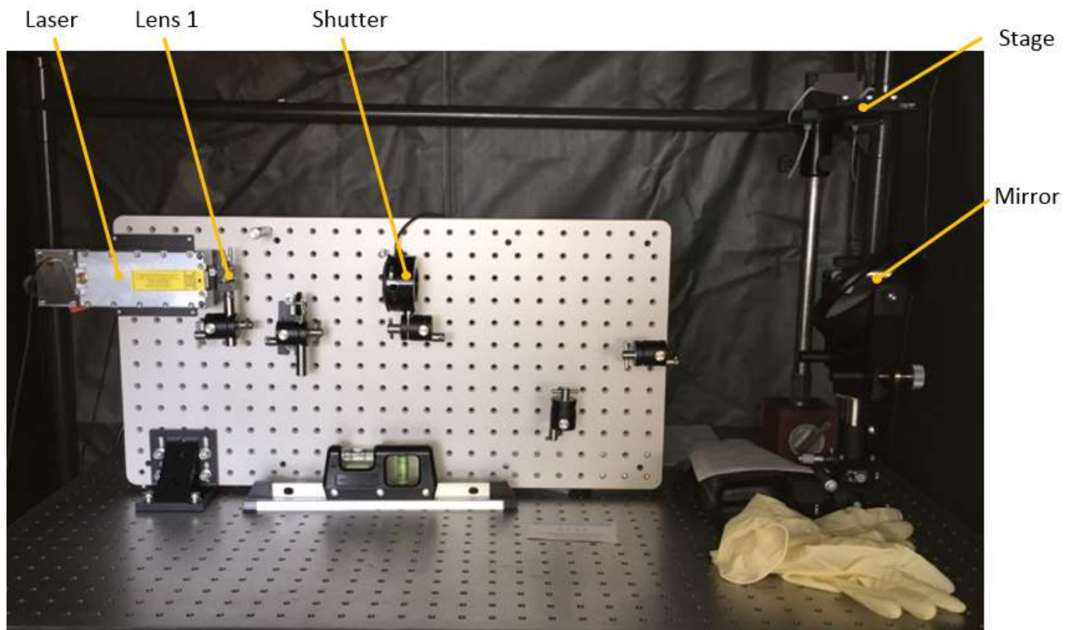

Figure 2.6 Laser system version 2.

However, the energy distribution of the exposure spot is extremely uneven without lens 2, resulting in the failure to form nanostructures. After adding lens 2 to make the beam pass through the beam expander formed by the two lenses, although the exposure spot became smaller, but the energy

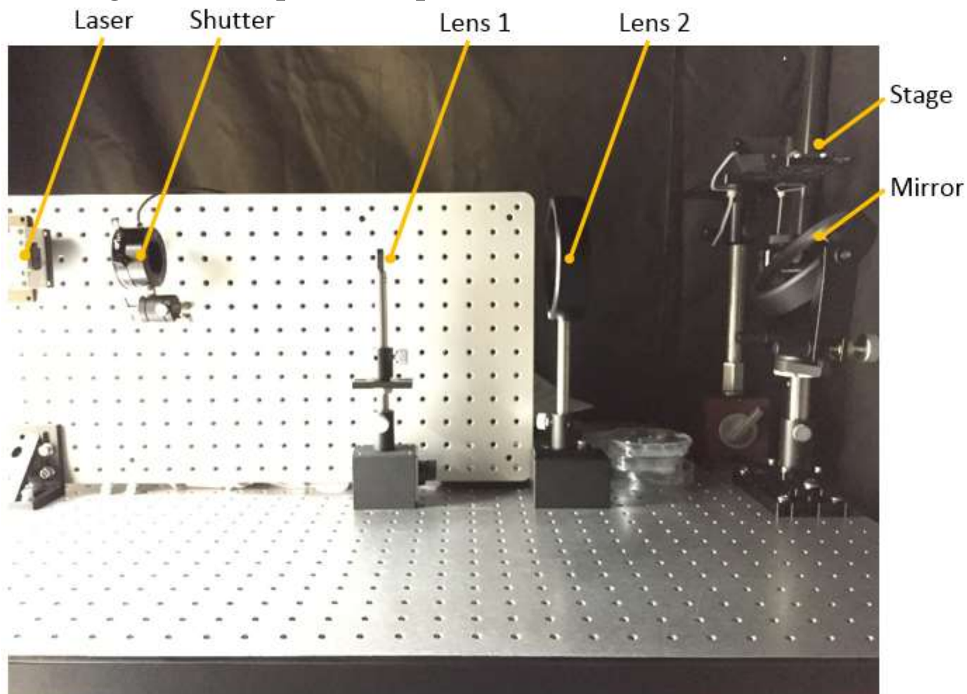

Figure 2.7 Laser system version 3.

distribution became uniform. Thereby laser system version 3 was assembled as shown in Fig. 2.7, which also improved exposure intensity from 0.18 to 0.3 mW/cm^2.

Unfortunately, due to the distance limitation of the anti-vibration table, the exposure spot still cannot reach the required beam diameter of $\phi = 4\ cm$. In the final version, a laser with the same wavelength (355-1-60, Matrix, Table 2.2) which can control the output power was used. In order to have a

Table 2.2 Basic specifications of UV laser light source.

Dimensions	100 mm x 131 mm x 335 mm
Wavelength	355 nm
Average Power	1 W at 60 kHz
Pulse Repetition Rate	Up to 100 kHz
Pulse width (FWHM)	< 25 ns
Output energy	> 16 μJ

more uniform exposure spot, the anti-vibration table was replaced, the distance between the lenses was increased, and a pinhole was also set at the focal point. During the exposure, the mirror was changed in the manner that the laser beam goes vertically into the air to allow the laser to evenly pass through the PSM and photoresist without any reflection, so as to ensure the uniformity of the periodic nanostructure (Fig. 2.8).

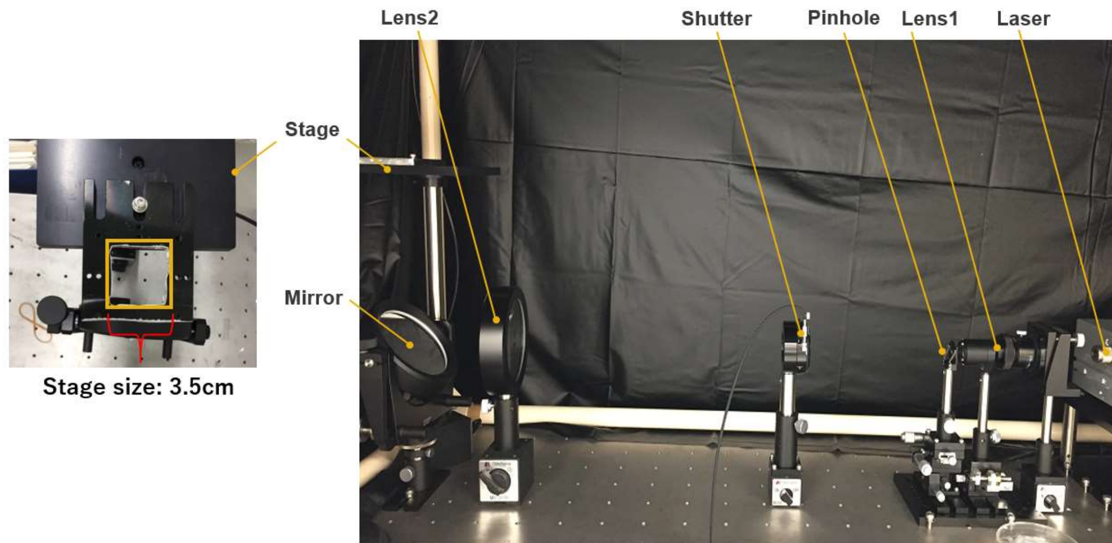

Figure 2.8. Laser system version 4.

In the case of this setup, the clearly and uniformly exposure spot is obtained as shown in Fig. 2.9.

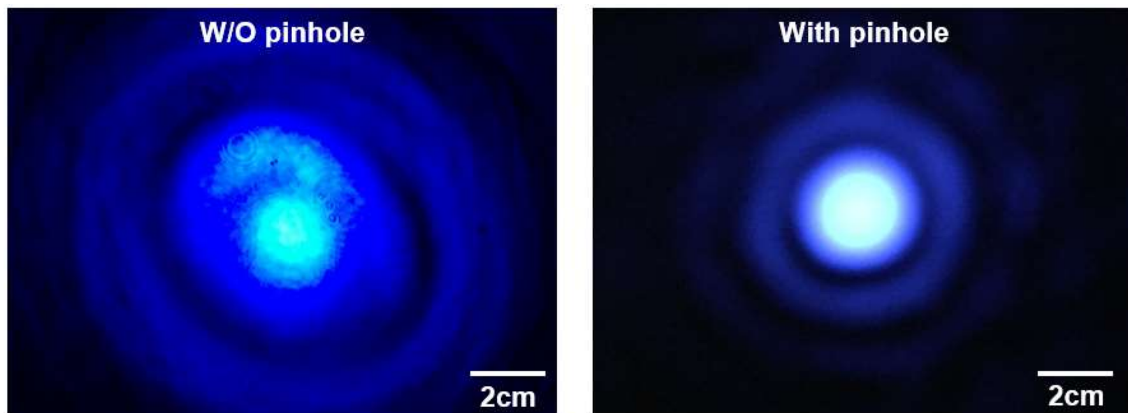

Figure 2.9. Exposure spot (Left: without pinhole, Right: with pinhole).

2.1.5 The procedures of PnP process

In this section, all steps of the PnP process and their purpose will be mainly introduced as follow:

(a) *Cleaning*: To remove the organic or inorganic contaminations on the glass substrate surface and keep good quality of the structure.

(b) *Spin Coating*: Make the film uniform upon substrate deposition and control the thickness by changing the spin speed/time.

(c) *Soft-bake I (Soft-bake)*: The purpose of soft-bake is to mitigate the stress which was generated by the spin coating process and enhance the photoresist adhesion so that the photoresist will not be detached from the substrate.

(d) *Soft-bake II (Bake)*: Enhance the photoresist light absorption and resistance to corrosion; also improve the photoresist adhesion so that the nanostructure layer can well-connect with the adhesion layer.

(e) *Laser exposure*: Activate the photoactive compound in the photoresist, enhance crosslinking and polymerization. This process can achieve higher resolution by decreasing the wavelength of the light source. (Normally lower than 400 nm)

(f) *Post-exposure bake*: Help smooth rough features on the sidewalls caused by standing wave phenomenon of thin film interference in a single exposure process, and promote the polymerization reaction induced by the photoactive compound. At the same time, it can also improve the quality of the structure.

(g) *Developing and rinse*: Dissolve the unexposed part, and remove. Make the pattern appear.

2.2 3D periodic nanostructures fabricated by PnP process with KMPR

2.2.1 Fabrication procedures of KMPR nanostructure

The optimized PnP process using KMPR was carried out according to the following procedure:

(a) Substrate cleaning

The micron cover glass (70 × 80 mm) with 0.13–0.17 mm thickness (MATSUNAMI Glass Ind., LTD.) is used as the substrate due to its excellent properties (such as advanced cleaning quality, good transparency and high flatness and dimensional accuracy). Then, it is cleaned with acetone, ethanol and ultrapure water ultrasonic cleaning for 5 min, respectively. Next, UV-O_3 (UV-1, Samco) treatment is done at 115 °C for 10 min to remove the organic residues.

(b) Fabrication of adhesion layer

Due to the porous nature of the fabricated 3D nanostructure templates, it will make the adhesion between structure and substrate surface weaker. Thus there is a high possibility that the structure will peel off from the substrate during the developing process. Therefore, an adhesion layer is needed which is formed with: 2000 rpm, 30 sec for spin-coating, soft-bake at 95°C for 3

min, then full exposure with a UV lamp (366 nm, 3 min) and hard-bake at 180°C for 3 min. The adhesion layer of KMPR is formed by using KMPR photoresist after being diluted with cyclopentanone (FUJIFILM Wako Pure Chemical Corporation) which can modify the solution viscosity and film thickness. The thickness of this layer should be lower than 4 μm [24].

(c) Spin-coat and soft-bake

A KMPR solution with 12.1 mol/L is spin-coated on top of the adhesion layer at 3500 rpm for 40 sec, then two-step soft-bake are performed at 70°C for 15 min and at 100°C for 15min on a hotplate.

(d) Laser exposure through PSM

Setting the PSM mask on top of the photoresist by using a tweezer lightly pressed on the glass side of the substrate to remove air bubbles and make conformal contact. Then expose the KMPR to a total exposure dose of 25 mJ/cm^2.

(e) Post-exposure bake (PEB)

The PEB process (65°C/7 min) promotes the polymerization reaction induced by the photoactive compound generated by the laser irradiation and the epoxy groups will cross-link to form the cured structure.

(f) Developing, rinse and dry

After PEB, immerse the sample in the SU8 developer (MicroChem) for

15 min, then in a buffer solution (1:1 mixture with developer and ethanol) for 10 sec to change the high surface tension of the sample to a lower one and avoid internal agglomeration of the porous 3D structure. In the final step, immerse the structure in ethanol for another 15 min and air-dried until the ethanol is completely removed.

2.2.2 Surface uniformity of photoresist

The original KMPR photoresist possesses high viscosity from 6000 – 15000 mPa·s. In order to make an appropriate concentration of KMPR that can be used for nanostructure, the mainly used solvent of KMPR, cyclepentanone, is used to dilute the KMPR photoresist. Three different concentrations of solution were made: undiluted KMPR, KMPR: Cyclopentanone = 5:1 and 2:1 (Mass ratio) as shown in Fig. 2.10–2.12,

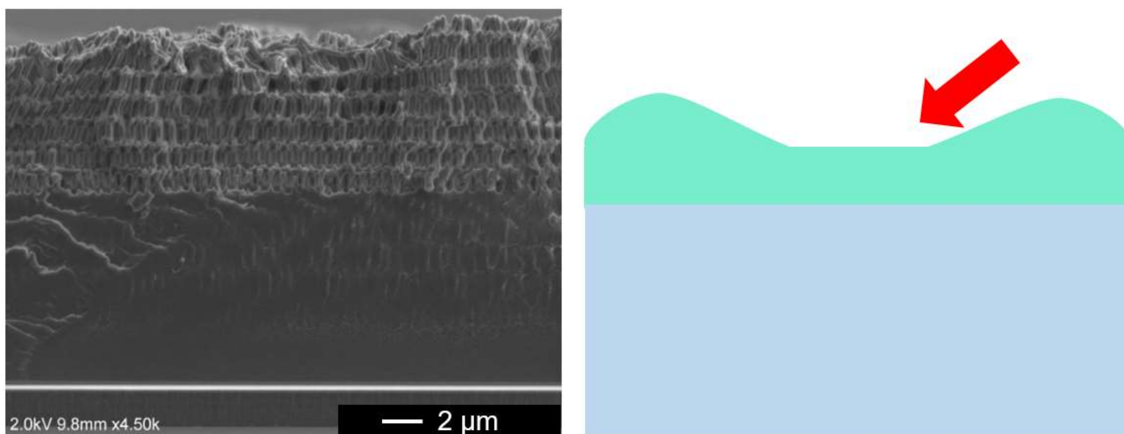

Figure 2.10. SEM image and schematic for undiluted KMPR.

respectively. Nanostructure of the undiluted KMPR had a uniform center, however, the sides near the center were bulging, which will have a negative effect when making conformal contact with PSM (Fig. 2.10). When KMPR is diluted by a mass ratio 5:1 with cyclopentanone, the film with 13 μm

thickness was obtained and it became more uniform than the undiluted one,

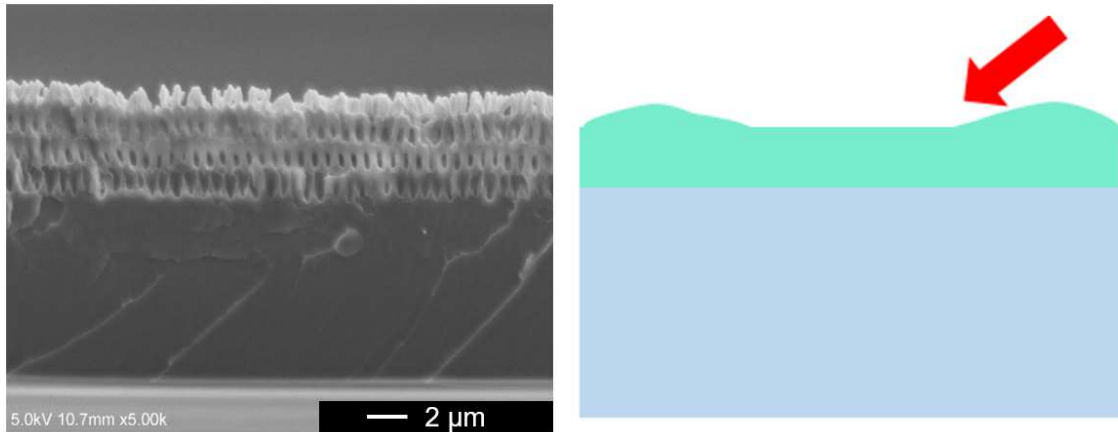

Figure 2.11. SEM image and schematic for KMPR : Cyclopentanone = 5 : 1 (Mass ratio).

but bulging near the edges still exist due to the coffee ring effect (Fig. 2.11). Nanostructure of the dilute KMPR (2:1) resulted in the most uniform surface

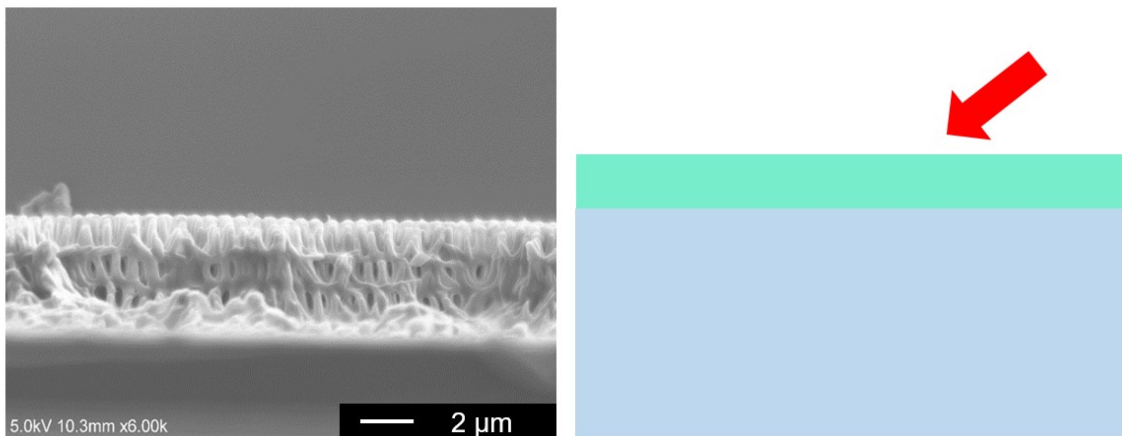

Figure 2.12. SEM image and schematic for KMPR : Cyclopentanone = 2 : 1 (Mass ratio).

with the 4.8 μm film thickness as shown in Fig. 2.12. However, this film thickness is much different from the expected film thickness of 10 μm. Therefore, the most appropriate ratio of KMPR to cyclopentanone was decided at 5 to 1, and the spin-coat speed is controlled to obtain the film thickness of 10 μm. At the same time larger substrates (70 mm×80 mm)

were used to enlarge the uniform part. After spin-coating all of the photoresist layers, the bulging part is removed by cutting with a diamond

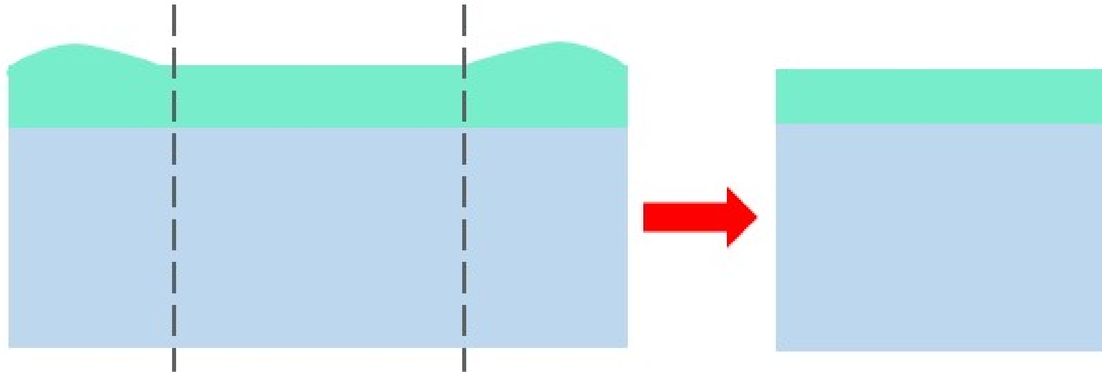

Figure 2.13. Method of obtaining a flat template.

pen, which leaves the most flat part to fabricate 3D nanostructure (Fig. 2.13).

2.2.3 Effects of different soft-bake conditions

Since KMPR and SU8 photoresists are both based on epoxy resins, the same fabrication conditions with SU8 which was already clearly fabricated in the reference is used at the beginning [27,28]. Figure. 2.14 shows that the KMPR nanostructure cannot form with this condition owing to the curing agent wherein some ingredients are different. According to the KMPR Data

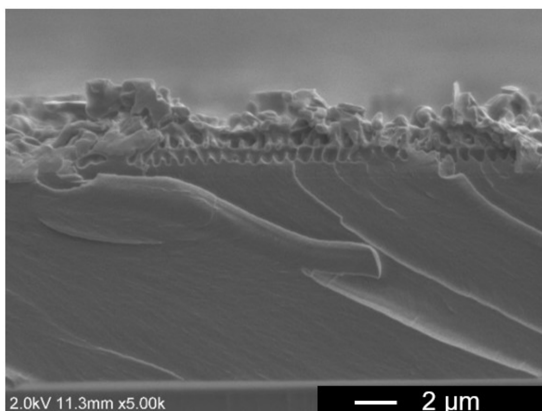

Figure 2.14. Cross-sectional SEM image of same conditions with SU8.

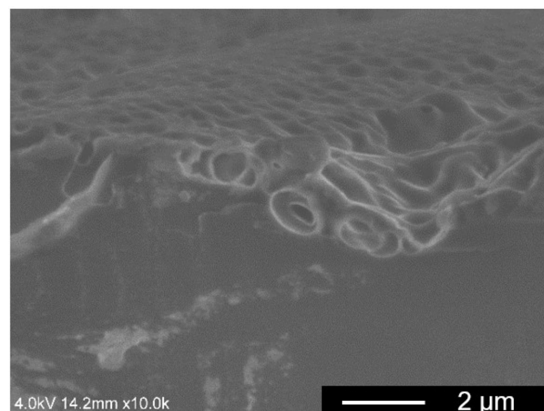

Figure 2.15. Cross-sectional SEM image of soft-bake 100°C for 5 min.

sheet, soft-bake at 100°C for 5 min is a suitable condition to fabricate a 10 μm film, unfortunately this condition did not work on our nanostructure as shown in Fig. 2.15. Then the soft bake temperature was changed to 105°C, and the nanostructure is partly formed but not very clearly; most parts are

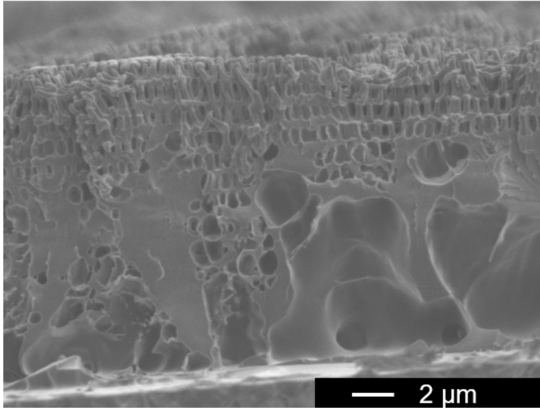

Figure 2.16. Cross-sectional SEM image of soft-bake 105°C for 5 min.

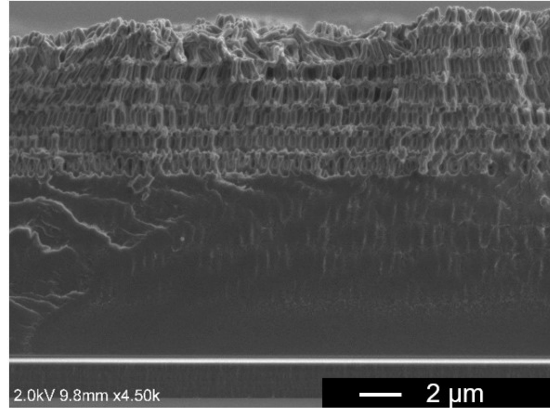

Figure 2.17. Cross-sectional SEM image of soft-bake 115°C for 5 min.

dissolved and collapsed (Fig. 2.16). After this, 115°C soft-bake temperature in an aluminum box is used to get more uniformly heat to sample. The clear and periodic nanostructure is shown in Fig. 2.17, however half of the film near the substrate still has no clear nanostructure. When the temperature reached 150°C using the oven instead of the aluminum box, with the diluted solution (KMPR : Cyclopentanone = 5 : 1), a uniform nanostructure from surface to adhesion layer was fabricated but the size of nano pillars is still not uniform (Fig. 2.18). After that, two steps of the soft bake method are introduced to remove the stress. The first step is set at 60°C for 5 min to slow down the heating rate. Then, the second step is performed at 150°C for another 5 min, and a more periodic nanostructure was obtained as presented in Fig. 2.19.

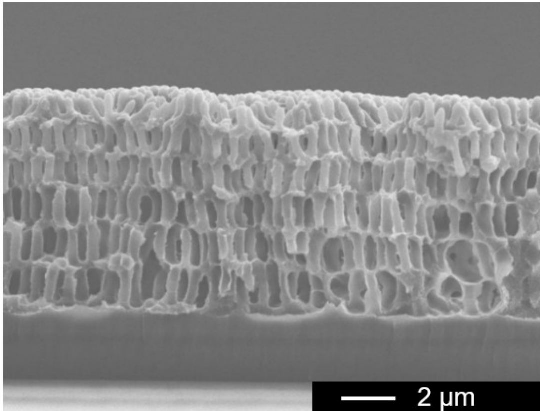

Figure 2.18. Cross-sectional SEM image of soft-bake 150°C for 5 min.

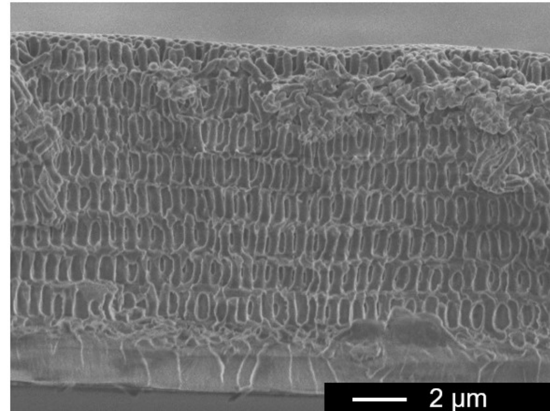

Figure 2.19. Cross-sectional SEM image of two steps soft-bake.

2.2.4 Effects of different UV exposure conditions

UV laser exposure dose and time are also crucial for the PnP process. The difference in the size of the structure is caused by the difference in the total exposure dose as well as different kinds of photoresist. In this part, the exposure dose for KMPR was determined by changing the exposure time and irradiate intensity. The laser system as described in Sec. 2.1.4 was used as a UV light source.

Identical with the previous section, laser system version 1 was used with the same conditions used for SU8 as shown in Fig. 2.20 (UV exposure intensity: 1.2 mW/cm^2, exposure time: 20 sec) [28]. A 4.5-μm-thick nanostructure was formed from the surface and some parts of the structure collapsed. Then, the exposure time changed to 35 sec and got the results shown in Fig. 2.14. Nevertheless, the structure was not successfully fabricated at all.

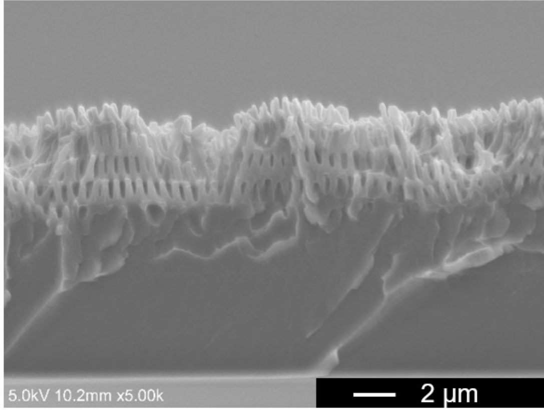

Figure 2.20. Cross-sectional SEM image of exposed for 20 sec (1.2 mW/cm^2).

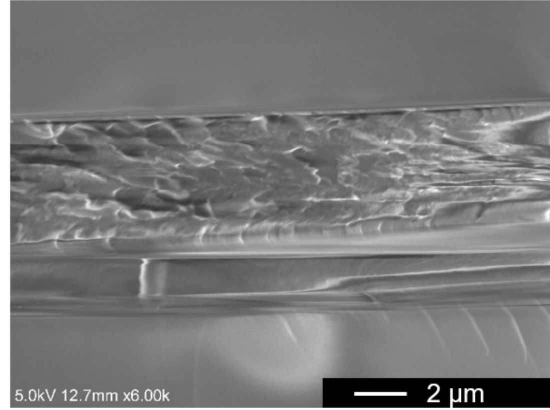

Figure 2.21. Cross-sectional SEM image of exposed for 150 sec (0.18 mW/cm^2).

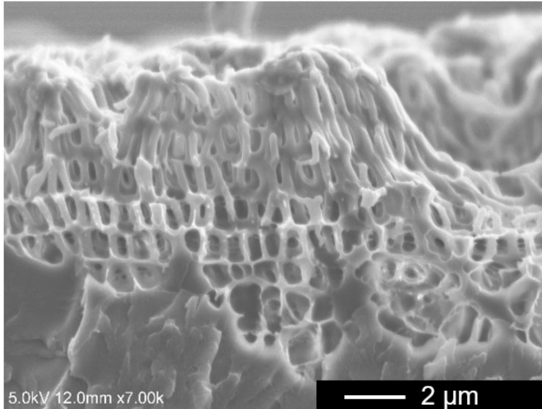

Figure 2.22. Cross-sectional SEM image of exposed for 190 sec (0.18 mW/cm^2).

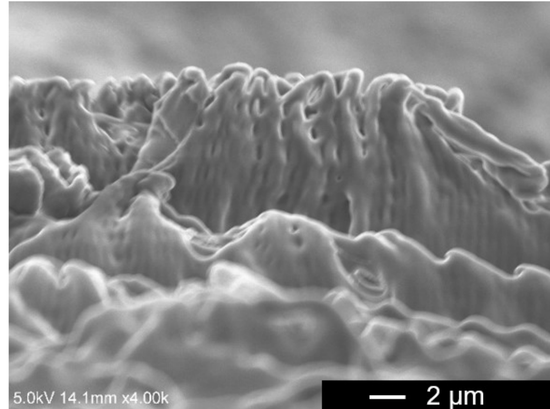

Figure 2.23. Cross-sectional SEM image of exposed for 250 sec (0.18 mW/cm^2).

Next, the laser system was revised to version 2 (Fig. 2.6) so that UV exposure intensity decreased to 0.18 mW/cm^2. In this case, the fabrication of nanostructure needed more time for exposure and UV curing reaction could proceed slowly. Therefore, the structure likely formed clearly all over the thin film. In order to confirm the necessary UV exposure time for the 3D nanostructure, three different conditions were performed: 150 sec, 190 sec and 250 sec. From the cross-section SEM observation (Fig. 2.21–2.23), 150 sec and 190 sec could not form the nanostructure. However, when exposure

time was increased to 250 sec, the nanostructure partly appeared. Those results were all under the condition at 115°C for 5 min in the soft bake step. In order to the influence of soft-bake, the samples was baked in an aluminum box to make samples uniformly be heated (Fig. 2.24). As a comparison, the UV exposure time 270 sec was also tested as follows (Fig. 2.25).

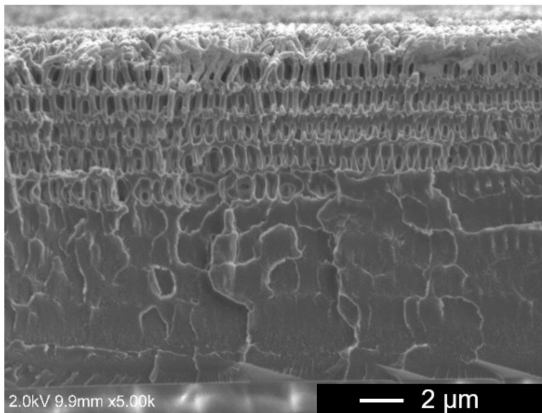

Figure 2.24. Cross-sectional SEM image of exposed for 250 sec (0.18 mW/cm^2).

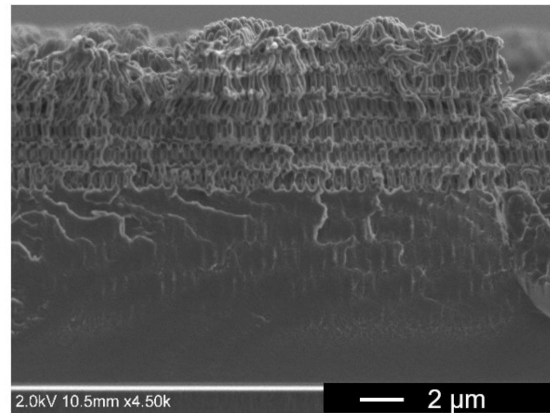

Figure 2.25. Cross-sectional SEM image of exposed for 270 sec (0.18 mW/cm^2).

Nanostructure was fabricated clearly and periodically, but the nanostructures cannot be obtained over the whole thin film area. Also, the collapsed parts still existed. As for film thickness, when the film was too thick in the soft-bake step, the heat conduction was reduced, and this affected the UV diffraction during the exposure step. To solve those problems, diluted KMPR was used (KMPR: Cyclopentanone = 5:1). Also, the exposure time was decreased by changing the expansion lens from concave to convex and adjusting the distance between the two lenses while keeping the main exposure dose value identical with that in Fig. 2.21. These steps were done to decrease the whole process time and speed up the UV curing time (Fig. 2.7). Moreover, the soft-bake temperature at 150 °C was performed in an

oven instead of the aluminum box. The SEM image is shown as follows. Figure. 2.26 showed that the nanostructure was formed from surface to adhesion layer. However, pillars were still not uniform, and some parts were also collapsed. Then, the two steps soft baking mentioned in the above section was performed and the result in Fig. 2.27 was obtained. Basically, in this case the 3D nanostructure was fabricated clearly, periodically and perfectly, except the pillars were dissolved in some areas.

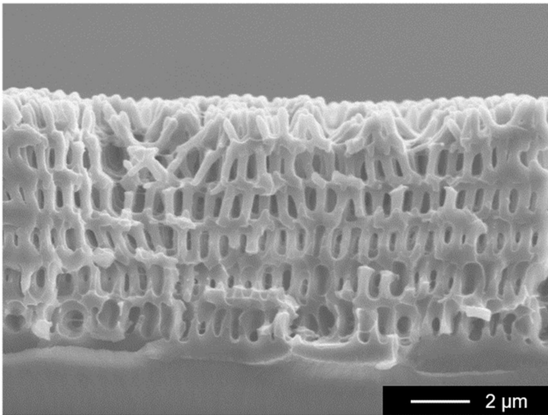

Figure 2.26. Cross-sectional SEM image of exposed for 90 sec (0.3 mW/cm^2).

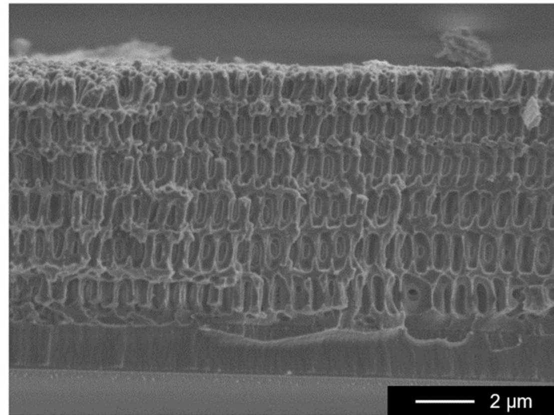

Figure 2.27. Cross-sectional SEM image of exposed for 90 sec with two steps soft-bake (0.3 mW/cm^2).

A summary of the UV irradiation intensity, exposure time and UV exposure dose are shown in Table 2.3. The UV exposure dose was calculated by UV exposure dose = UV intensity × Time. As seen in the summary below, when the irradiation time is 90 s and the UV exposure dose is 27 mJ/cm^2, the clearly 3D nanostructures can be fabricated with high periodicity.

Table 2.3 Summary of UV intensity, exposure time and UV exposure doses.

UV intensity (mW/cm^2)	Time (s)	UV exposure dose (mJ/cm^2)	Figure number
1.2	20	24	2.20
	35	42	2.14
0.18	150	27	2.21
	190	34.2	2.22
	250	45	2.23
	250	45	2.24
	270	48.6	2.25
0.3	90	27	2.26
	90	27	2.27

2.2.5 Reproducibility of KMPR 3D nanostructures

After establishing laser version 4 (Fig. 2.8) to obtain a more uniform and bigger laser exposure spot, the best conditions acquired from the above sections were used to confirm the reproducibility. Figure. 2.28 shows that

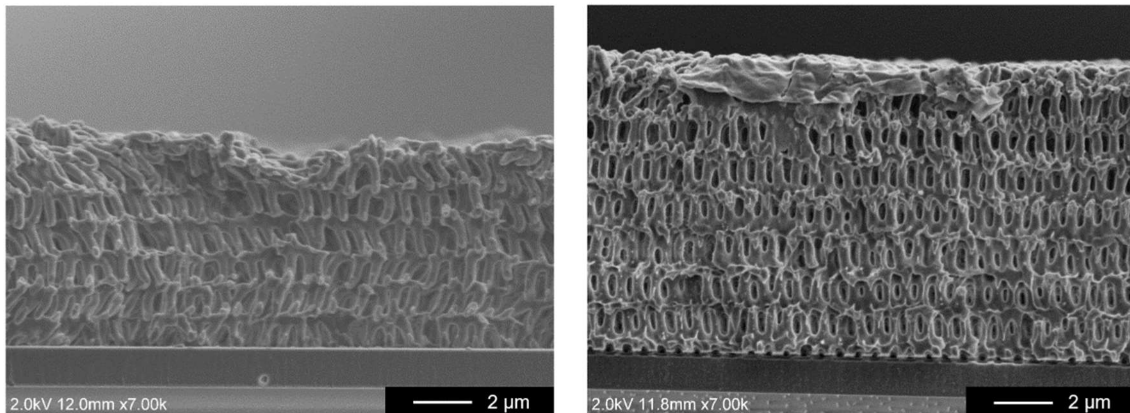

Figure 2.28. Cross-sectional SEM image of collapsed nanostructure (left) and surface skinning effect (right).

nanostructure was formed but the cracks and collapsed parts are observed more than the previous result which means the optimization is needed. Then the following adjustments were made with reference to the previous

conditions.

① Soft-bake I is performed at 70°C for 15 min on a hotplate. Increase temperature and time to remove most of the solvent as much as possible. (Also moisture in the air.)

② Soft-bake II is performed at 100°C for 15 min on a hotplate. Decrease the temperature to reduce the skinning effect of solvent depletion on the surface and prevent the formation of dense layer. Increase baking time to get rid of the remaining solvent.

③ Total exposure dose was set at 25 mJ/cm^2.

With these optimized conditions, the 3D nanostructure was fabricated as shown in Fig. 2.29 and reproducibility was affirmed by repeating the PnP process 10 times.

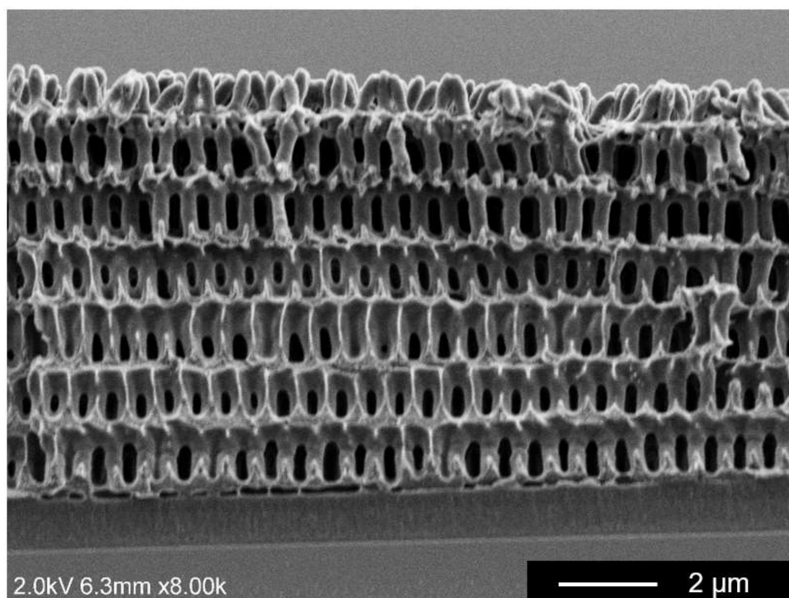

Figure 2.29. Cross-sectional SEM image of clearly 3D nanostructure with high periodicity.

2.3 3D periodic nanostructures fabricated by PnP process with SU8

2.3.1 Fabrication procedures of SU8 nanostructure

The PnP process using SU8 was carried out according to the following procedure:

(a) Substrate cleaning

Same glass substructure was used refer to Sec. 2.2.1 (a).

(b) Fabrication of adhesion layer

Adhesion layer of SU8 is spin-coat at 2000 rpm for 30 sec, soft-bake at 65°C for 1 min and at 95°C for 2 min, then fully cured with UV lamp (366 nm, 2 min) and hard-bake at 180°C for 2 min. Normally, the thickness of adhesion layer is 1–2 μm.

(c) Spin-coating and soft-bake

After the adhesion layer was formed on the cover glass, spin-coat (2000 rpm, 30 sec) SU8 on top of the adhesion layer, and soft-bake it at 65°C for 40 min and 95°C, 40 min. Two step soft-bake is generally a process to reduce stress formation during the baking.

(d) Laser exposure through PSM

Same operation as in the Sec. 2.2.1 (d) is done. Next, the SU8 film is irradiated by UV laser with an exposure dose of 10 mJ/cm^2.

(e) Post-exposure bake (PEB)

Refer to Sec. 2.2.1 (e)

(f) Developing, rinse and dry.

The SU8 developer is used for 30 min, same buffer solution used for KMPR which is performed for 10 sec. Finally, rinse the sample by using ethanol for another 30 min and air-dried until no more ethanol remains.

2.3.2 Effects of different soft-bake conditions

To investigate the soft-bake influence on SU8 nanostructure, the laser system shown in Fig. 2.7 was used. From the references, soft-bake conditions were normally set at 95°C for 5 or 10 min, and intermittently two step soft-baking was also utilized (at 65°C for 5 min and at 95°C for 10 min) [24,27,28]. Owing to the experience obtained from the KMPR production process aforementioned, two step soft-baking is more beneficial for the formation of the 3D nanostructure. Therefore, the following four conditions were chosen for the comparison.

(a) At 65°C for 10 min and at 95°C for 10 min

(b) At 65°C for 15 min and at 95°C for 15 min

(c) At 65°C for 30 min and at 95°C for 30 min

(d) At 65°C for 40 min and at 95°C for 40 min

As for the UV exposure, 15 mJ/cm^2 total exposure dose was applied and

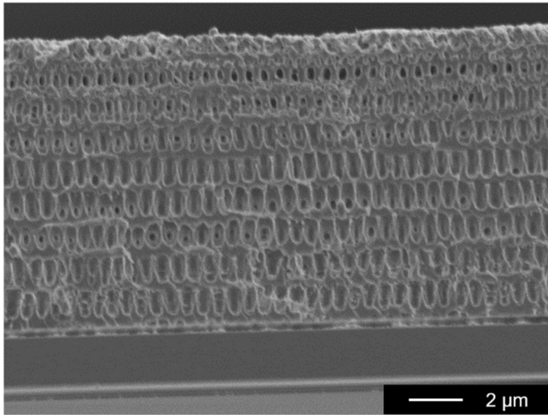

Figure 2.30. Cross-sectional SEM image of condition (a).

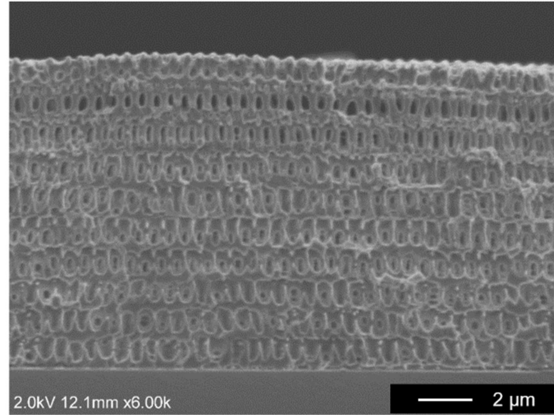

Figure 2.31. Cross-sectional SEM image of condition (b).

post-exposure-bake step was performed at 65°C for 7 min. The SEM cross-section observation is shown in Fig. 2.30–2.33. Condition (a) shows that only partially complete nanostructures are formed on the upper part of the film. The nanostructures on the surface did not reach to an ideal structure which should be isolated pillars (Fig. 2.30). As for condition (b), the formed layer of the nanostructure increased to 4 and the isolated pillars on the surface can be observed partially (Fig. 2.31). Both of these two conditions cannot form 3D nanostructures from the surface to the bottom and is most probably due to the insufficient soft-bake time, which means the solvent inside the photoresist is not being removed adequately (including water in the air because of high humidity). Afterwards, soft-bake time was increased in condition (c) and condition (d). From the SEM observation in Fig. 2.32, 3D nanostructures were fabricated with around 6–8 layers throughout the whole film and the surface structure was also very intact except for some collapse parts. Figure. 2.33 has the similar results with Fig. 2.32.

After the above optimization process, the soft-bake process was basically

fixed at 65°C for 30/40 min and at 95°C for 30/40 min.

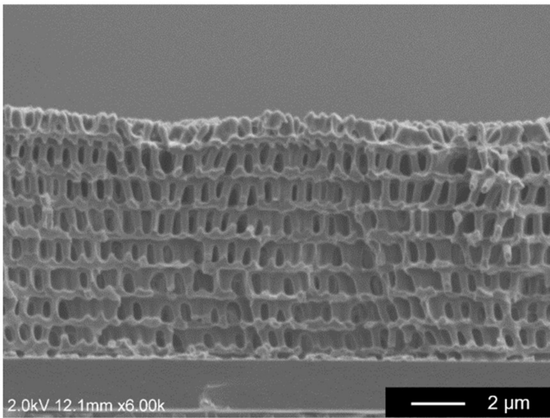

Figure 2.32. Cross-sectional SEM image of condition (c).

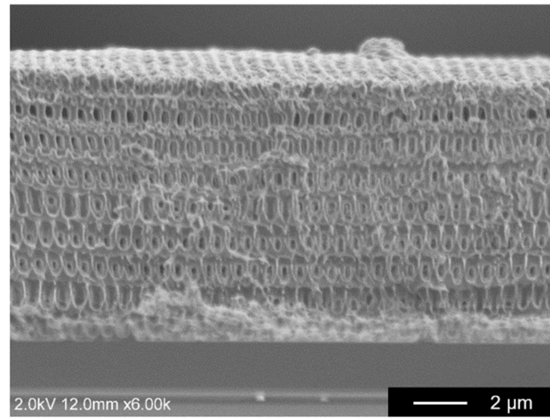

Figure 2.33. Cross-sectional SEM image of condition (d).

2.3.3 Effects of different UV exposure conditions

For the UV exposure conditions, the best soft-bake conditions (c) and (d) in the above section were used and the laser system in Fig. 2.8 without pinhole was used to confirm the reproducibility of the experiment. The results are shown in Fig. 2.34 and Fig. 2.35, respectively. However, due to the fluctuation and uneven distribution of laser energy, nanostructures are

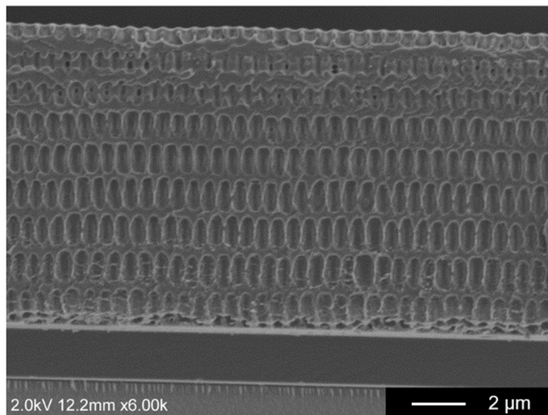

Figure 2.34. Cross-sectional SEM image of condition (c).

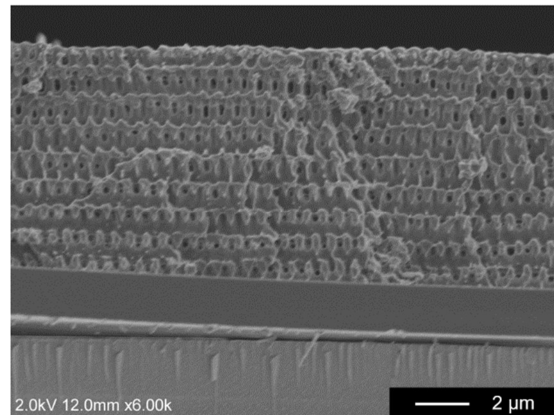

Figure 2.35. Cross-sectional SEM image of condition (d).

not well formed. Comparing these two results, it is found that the nanostructure is clearer under the condition of soft-bake for 40 min. Therefore, 40 min soft-bake was set as a fixed condition in subsequent experiments. After adding the pinhole to make the energy more uniform, the 40 min soft-bake and exposure energy of 15 mJ/cm^2 was used to fabricate nanostructures. Figure. 2.36 shows that the nanostructure still cannot be formed which may be due to overexposure, because the irradiation intensity becomes stronger at the center due to the setting of pinhole. To obtain the most ideal exposure dose, the fluence was reduced to 14, 12, 10, 9, 8, 7, 6,

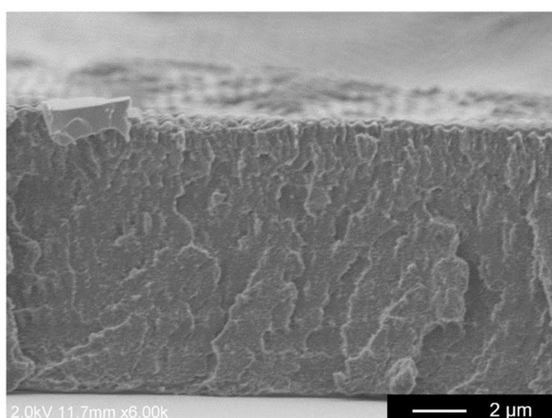

Figure 2.36. Cross-sectional SEM image of 15 mJ/cm^2 exposure doses.

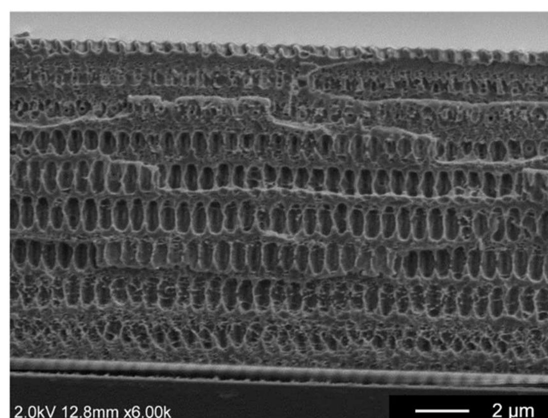

Figure 2.37. Cross-sectional SEM image of 14 mJ/cm^2 exposure doses.

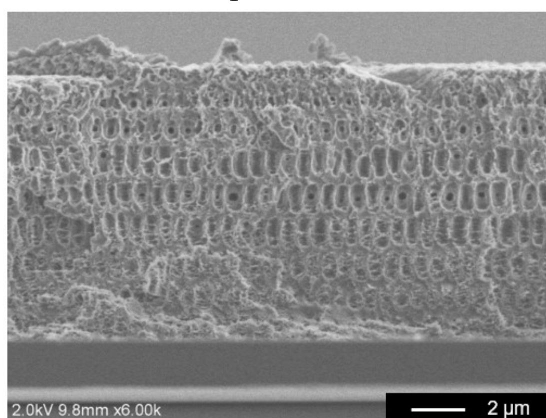

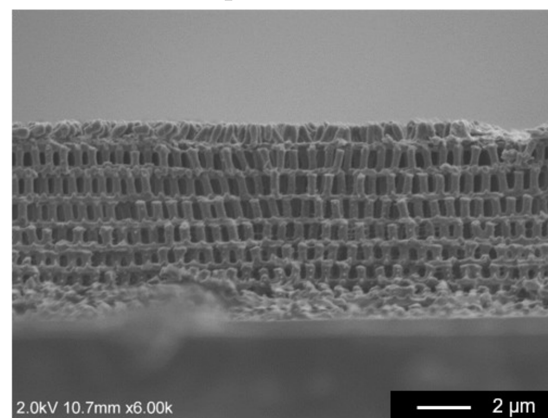

Figure 2.38. Cross-sectional SEM image of 12 mJ/cm^2 exposure dose (left: center of sample, right: edge of sample).

and 5 mJ/cm^2, respectively. As shown in Fig. 2.37, when the exposure dose decreased to 14 mJ/cm^2, the nanostructure is formed on the surface due to imprinting which originates from pressing the glass during the exposure step. Although part of the nano-holes are shown in the image, the nano-holes are not formed deep in the in-plane direction. Therefore, it is speculated that this is still caused by excessive exposure. When it was reduced at 12 mJ/cm^2, the edge of the sample exhibited partial nanostructure formation (Fig. 2.38). Once the exposure dose is decreased further to 10 mJ/cm^2, the periodic nanostructure can be formed in a wide range, is around 70–80% of the entire

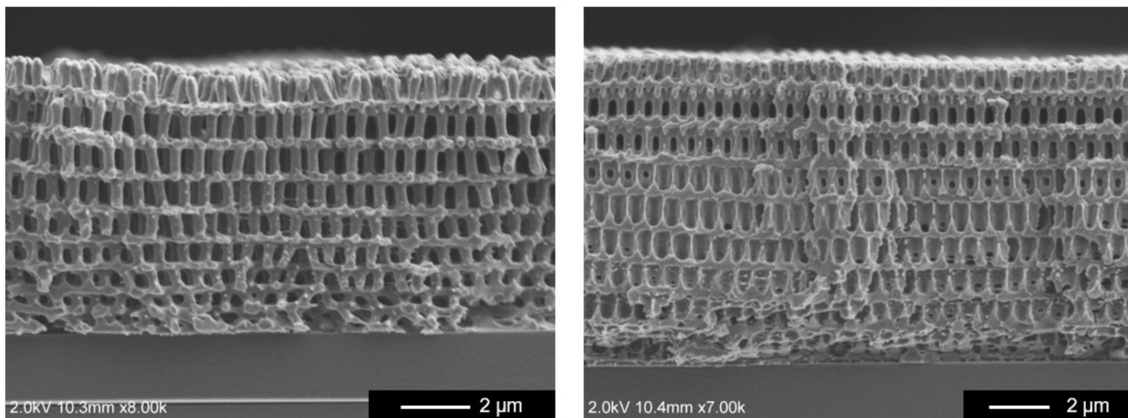

Figure 2.39. Cross-sectional SEM image of 10 mJ/cm^2 exposure dose (left: well-formed, right: not well-formed).

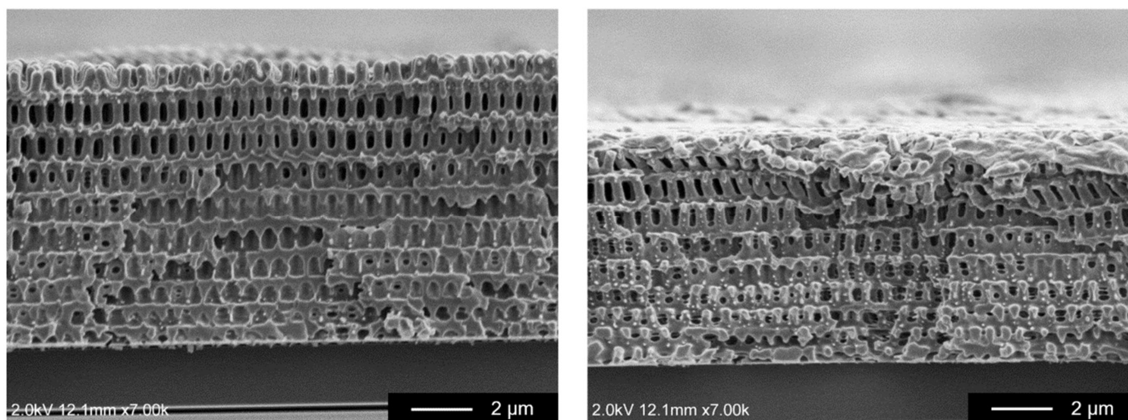

Figure 2.40. Cross-sectional SEM image of 9 mJ/cm^2 exposure dose (left: well-formed, right: not well-formed).

sample (Fig. 2.39). The exposure doses of 9 mJ/cm^2 (Fig. 2.40) and 8 mJ/cm^2 (Fig. 2.41) also result in well-formed nanostructures similar to that in Fig.

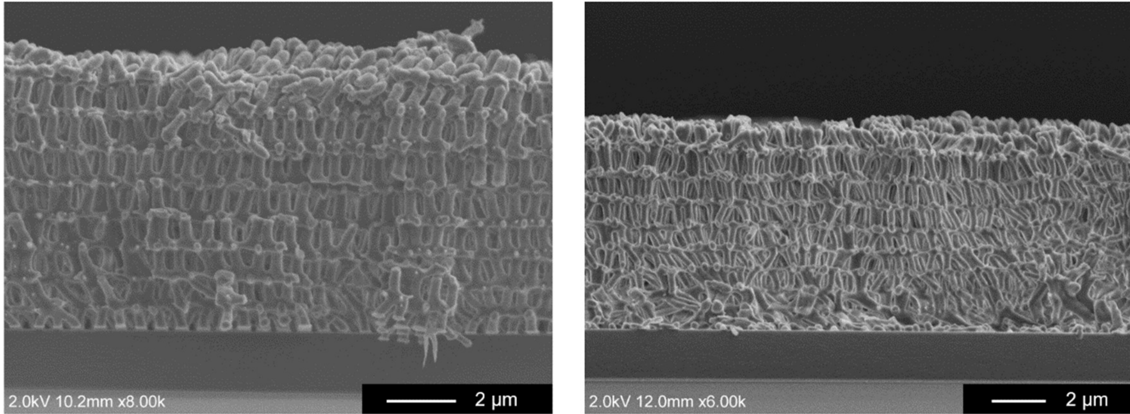

Figure 2.41. Cross-sectional SEM image of 8 mJ/cm^2 exposure dose (left: well-formed, right: not well-formed).

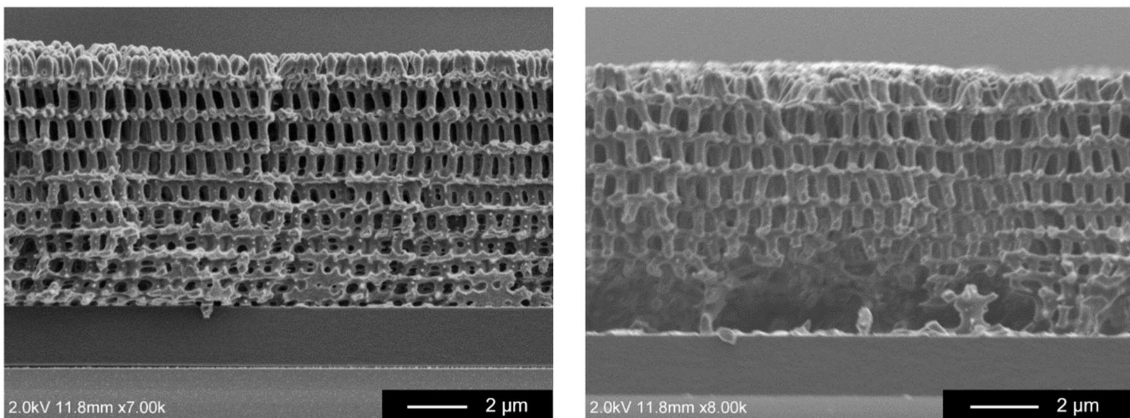

Figure 2.42. Cross-sectional SEM image of 7 mJ/cm^2 exposure dose (left: well-formed, right: not well-formed).

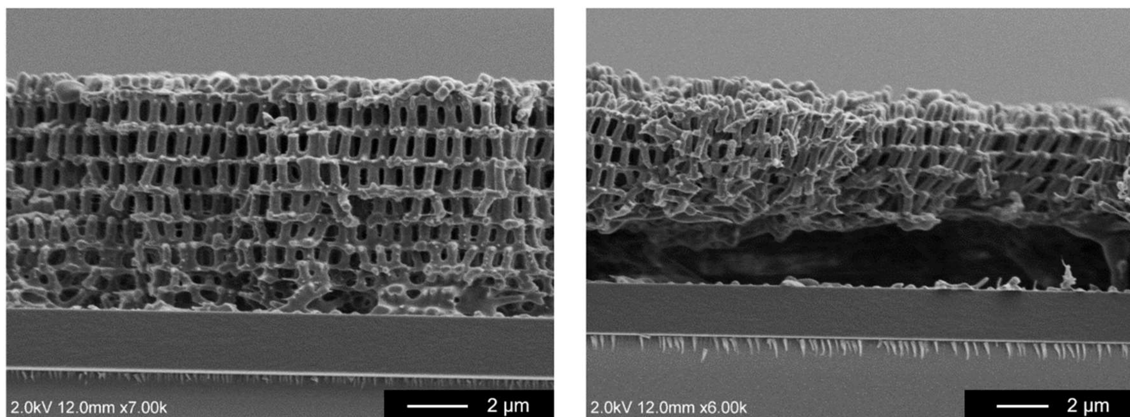

Figure 2.43. Cross-sectional SEM image of 6 mJ/cm^2 exposure dose (left: well-formed, right: not well-formed).

2.39. Nevertheless, the bottom nanostructure in Fig. 2.40 and the pillar nanostructure on the top in Fig. 2.41 are not as good as that in Fig. 2.39. Nanostructures can also be fabricated at the exposure dose lower than 8

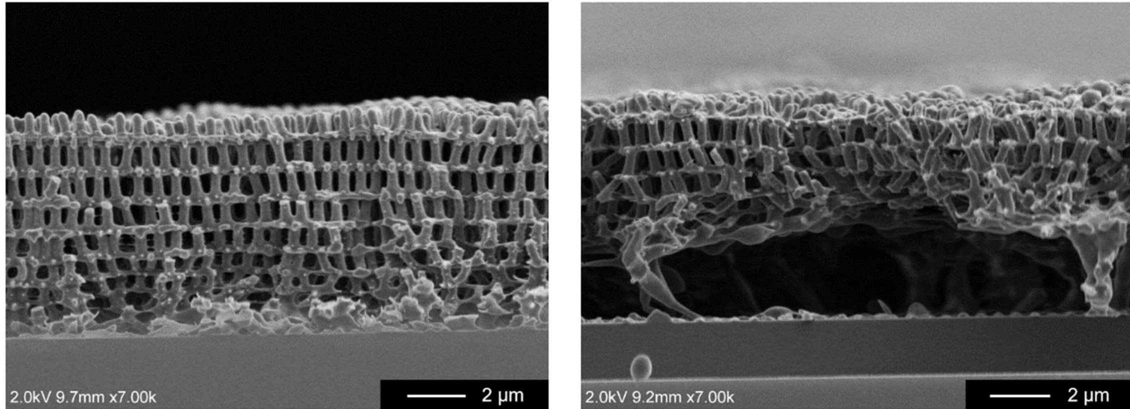

Figure 2.44. Cross-sectional SEM image of 5 mJ/cm^2 exposure dose (left: well-formed, right: not well-formed).

mJ/cm^2, as shown in Fig. 2.42–2.44. However, due to insufficient exposure, most of the nanostructures at the bottom of each sample were removed by the developing process and voids were formed at the same time.

In conclusion, the exposure dose at 10 mJ/cm^2 is the best condition to fabricate 3D nanostructure at current stage. It is important to note that the exposure dose maybe different due to differences in regions, environments, and equipment.

2.3.4 Reproducibility of SU8 3D nanostructures

The reproducibility experiment was processed with all these optimized conditions, which have been listed in Sec. 2.3.1. Basically, 70–80% of the 2.1 cm × 2.1 cm sample can be well fabricated with periodic 3D nanostructures as shown in Fig. 2.45. The remaining part has problems such

as collapsed structure (Fig. 2.46), incomplete structure (Fig. 2.47), and voids (Fig. 2.48).

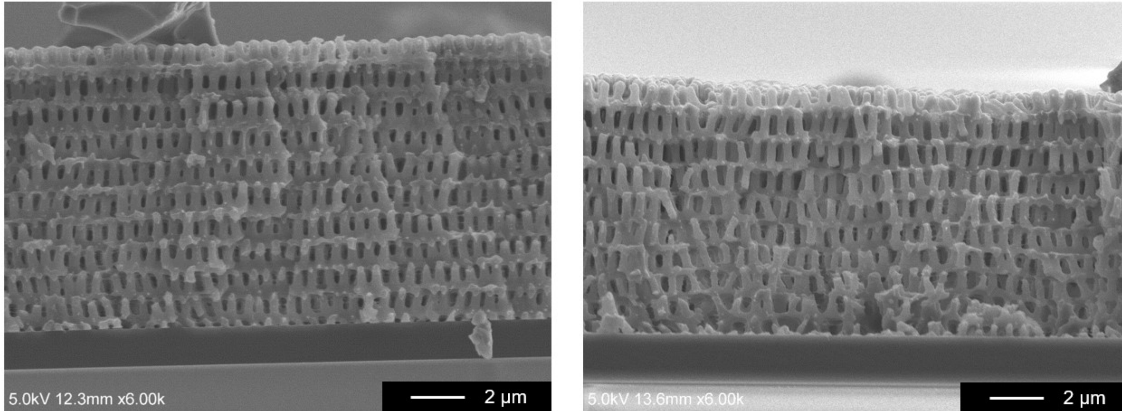

Figure 2.45. Cross-sectional SEM image of well fabricated 3D periodic nanostructure.

There are several reasons for these problems:

① Dust particles in the film entered during the fabrication process.

② Insufficient exposure or overexposure.

③ Pattern damage or defect in the PSM.

④ Improper cutting techniques of the sample before SEM observation.

Correspondingly, it needs to keep the samples as clean as possible during the fabrication process, while making the energy distribution of the laser beam more uniform and stable. For the PSM, it is strongly recommended to remake it after being used for multiple times. Regarding the observation method, it is suggested to observe the cross-section images after cutting the sample through focused ion beam (FIB) instead of cutting by diamond pen, to reduce the errors of manual operation.

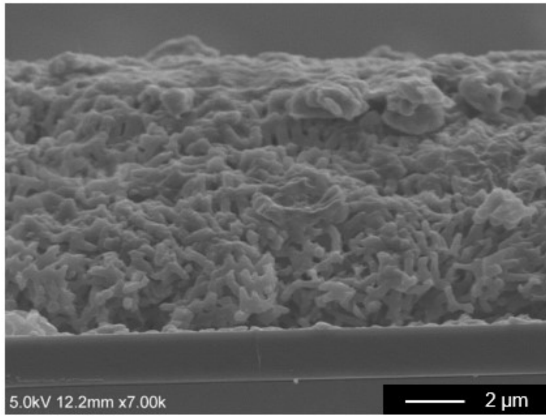

Figure 2.46. Cross-sectional SEM image of collapsed structure.

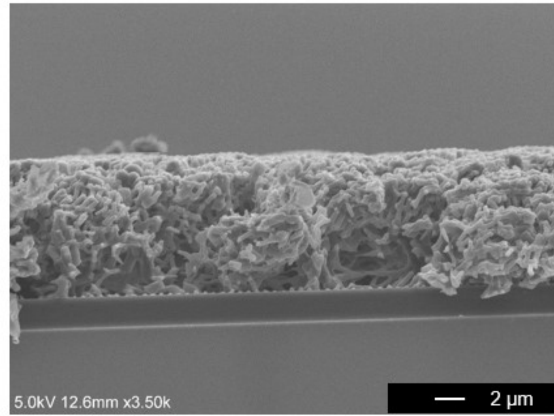

Figure 2.47. Cross-sectional SEM image of incomplete structure.

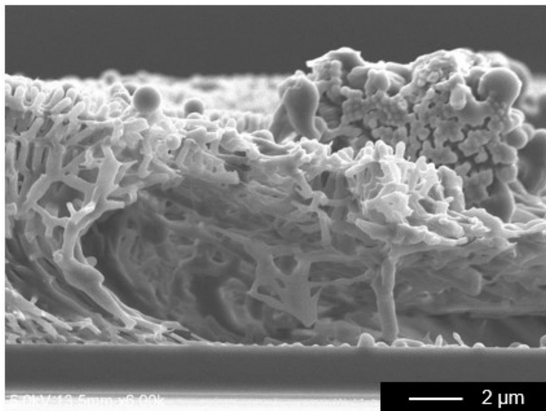

Figure 2.48. Cross-sectional SEM image of voids inside the structure.

2.4 Characteristic comparison of KMPR & SU8 3D nanostructures

2.4.1 Talbot distance

As described in Sec. 2.1.1, Talbot distance (Z_T) is the most essential evaluation parameter of Talbot effect. Hereafter, the theoretical value can be calculated and compared them with the measured value of the fabricated nanostructure, so that the shrinkage rate of this nanostructures can be

obtained. This is very important for the theoretical simulation of related thermoelectric characteristics. To calculate the theoretical Z_T, Eq. 2.1 and 2.2 in Sec. 2.1.1 are integrated as follows (Eq. 2.4). Here, λ_0= 355 nm, n_m= 1.66 for SU8, n_m= 1.62 for KMPR, and p= 600 nm.

$$Z_{\mathrm{T}} = \frac{\lambda_0/n_m}{1-\sqrt{1-\left(\frac{\lambda_0}{n_m \cdot p}\right)^2}} \tag{2.4}$$

For the Z_T in nanostructures, this is expressed by the periodicity in the out-of-plane direction shown in the inset in Fig. 2.49. 100 different locations

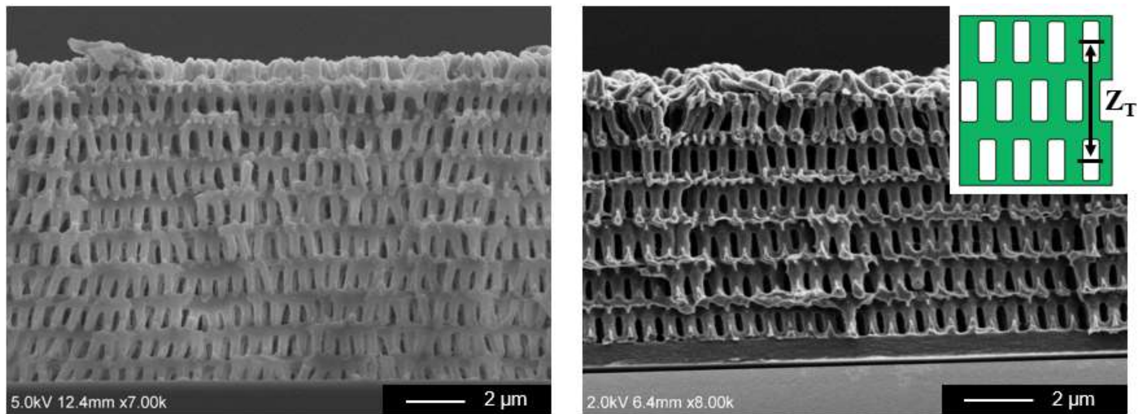

Figure 2.49. Cross-sectional SEM image of measured samples and method (left: SU8, right: KMPR).

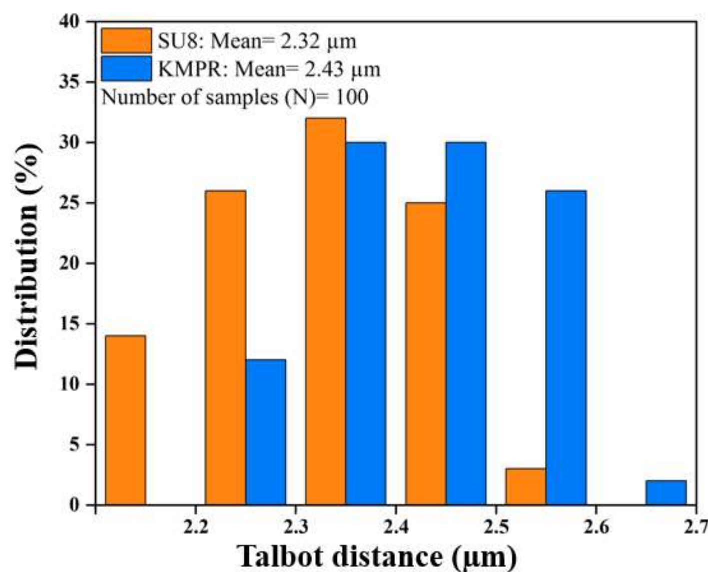

Figure 2.50. Measured Z_T of KMPR and SU8 3D nanostructures.

of Z_T were chosen from one sample (Fig. 2.49) to have a more accurate measurement value.

Z_T of KMPR and SU8 were summarized in Fig. 2.50. It was presented that the Z_T of KMPR was close to the range of 2.2–2.6 μm, and SU8 was close to the range of 2.1–2.5 μm. In order to more intuitively evaluate the shrinkage of the nanostructures, the shrinkage factor is calculated by

$$Shrinkage\ \ factor = \frac{[Z_T(theoretical) - Z_T(nanostructure)]}{Z_T(theoretical)} \tag{2.5}$$

The KMPR nanostructures had a lower shrink factor than SU8. However, large shrinkage still remains as shown in Table 2.4.

Table 2.4. Theoretical calculation value of Z_T, average of the measured Z_T, and the shrinkage factor for KMPR, SU8 reference and SU8 nanostructures.

	Talbot distance (μm)	Shrinkage factor (%)
Theoretical (SU-8)	3.23	—
SU-8 nanostructure ref [28]	2.31	29.2 ± 1.4
SU-8 nanostructure	2.32	28.2 ± 0.3
Theoretical (KMPR)	3.17	—
KMPR nanostructure	2.43	23.3 ± 0.3

By using the same PSM, this work can confirm that SU8 nanostructure that was fabricated are similar with the previous research result (SU8-ref), and the Talbot distance is also comparable [28]. Both aforementioned points explain that the SU8 nanostructure formed in this system have high reproducibility. Regarding the shrinkage of both KMPR and SU8, the crosslink density of the photoresist under the development and drying processes was postulated as the reason which caused the shrinkage [29]. It is also speculated that high epoxy resin contents in the KMPR photoresist make

it have a lower shrinkage factor compared to SU8, by increasing the crosslink density.

2.4.2 The height and periodicity of the nanostructures

The height and periodicity of the nanostructures were used to better evaluate the whole nanostructures. The x-direction distance of two adjacent nanoholes as the periodicity, and the y-direction distance as the height are presented in Fig. 2.51. 100 points were also measured in one sample from the SEM images shown in Fig. 2.49 to get an average value.

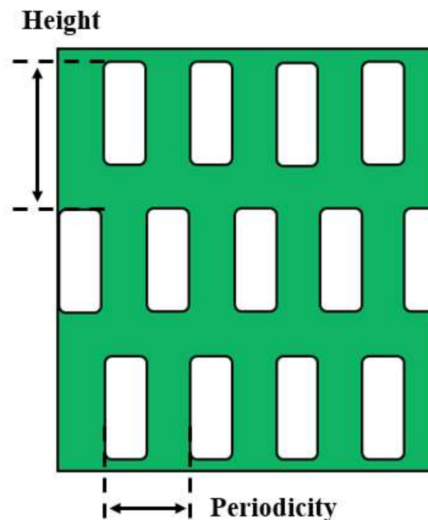

Figure 2.51. Schematic for height and periodicity in nanostructure.

From the histogram for KMPR, SU8 and SU8-ref, the difference in the measured values of the structural dimensions can be observe. Figure. 2.52 presents the heights of SU8 nanostructures which are mostly distributed in the range of 1000−1375 nm and concentrated in the range of 1000−1200 nm. It seems that the heights of SU8-ref nanostructures are more concentrated

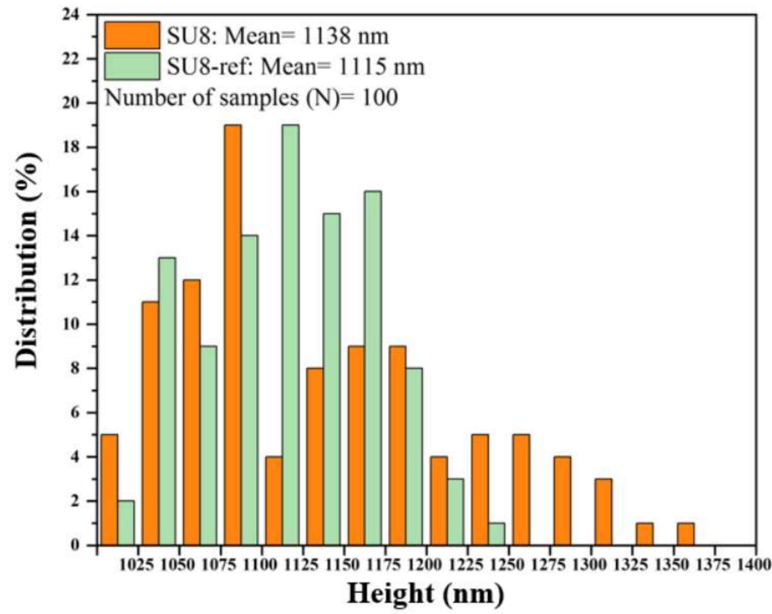

Figure 2.52. Distribution of nanostructures height (SU8 &SU8-ref).

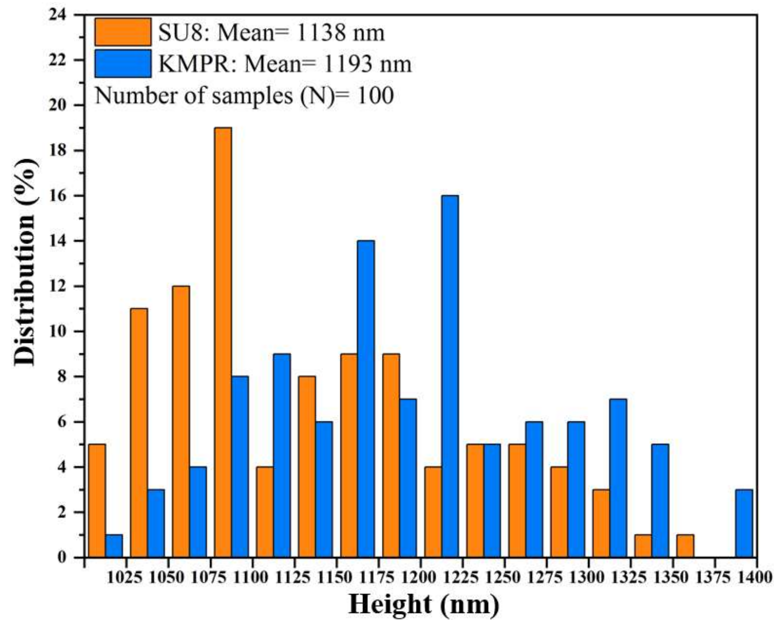

Figure 2.53. Distribution of nanostructures height (SU8 & KMPR).

than SU8, which is caused by the highly uniform energy distribution of the laser system used in the reference [30]. For the height distribution of KMPR nanostructures, they are concentrated in the range of 1075–1225 nm, and distributed in the range of 1000–1400 nm (Fig. 2.53). It indicates that the height shrinkage happened in both photoresists. The KMPR nanostructures

have a lower shrinkage factor compared to the SU8 nanostructures which is the reason why the KMPR height increased. Moreover, both SU8 and KMPR nanostructure heights fabricated in this study are more dispersed than that of SU8-ref. It is speculated that due to the energy attenuation and problems with beam uniformity caused by pulsed laser beam expansion and distance increase. On the other hand, the reproducibility of the PnP process was similarly demonstrated as the SU8-ref.

The periodicity distribution of these two photoresists is shown in Fig. 2.54–2.55. SU8 formed in this study has a larger distribution range from 425–725 nm and concentrate in the range of 500–625 nm. On the contrary, both SU8-ref and KMPR are centralized in the range of 525–625 nm. According to the summary of the average values of height and periodicity for SU8, SU8-ref, and KMPR in Table 2.5, the periodicity distribution of both KMPR and SU8 are within the margin of error. The reason why SU8

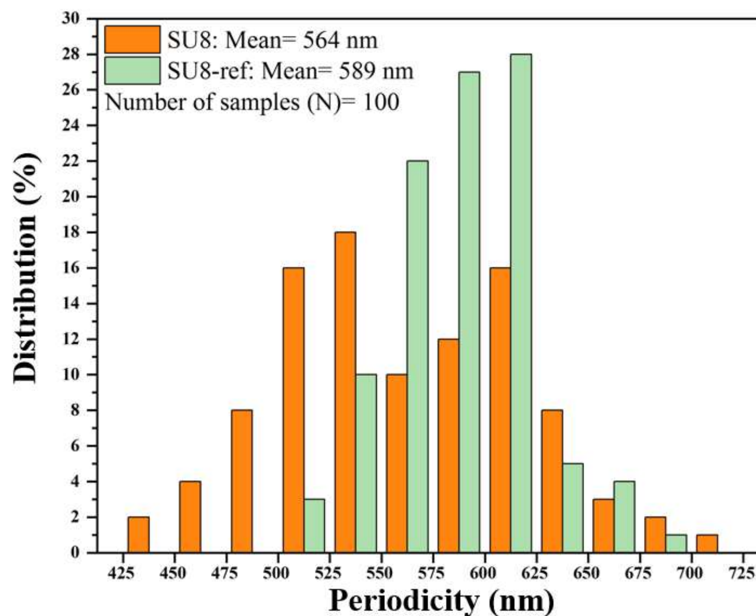

Figure 2.54. Distribution of nanostructures periodicity (SU8 &SU8-ref).

have a larger distribution is probably due to systemic errors in the PSM and laser system.

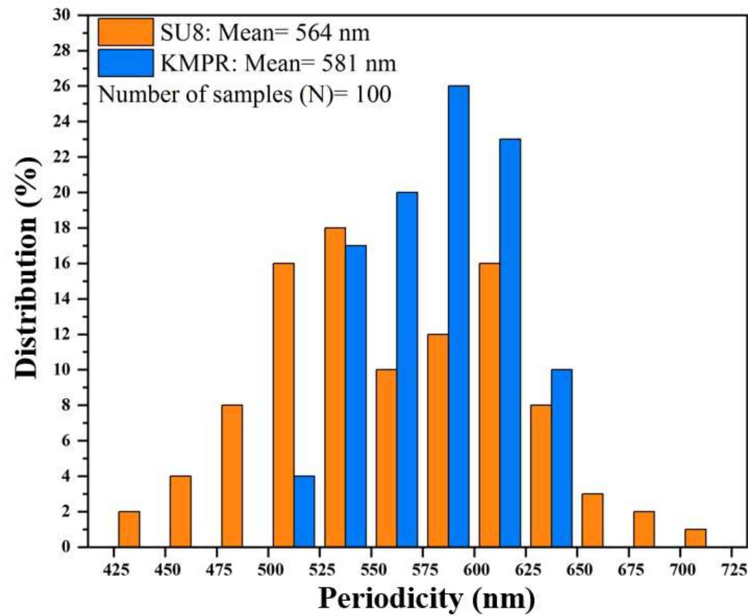

Figure 2.55. Distribution of nanostructures periodicity (SU8 & KMPR).

Table 2.5. Average values of the structure's height, periodicity and shrinkage factors for SU8, SU8 ref and KMPR nanostructures.

Structures	Height (nm)	Periodicity (nm)
SU-8 template	1138 ± 85.6	564 ± 58
SU-8 ref template [28]	1115	589
KMPR template	1193 ± 86.4	581 ± 33.1

In conclusion, KMPR and SU8 3D nanostructures were successfully fabricated in this study by using the same PSM with the reference. However, the height and periodicity of the structure is not controlled as the SU8-ref because of the shrinkage of the photoresist, and instability of the pulsed laser energy. Nevertheless, the distribution analysis still shows a strong orderliness in height and periodicity of the nanostructure which can be expected to produce a 3D inverse nanostructure.

2.5 Summary

In this chapter, the PnP process was introduced, then the fabrication conditions of two kinds of negative photoresists was optimized, the laser irradiation system was constructed, and the 3D periodic nanostructures were fabricated. As a consequence, the important findings as follows were obtained:

(a) Conformal contact is very important to form 3D periodic nanostructures which means high uniformity photoresist surface are required. Otherwise, the highly ordered intensity distribution will be hard to achieve.

(b) Laser irradiation system is another core part of PnP process, when overexposed, the photoresist will be fully solidified making it difficult to form nanostructures. When the exposure dose is not enough, the photoresist will be removed during the developing step. At the same time, different photoresists have different exposure doses to fabricate nanostructures, therefore optimization process are also crucial.

(c) Due to the cross-linking density during the developing and drying process and the shrinkage of the photoresist itself, the in-plane and out-of-plane direction shrinkage of the nanostructures were confirmed as well [31]. This fabrication process optimization and shrinkage evaluation will be very useful information for future nanostructure design and theoretical calculation of thermal conductivity.

References

[1] S. Jeon, J. –U. Park, R. Cirelli, S. Yang, C. E. Heitzman, P. V. Braun, P. J. A. Kenis, and J. A. Rogers, PNAS., 101, No.34, 12428 (2004)

[2] S. Jeon, D. J. Shir, Y. S. Nam, R. Nidetz, M. Highland, D. G. Cahill, J. A. Rogers, M. F. Su, I. F. El-Kady, C. G. Christodoulou, and G. R. Bogart, Opt. Express., 15, No.10, 6358 (2007)

[3] D. Shir, H. –w. Liao, S. Jeon, D. Xiao, H. T. Johnson, G. R. Bogart, K. H. A. Bogart and J. A. Rogers, Nano. Lett., 8, No.8, 2236 (2008)

[4] E. Menard, M. A. Meitl, Y. –G. Sun, J. –U. Park, D. J. –L. Shir, Y. –S. Nam, S. Jeon, and J. A. Rogers, Chem. Rev., 107, No.4, 1117 (2007)

[5] T. T. Truong, R. –S, Lin, S. Jeon, H. H. Lee, J. Maria, A. Gaur, F. Hua, I. Meinel, and J. A. Rogers, Langmuir., 23, No.5, 2898 (2007)

[6] H. F. Talbot, Philos. Mag., 9, No.51, 401 (1836)

[7] A.Isoyan, F. Jiang, Y. C. Cheng, and F. Cerrina, J. Vac. Sci. Technol. B., 27, No.6, 2931 (2009)

[8] H. H. Sloak, C. Dais, and F. Clube, Opt. Express., 19, No.11, 10686 (2011)

[9] M. –S Kim, T. Scharf, C. Menzel, C Rockstuhl, and H. P. Herzig, Opt. Express., 20, No.5, 4903 (2012)

[10] J. –M. Wen, Y. Zhang, and M. Xiao, Adv. Opt. Photonics., 5, No.1, 83 (2013)

[11] L. Stuerzebecher, T. Harzendorf, U. Vogler, U. D. Zeitner, and R. Voelkel, Opt. Express., 18, No.19, 19485 (2010)

[12] P. Latimer, and R. F. Crouse, Appl. Opt., 31, 80 (1992)

[13] S. Jeon, Y. –S. Nam, D. J. –L. Shir, and J. A. Rogers, Appl. Phys. Lett., 89, No.25, 253101 (2006)

[14] D. Chanda, L. Abolghasemi, and P. R. Herman, Opt. Express., 14, No.19, 8568 (2006)

[15] J. A. Rogers, K. E. Paul, R. J. Jackman, and G. M. Whitesides, J. Vac. Sci. Technol. B., 16, No.1, 59 (1998)

[16] Shinji Araki, Nara Institute of Science and Technology Doctor's Thesis (2016)

[17] X. D. F. Wang, Y. Ishikawa, S. Araki, M. Uenuma, and Y. Uraoka, Jpn. J. Appl. Phys., 58, SDDF08 (2019)

[18] Eric, Anslyn; Dougherty, Dennis. Modern physical organic chemistry. University Science Books.

[19] H, Ito, C. G. Willson, and J. H. J. Frechet, Symposium on VLSI Technology, Digest of Technical Papers., 86 (1982)

[20] D. J. Shir, S. Jeon, H. –W. Liao, M. Highland, D. G. Cahill, M. F. Su, I. F. El-Kady, C. G. Christodoulou, G. R. Bogart, A. V. Hamza, and J. A. Rogers, J. Phys. Chem. B., 111, No.45, 12945 (2007)

[21] J. –B. Kwon, K. Trivedi, N. V. Krishnamurthy, W. Hu, J. –B. Lee, and B. Gimi, J. Vac. Sci. Technol. B., 27, No.6, 2795 (2009)

[22] C. Ge, and E. Cretu, Micromachines., 11, No.3, 317 (2020)

[23] Y. W. Kwon, J. –Y. Park, T. –H. Kim, S. H. Kang, H. –W. Kim, J. –H. Shin, S. Jeon, and S. W. Hong, ACS. Nano., 10, No.4, 4609 (2016)

[24] KMPR 1000 Chemically Amplified Negative Photoresist, MicroChem

[25] Report No.26, Joint Assessment of Commodity Chemicals, “Linear Polydimethylsiloxanes” (1994)

[26] J. K. Hyun, J. –Y. Park, E. –H. Kim, L. J. Lauhon, and S. Jeon, Adv. Optical Mater., 2, No.12, 1213 (2014)

[27] J. –Y. Park, J. –W. Seo, H. K. Jung, G. Hyun, S. Y. Park, and S. Jeon, Adv. Funct. Mater., 26, No.39, 7170 (2016)

[28] S. Araki, Y. Ishikawa, X. D. F. Wang, M. Uenuma, D. –H. Cho, S. Jeon and Y. Uraoka, Nanoscale Res. Lett., 12, No.419 (2017)

[29] J. –Y. Park, K. –I. Kim, K. Kim, D. –C. Kim, D. –H. Cho, J. H. Lee, and S. Jeon, Adv. Mater., 27, No.48, 8000-6 (2015)

[30] J. –Y. Park, D. –H. Tahk, C. –G. Ahn, S. G. Im, S. –J. Choi, K. –Y. Suh, and S. Jeon, J. Mater. Chem. C., 2, No.13, 2316 (2014)

[31] R. C. Rumpf and E. G. Johnson, J. Opt. Soc. Am. A., 21, No.9, 1703 (2004)

Chapter.3 Fabrication of 3D periodic ZnO nanostructure via infiltration process

3.1 Introduction

ZnO is potentially low-cost and nontoxic n-type semiconductor that can be expected to be used in the field of thermoelectricity, which has a relatively high Seebeck coefficient (S) among the metal oxides. With different carrier concentration, S can be controlled from -100 μV/K to -400 μV/K [1]. At the same time, it has a wide working range that covers mid to high temperatures, even over 1027ºC at which the ZnO still can keep stable in air [2]. And it also has good transparency, high electron mobility, and wide bandgap [3−5], which attracts lots of interests from many fields such as sensors, transparent electrodes, and transistors [6–8].

The reasons why ZnO is challenging material for the thermoelectric application are the relatively high thermal conductivity (κ) and low electrical conductivity (σ) [9]. In recent years, ZnO doping with other elements caught an interest in the thermoelectric field, which can overcome those shortcomings. For example, ZnO doping with Al and Ga can achieve a high figure of merit (*ZT)* around 0.6 at 1000°C [10] and a nanocomposites with Al-doped ZnO had a ZT around 0.44 at 727ºC [11], however both those approaches are required high-temperature, high-pressure, and high-vacuum processes such as atomic layer deposition (ALD) or chemical vapor deposition (CVD). Moreover, the additional reactive ion etching (RIE) may also be required to remove an excess overlayer [12−14].

For pure ZnO, since ZT of ~1.4×10^{-4} at near room temperature is almost negligible [15], the best improvement approach is introduce nanostructures inside. Such as nanoparticles, nanowires, nanomeshes, and superlattices, which can decrease the thermal conductivity via enhance phonon-boundary scattering [15–19]. Kim's research used ALD to deposit ZnO inside the nanostructure and discussed the thermal properties with 3D periodic nanostructure, which have an obvious decrease of the κ, therefore ZT was also improved to a considerable degree (Fig. 3.1) [20]. On the contrary,

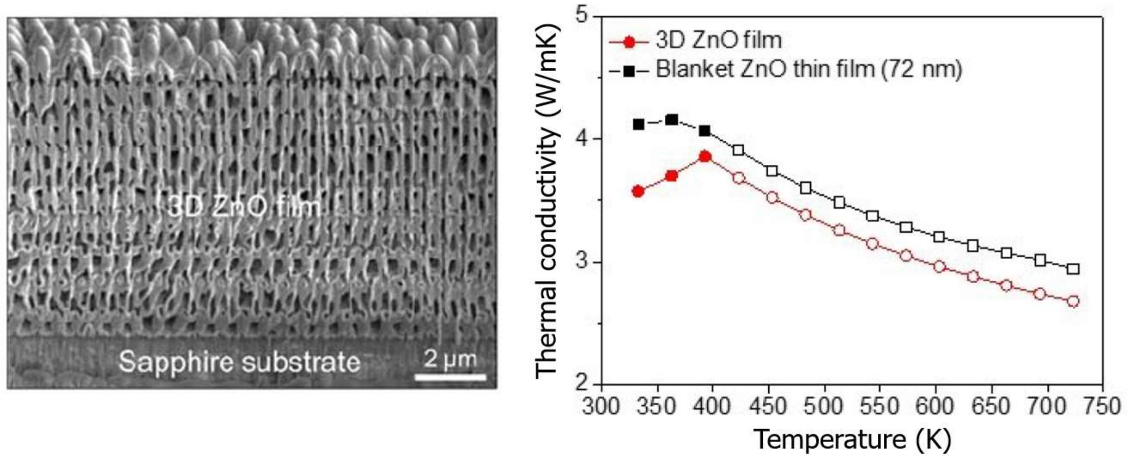

Figure 3.1 ZnO nanostructures formed with ALD [20] wherein the filled circles and squares indicate the measured values, and the open circles and squares are the estimated values by using the Debye-Callaway model.

Huang's research fabricated an inverse ZnO photonic crystal structures with sol-gel reaction which is a non-vacuum process [21].

In this chapter, the 3D periodic nanostructures fabricated in Chap. 2 were used as a template to form ZnO inverse 3D nanostructures by a liquid infiltration process which are non-vacuum and cost-effective [22–25]. Different from the complicated traditional methods, the nanostructure formed by infiltration process can be modified with different nanostructure templates. It is also expected to have low thermal conductivity as mentioned

in the first chapter. A metal organic decomposition (MOD) solution is used as a precursor for the ZnO solution (SYM-Zn20, Kojundo Chemical Lab.). The MOD solution is a metal organic compound which is dissolved in an organic solvent, and is capable of easily forming an oxide thin film by coating the solution on a substrate and performing heat treatment after drying [26]. In addition, the greatest merits of thin film production using MOD coating type materials are low material cost and low cost of production equipment. Another advantage is the excellent controllability of the composition ratio, which can improve the freedom of research. It should be noted that precipitation formation and viscosity increase may occur during the mixing of the solutions.

The previous research has discussed the possibility of using ZnO MOD solution (ZnO solution) to penetrate and fill nanostructures by capillary action. The work has shown that the fabrication of ZnO inverse 3D nanostructures with periodic structures is possible. From the experimental results, the necessary procedures of the infiltration process were identified. Although results showed that to maintain the original periodic ZnO inverse nanostructure without large-scale collapse and shrinkage, it is necessary to perform multi-cycle filling before removing the original nanostructure, which was used to form the framework of ZnO nanostructures. As the cycle number of filling increases, the thickness of the ZnO film will also be increased. After six filling cycles, the voids of the 3D nanostructure are filled completely. Similarly, the results showed that the ZnO inverse nanostructure produced a shrinkage rate of approximately 16%. This effect was observed

in both the height and the periodicity in the in-plane direction. Furthermore, the shrinkage of 36.8% of the periodicity in thickness direction was confirmed [25].

Nevertheless, reproducibility experiments could not obtain the same results due to the different nanostructure templates. Other factors include the uncertain dispensed amount of the ZnO solution and the shelf life of the solutions. In this study, the experimental processes were further optimized and identified. Moreover, the reproducibility was also verified. In the meantime, the changes and differences of the ZnO inverse nanostructure fabricated under different ZnO concentrations are also discussed.

3.2 Fabrication of 3D periodic ZnO nanostructure via infiltration process

3.2.1 Fabrication procedures of 3D periodic ZnO nanostructure

The fabrication of 3D periodic ZnO nanostructures via infiltration were carried out according to the following procedures:

(a) Preparation of ZnO solution

Move the ZnO solution out of the refrigerator and thaw for 15 min to bring the solution back to room temperature (RT). (Storage method: The ZnO solution is kept in a plastic bag under nitrogen gas and kept in a freezer to prevent degradation)

(b) Spin-coat

With a glass pipette that cannot control the dropping amount, drop the ZnO solution on the surface of the 3D nanostructure template. Then, spin-coat at 500 rpm for 5 sec and at 2000 rpm for 20 sec, to make the film uniform.

(c) Defoam

Put the samples inside a vacuum desiccator and defoam for 5 min via a diaphragm pump. This is done to remove bubbles in the solution to prevent the nanostructure from being destroyed as well as promote capillary action so that the ZnO solution can penetrate to the bottom layer of the nanostructure.

(d) Baking

Bake samples in O_2 atmosphere at 220°C for 1 h, solidify the ZnO precursor and form the nanostructure skeleton. The four steps mentioned above constitute a cycle. After performing at least 6 cycles, the voids in the nanostructure template can be completely filled to ensure the periodicity of the original nanostructure.

(e) Post-bake

This post-bake process is performed at 410°C for 4 h under O_2 atmosphere, which can completely solidify the ZnO while removing the original photoresist as much as possible.

3.2.2 Reproducibility of ZnO 3D inverse nanostructure with SU8 template

The conditions mentioned above which is based on the previous research were used to verify the reproducibility of the fabrication [16]. The 3D nanostructure templates similar with the previous research were also used. The filling cycles increased to 4, 5, and 6 times are also discussed respectively as shown in Fig. 3.3–3.5. From the cross-sectional SEM observations as seen in Fig. 3.3, ZnO nanostructures exhibit large shrinkage and collapsed sections. This implies that the periodicity is not be similar especially compared to the previous research. At the same time, large ZnO residues were found on the surface of the nanostructures. When the filling cycle was increased to 5, nanostructures similar to the previous research was obtained. However, the ZnO residues became thicker, which would have a big influence on the thermal properties of the device (Fig. 3.4). Figure. 3.5 presents the results for 6 filling cycles. As same as the previous result, a large amount of bulky ZnO residues remains on the structure surface while the voids of the ZnO nanostructures became bigger.

The above results indicate that the reproducibility of the experiment is low. The most probable reasons are as follows:

① The uncontrollable dispensed amount of ZnO solution in each drop.

② Due to systematic errors and uncontrollable dispensed amount of SU8, the 3D nanostructure template used every time is slightly different.

Even after the spin-speed was increased to 4000 rpm for 20 sec, the bulky

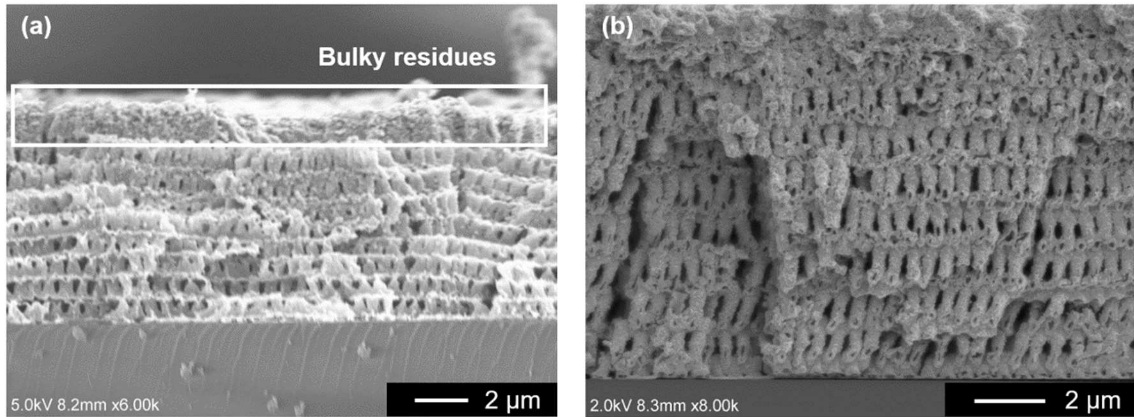

Figure 3.3 Cross-sectional SEM image of ZnO nanostructures with 4 cycles repeat,
(a): Reproduction experiment, (b): Previous research [16].

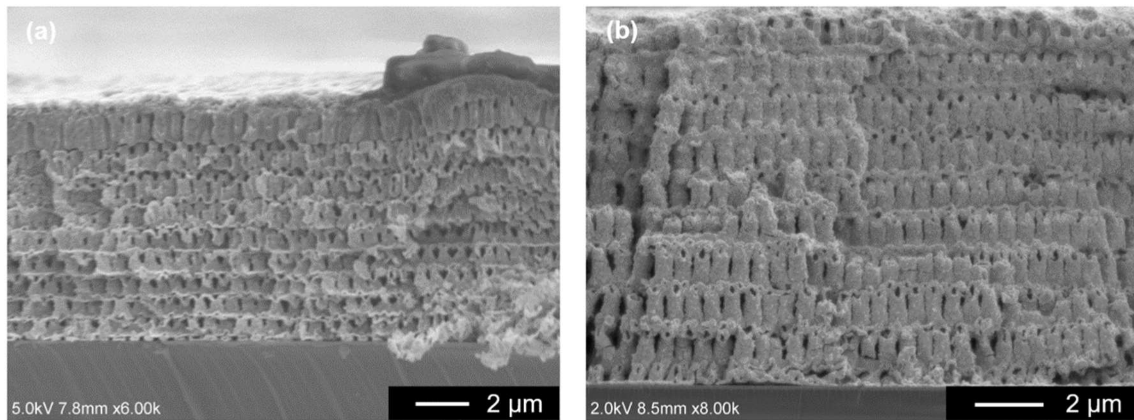

Figure 3.4 Cross-sectional SEM image of ZnO nanostructures with 5 cycles repeat,
(a): Reproduction experiment (b): Previous research [16].

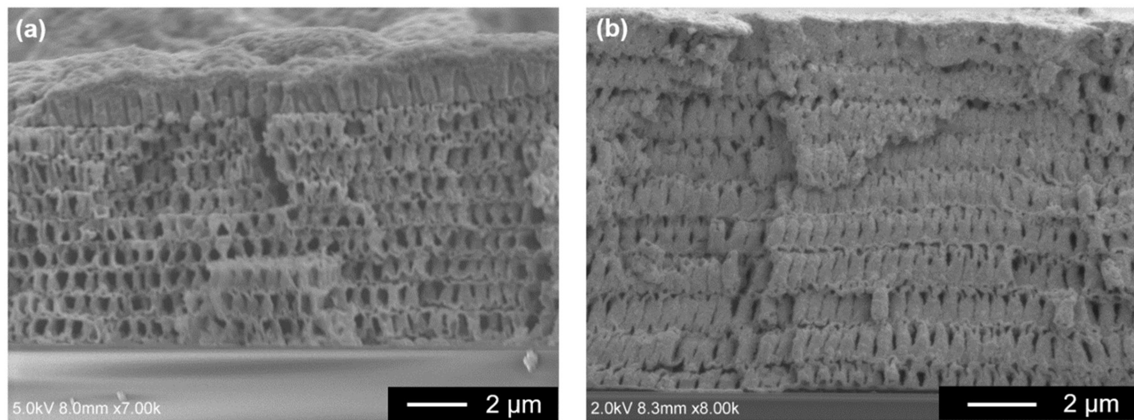

Figure 3.5 Cross-sectional SEM image of ZnO nanostructures with 6 cycles repeat,
(a): Reproduction experiment (b): Previous research [16].

ZnO residues still existed but the thickness decreased as demonstrated in Fig. 3.6–3.8. In view of the fact that the previous research reported that 6 cycles

are the best conditions for maintaining the film thickness of the original structure, this study decides 6 cycles as the basic conditions in the subsequent optimization experiments.

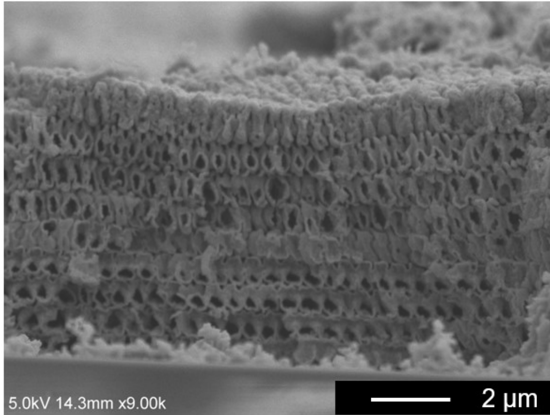

Figure 3.6 Cross-sectional SEM image of ZnO nanostructures with 4000 rpm/ 20 sec spin speed (4 cycles).

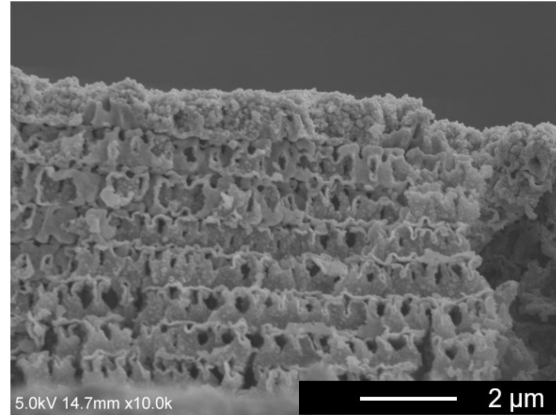

Figure 3.7 Cross-sectional SEM image of ZnO nanostructures with 4000 rpm/ 20 sec spin speed (5 cycles).

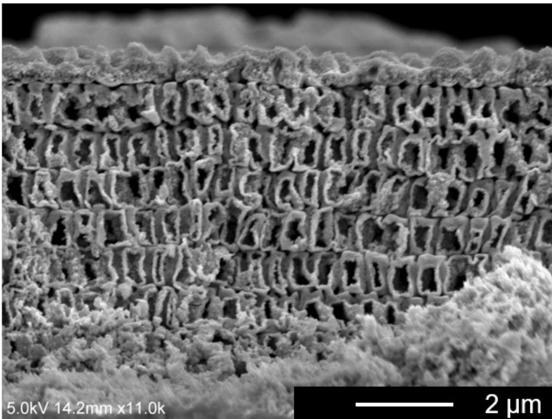

Figure 3.8 Cross-sectional SEM image of ZnO nanostructures with 4000 rpm/ 20 sec spin speed (6 cycles).

3.2.3 Optimization of infiltration process by using SU8 template

The SU8 3D periodic nanostructure template made in Chap. 2 was used, for the purpose of optimizing the infiltration process and maintaining the consistency of the conditions. Similar conditions described in Sec. 3.2.1 were

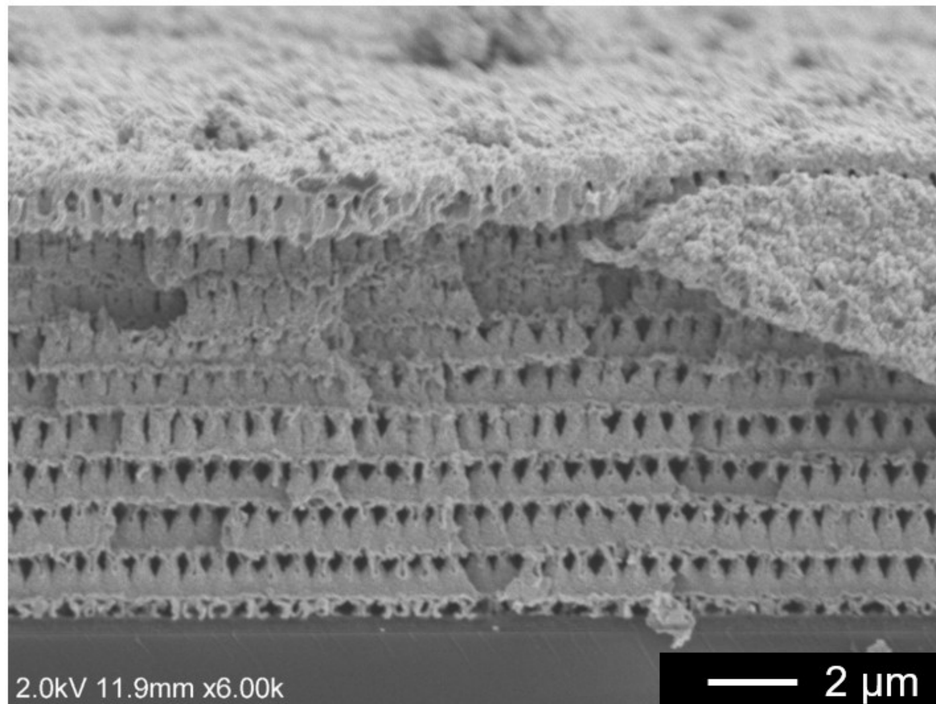

Figure 3.9 Cross-sectional SEM image of ZnO nanostructures formed with SU8 template. (6 cycles)

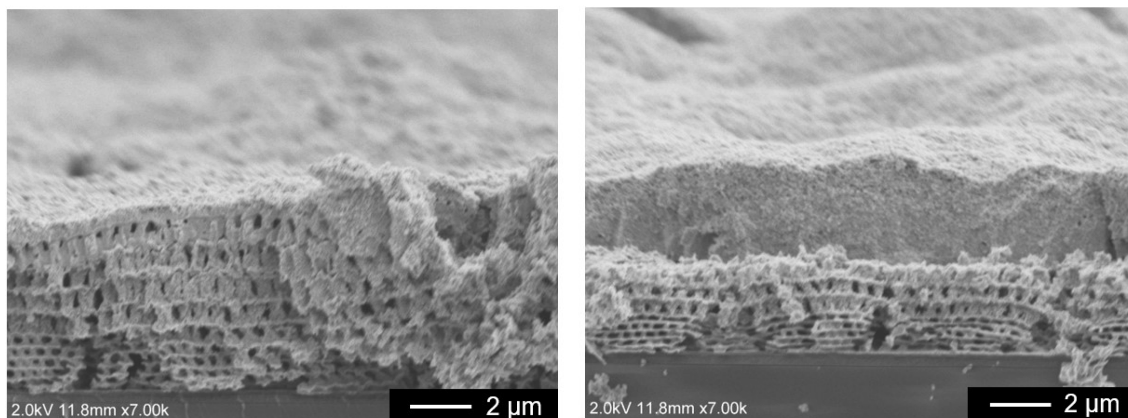

Figure 3.10 Cross-sectional SEM image of ZnO nanostructures formed with SU8 template. (6 cycles)

used to verify the feasibility of the template. As a result, the general structure and shape was comparable with the previous result, but the voids of structures were bigger (Fig. 3.9). It should be pointed out that the SU8 nanostructure template fabricated in Chap. 2 can be a good alternative template. On the other hand, the collapse, shrinkage, and agglomeration of the nanostructure still happens as shown in Fig. 3.10, which implies that further optimization of the infiltration process is required.

To get a more uniform 3D periodic ZnO nanostructure without any residues on the surface, the ZnO solution (2.0 mol/L) was diluted with a specialized diluent (ZnO thinner, Kojundo Chemical Lab) and a micropipette was also used to control the amount of liquid dispensed every time. Firstly, the ZnO concentration was decreased to 1.92 and 1.84 mol/L. This was done to confirm the feasibility of the diluted solution. At the same time, the amount of ZnO dispensed was set up to 10 μL while the SU8 template size was fixed within 1 cm × 0.5 cm. SEM images in Fig. 3.11 show that the ZnO nanostructures can be successfully fabricated. It can be observed that the

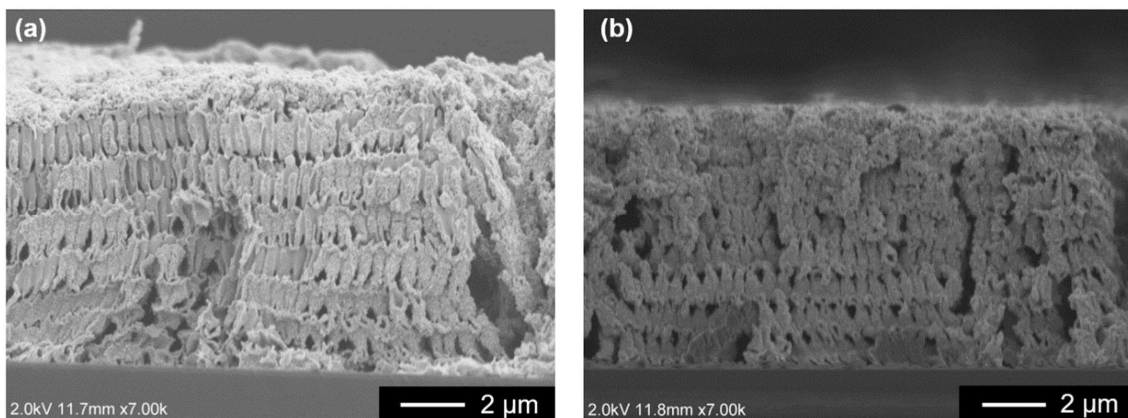

Figure 3.11 Cross-sectional SEM image of ZnO nanostructures formed with diluted ZnO solution, (a): 1.92 mol/L, (b): 1.84 mol/L.

surface residue is significantly reduced and thinner for these two concentrations. The results illustrate that this method is practical and effective. However, the residues-agglomerated and collapsed regions still exist.

It is highly possible that spin-coating the ZnO solution first may cause insufficient penetration time. This results in solution accumulation on the surface of the structure and forms agglomerates. Therefore, the defoaming process is performed before the spin-coating process and the defoaming time is increased to 5 min and repeated for 3 times. This facilitates the penetration of the ZnO solution into the nanostructure. Also, the ZnO solution was further diluted to 0.86 mol/L, 0.47 mol/L, 0.30 mol/L, and 0.23 mol/L. Under the new optimized conditions with 10 μL dropping amount, the ZnO nanostructures are formed as shown in Fig. 3.12–3.15. Overall, when the

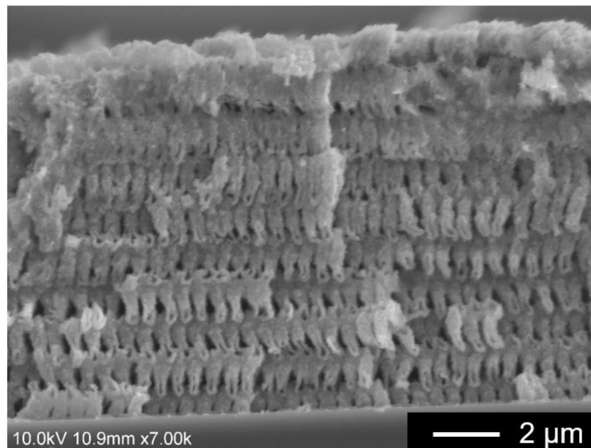

Figure 3.12 Cross-sectional SEM image of ZnO nanostructures formed with different concentration (0.86 mol/L).

defoaming process is carried out first and lower concentrations of ZnO solutions are used, the periodic nanostructure can be successfully fabricated, the period is more obvious, and the structure is more complete. Similarly,

with the decreasing concentration of ZnO, the bulky residues became thinner (Fig. 3.12). When the concentration reaches 0.47 mol/L, the bulky residues disappeared. In contrast with the previous research, the shape of the ZnO nanostructures improved and the voids became larger after optimization (Fig. 3.13). In order to confirm that ZnO was fully filled inside the nanostructure and the original template was completely removed, energy dispersive X-ray (EDX) mapping analysis was carried out. From the EDX mapping shown in Fig. 3.13–3.15, it can be observed that inverse ZnO nanostructures with high periodicity were formed, and the original SU8 template which was based on

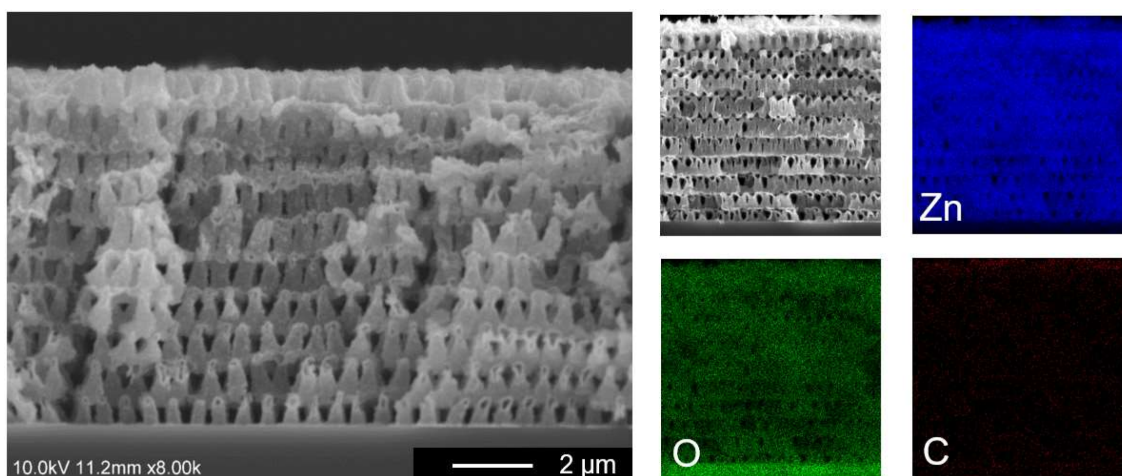

Figure 3.13 Cross-sectional SEM image of ZnO nanostructures (0.47 mol/L).

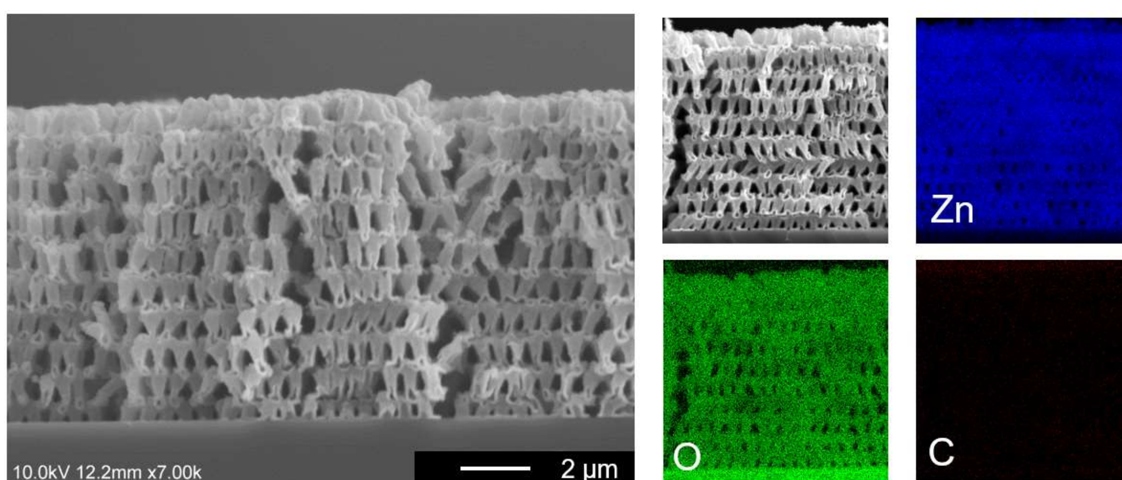

Figure 3.14 Cross-sectional SEM image of ZnO nanostructures (0.30 mol/L).

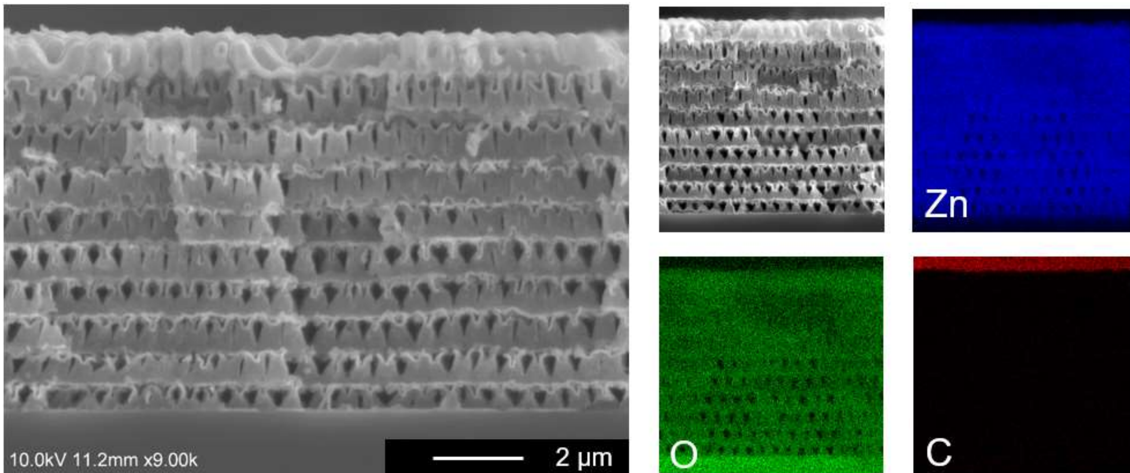

Figure 3.15 Cross-sectional SEM image of ZnO nanostructures (0.23 mol/L).

carbon elements was removed clearly. It demonstrates that the optimized conditions in the current stage are the best conditions to fabricate ZnO 3D periodic inverse nanostructures. The elemental distribution ratio as shown in Fig. 3.16, shows that minute elements (4%) of carbon are still present. It is speculated that the carbon elements found which were covered by the ZnO solution were not completely eliminated after the post-bake process.

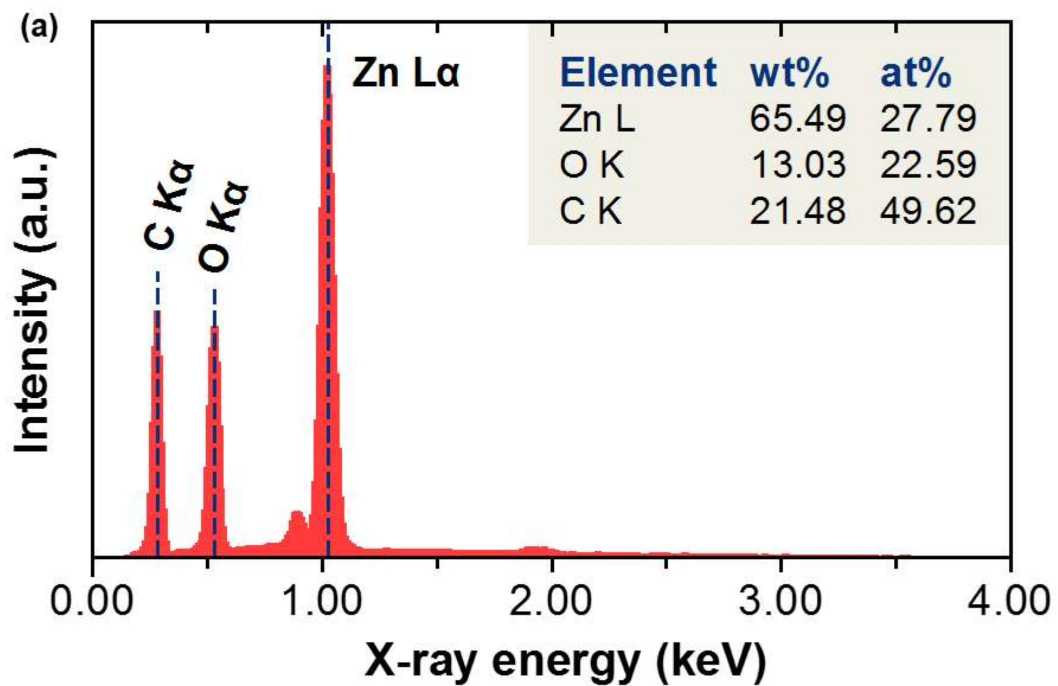

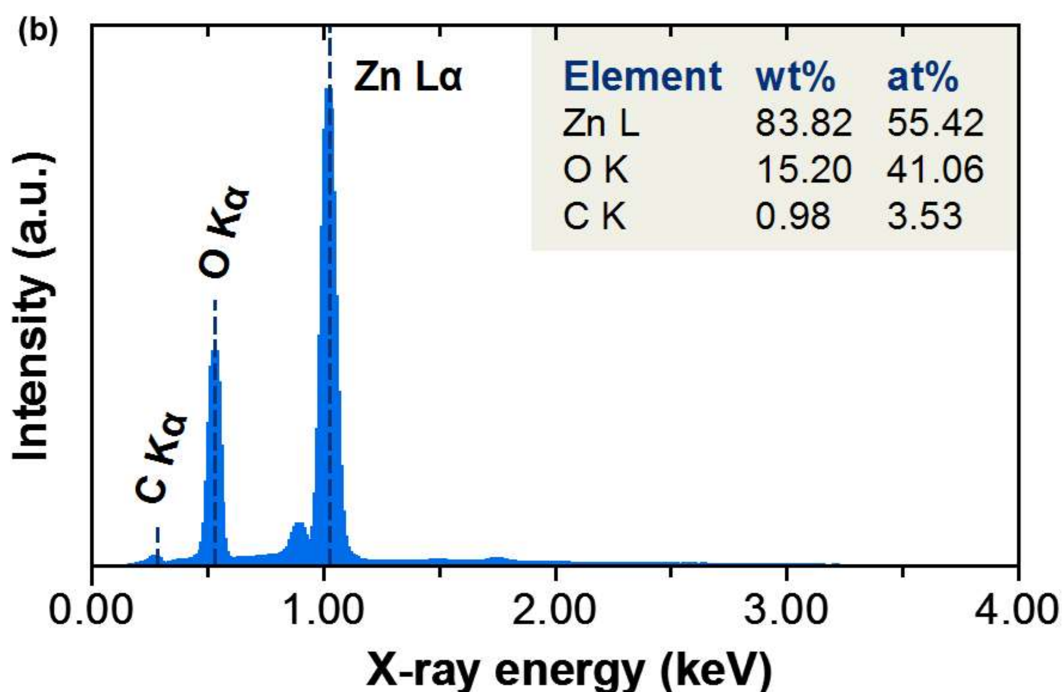

Figure 3.16 Element distribution ratio before (a) and after (b).

The same conditions were used to confirm the reproducibility of the optimized experiment. Unfortunately, there are some bulky residues which partly appeared on the top of the structure with 0.86, 0.47 and 0.30 mol/L ZnO concentration but the important characteristics such as shape of nanostructure and periodicity are similar as previous results (Fig. 3.17). This is because systematic errors occurred during the infiltration process. As a countermeasure, reducing the amount of dispensed liquid is the most appropriate choice when the other conditions are completely consistent. Hence, the reproducibility experiment was performed again after reducing the amount of ZnO solution dispensed from 10 to 9 μL. Figure. 3.18 shows the similar ZnO nanostructures without bulky residues which can be fabricated with 9 μL under different ZnO concentration conditions. These results also show the best uniformity and periodicity. To further affirm the

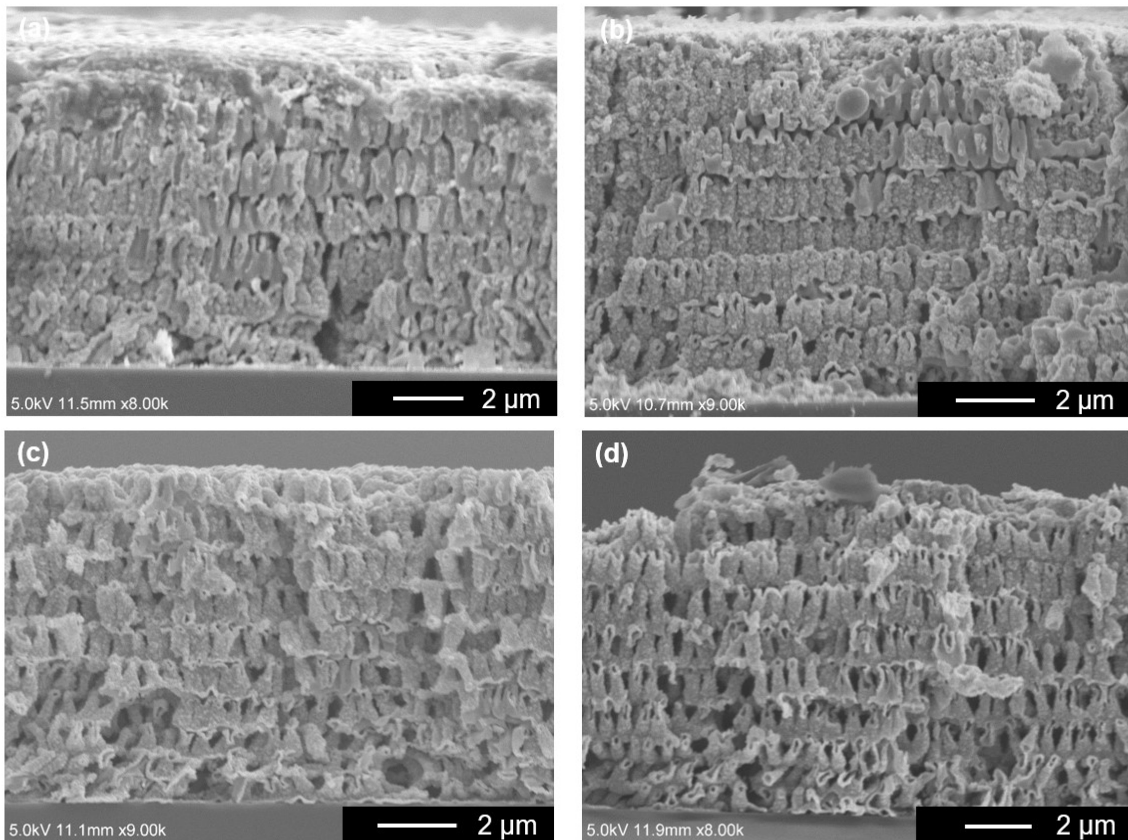

Figure 3.17 Cross-sectional SEM images of ZnO nanostructures, (a): 0.86 mol/L, (b): 0.47 mol/L, (c): 0.30 mol/L, (d): 0.23 mol/L.

reproducibility, the infiltration process is repeated over 10 times, and each time similar results to this experiment can be obtained. Finally, the complete infiltration process was determined as present in the figure below (Fig. 3.19). These conditions are applicable only when the template size is within 1 cm × 0.5 cm. Due to the difference in the size of the different samples and the difference in the thickness of nanostructures, the required filling amount and penetration time are different. Therefore, there are no prescribed conditions applicable to any size. After sample size or thickness is changed, optimization experiments are required.

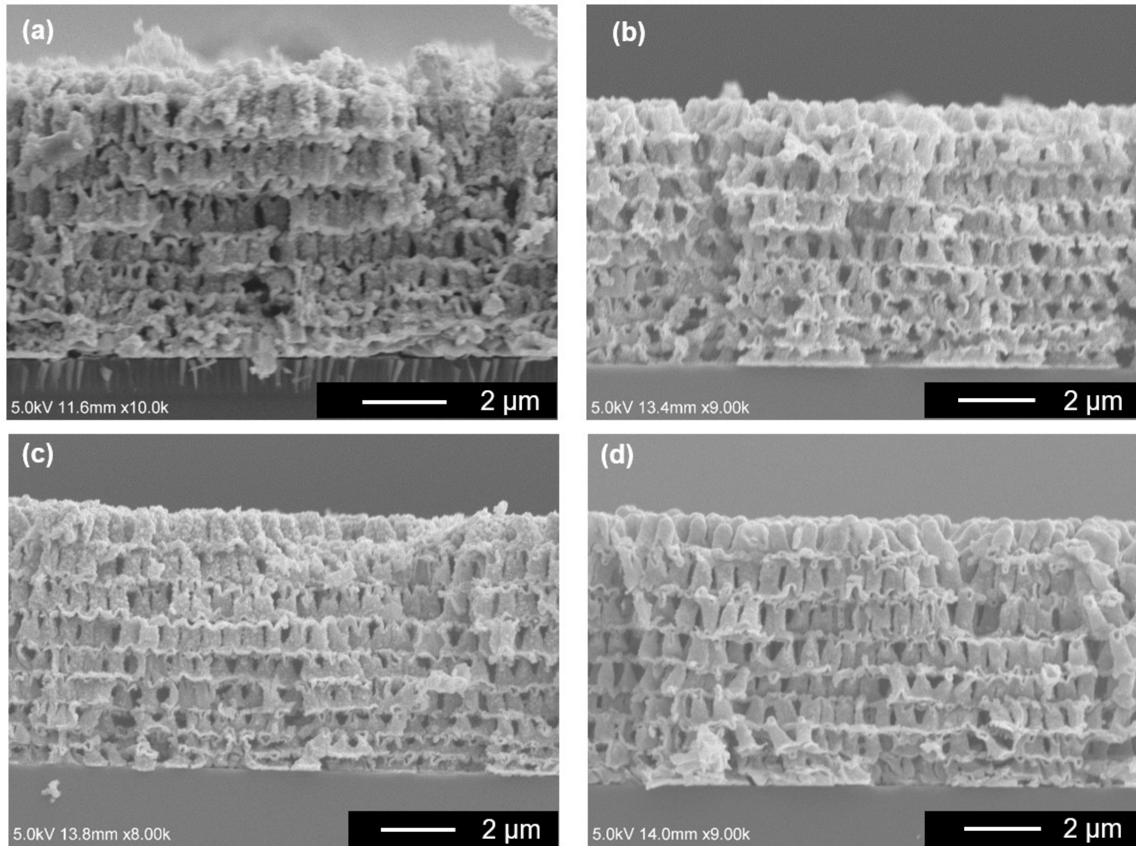

Figure 3.18 Cross-sectional SEM images of ZnO nanostructures with 9 µL,
(a): 0.86 mol/L, (b): 0.47 mol/L, (c): 0.30 mol/L, (d): 0.23 mol/L.

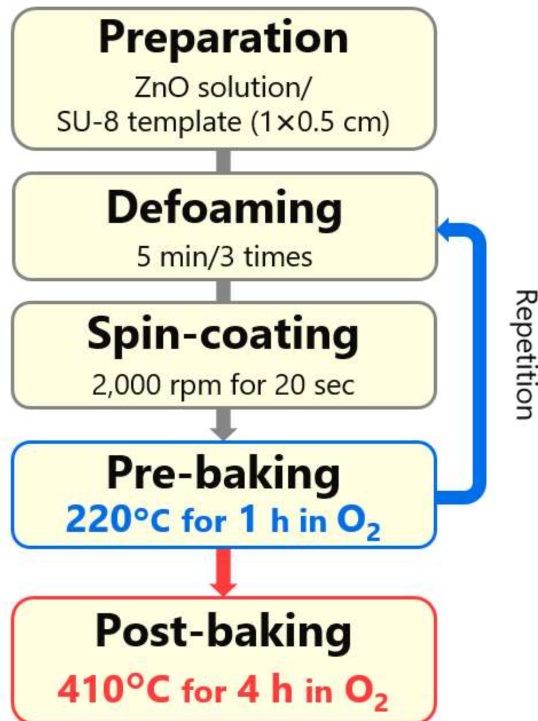

Figure 3.19 Fabrication process of 3D ZnO inverse nanostructure.

3.2.4 Optimization of infiltration process by using KMPR template

In Chap. 2, this work discussed that 3D periodic nanostructure fabricated with KMPR photoresist can be completely removed after curing via a solution process. Here, to compare the changes and differences between ZnO nanostructure formed by the removal of template with KMPR at high temperature annealing and the removal of template with KMPR in the solution process, infiltration experiments were also carried out with the KMPR photoresist. The template with only the KMPR nanostructure was used to affirm the possibility of the solution process first as shown below

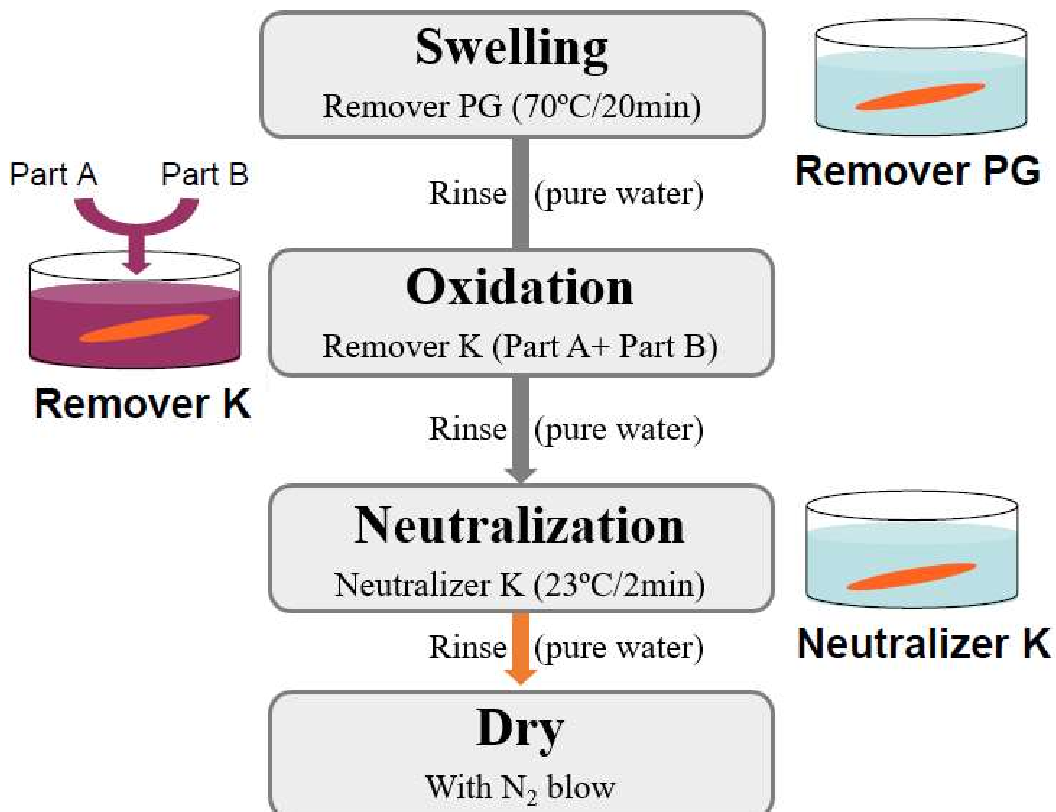

Figure 3.20 Solution remove process of KMPR template [27].

(Fig. 3.20). The general process is divided into four steps which are: swelling, oxidation, neutralization, and drying, respectively. The swelling step was processed at 70 °C for 20 min with a water bath, and Remover PG (MicroChem) was used as the swelling agent. Next, Remover K's part A and part B were mixed with a mass ratio of 1:1 to oxidize the photoresist for another 20 min. For the neutralization step, the neutralizer K was used for 2 min at room temperature. After every step, the templates are cleaned with pure water [27]. As seen in Fig. 3.21, after performing the process mentioned above, the KMPR nanostructure can be completely removed without any residues.

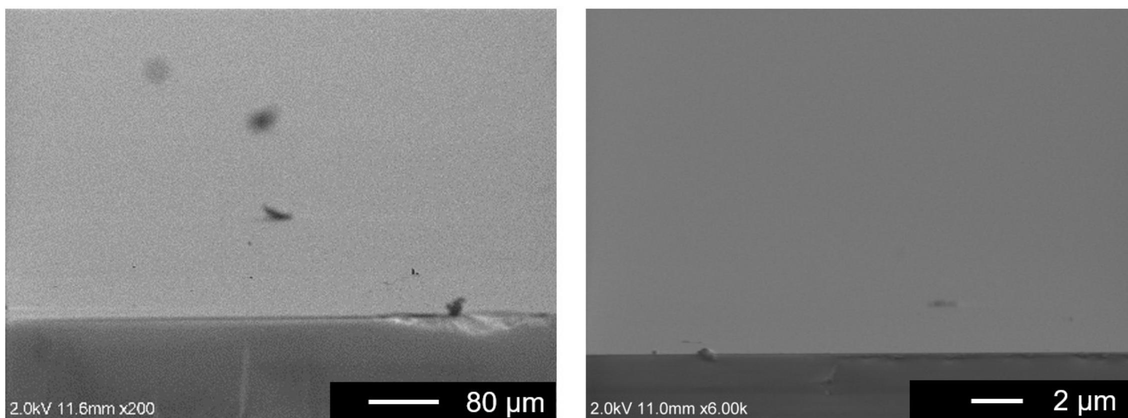

Figure 3.21 Cross-section SEM images after solution remove process for KMPR template.

Afterwards, the same conditions of the infiltration process as described at the beginning of Sec. 3.2.3 were implemented on the KMPR template. The spin-speed of 4000 rpm/sec was also performed as a control group. Figure. 3.22 presents ZnO nanostructures which can be fabricated with the KMPR template under different spin-speeds through the removal of the template at high temperature annealing. A ZnO nanostructure with no residues and with distinct periodicity were successfully fabricated at 4000 rpm/sec. This is

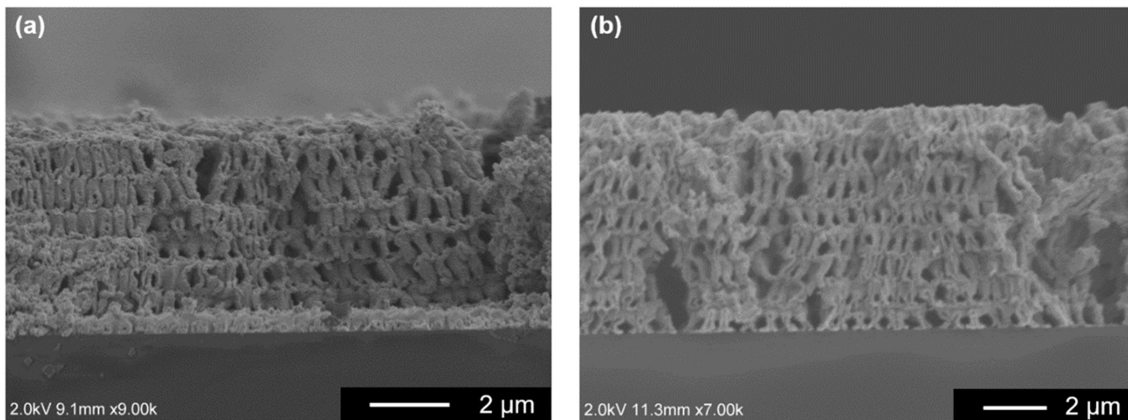

Figure 3.22 SEM images of ZnO inverse nanostructure with different spin-speed, (a): 2000 rpm/sec, (b): 4000 rpm/sec.

because the KMPR nanostructure has a lower shrinkage factor than the SU8 nanostructure, which is already affirmed in Chap. 2. The results show that the nanostructure can be formed without aggregation during the infiltration process. On the contrary, it also caused most of the structure to collapse. On the other hand, when the solution process was used to remove the KMPR template, not only the template was removed but also the ZnO nanostructure was peeled off from the glass substrate due to excessive swelling and strong oxidation. In the future, some solvents with low swelling and low oxidation can be used to try to make the solution process feasible.

3.3 Characteristics of 3D periodic ZnO nanostructure

3.3.1 Comparison between calculation of shrinkage rate by structural size evaluation and theoretical calculation

As described in Chap. 1, the characteristics will significantly change when the nanostructure size of the periodic structure is changed. Thus, the comparison between the ideal structure size obtained by theoretical

calculation and the actual structure size gained from measurement is very important. Firstly, the Z_T of the nanostructure film was measured and compared. 100 points in one sample were measured to ensure the accuracy and calculation error of the data as aforementioned in last chapter. The average Z_T was obtained after data measurement; SU8: 2.32 µm, ZnO(0.86): 2.29, ZnO(0.47): 1.83, ZnO(0.30): 1.80, ZnO(0.23): 1.71, as shown in Fig. 3.23. For the ZnO solution with 0.86 mol/L concentration, the shrinkage of the nanostructure is roughly same with the SU8 template. The Z_T decreased as the concentration of ZnO reduced to 0.47, 0.30 and 0.23 mol/L; this means that the shrinkage increased. Regarding the height of the nanostructures presented in Fig. 3.23 (a), the same shrinking in Z_T occurred. Those two data mutually prove the veracity of the out-of-plane direction shrinkage of the nanostructure.

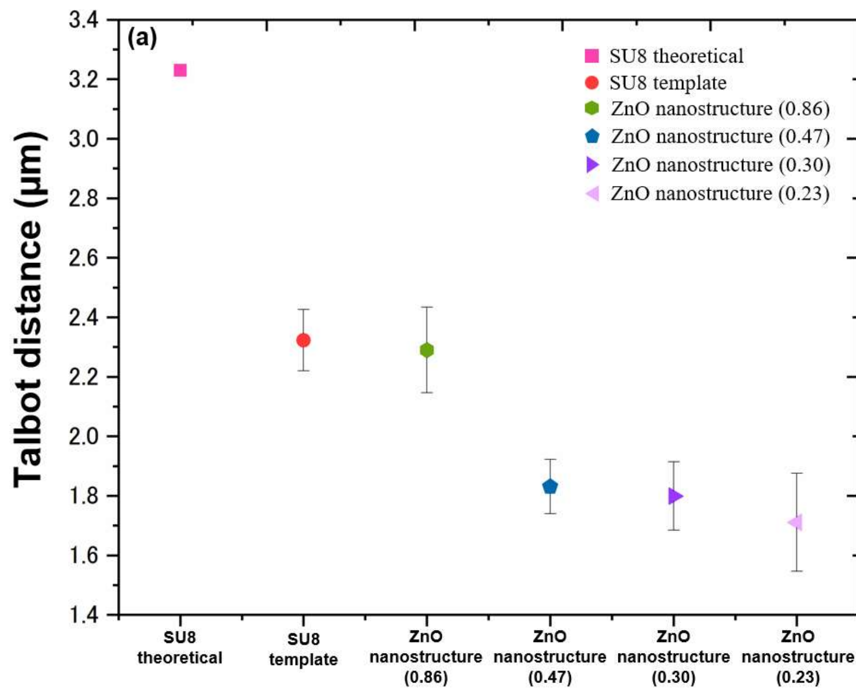

Figure 3.23 Distribution of Talbot distance (a).

The periodicity of the ZnO nanostructures were consistent with the SU8

template and were well within the error range. It indicated that the defoaming step performed first and the amount of dispensed ZnO solution are vital to keep the periodicity constant for the in-plane direction of the nanostructure. Compared with the previous research, the optimized conditions have a lower shrinkage in the in-plane direction, and a similar shrinkage occurred in out-

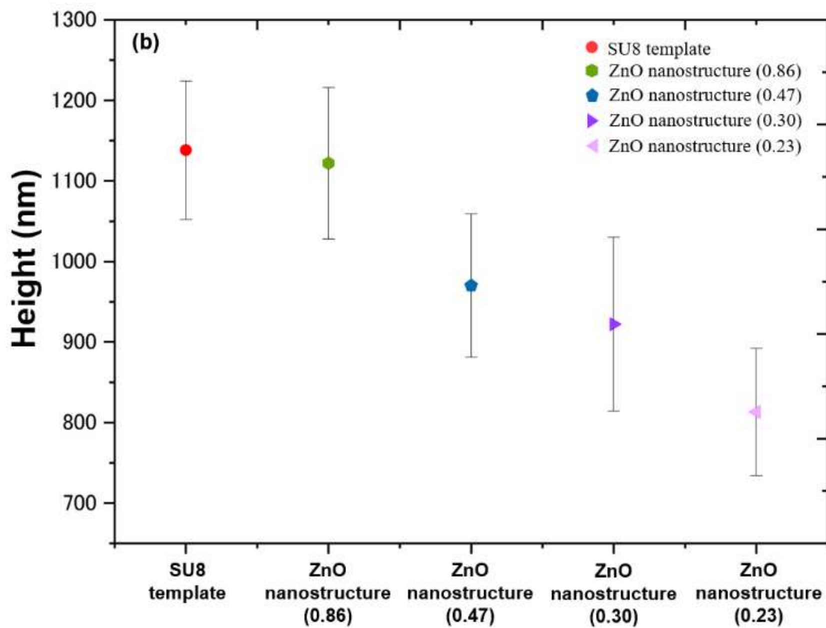

Figure 3.23 Distribution of nanostructure heights (b).

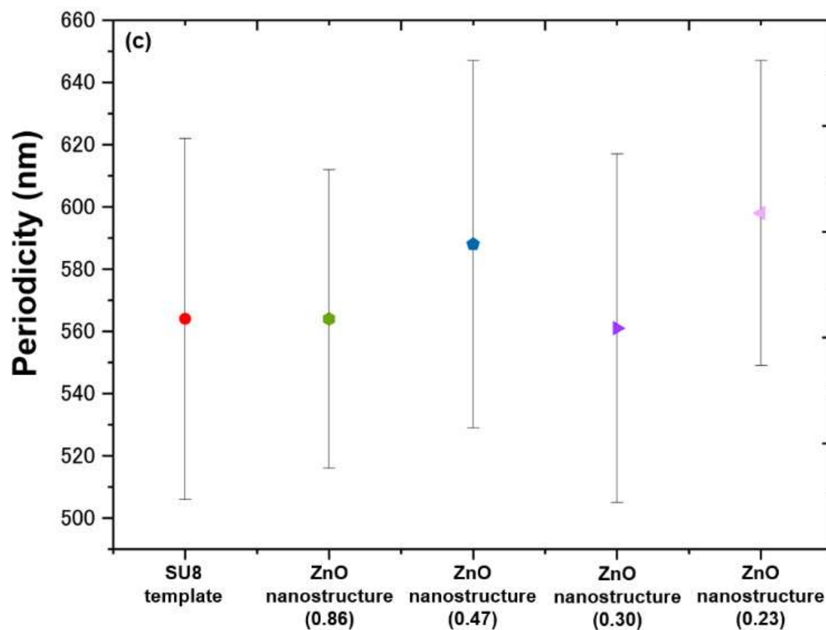

Figure 3.23 Distribution of nanostructure periodicity (c).

plane direction [Fig. 3.23 (b,c)].

It is considered that when a low concentration of ZnO solution is used and the defoaming process is performed first, the partially gelled ZnO which is caused by solvent evaporation, will adheres well around the nanostructures (Fig. 3.24(a)). Thereby, reducing shrinkage and making the distribution more uniform. On the other hand, if a high-concentration ZnO solution is used and spin-coating is performed first, it is highly possible that ZnO will aggregate together with the spin-coat on top of the nanostructure, resulting in surface residues and non-uniform structures (Fig. 3.24(b)).

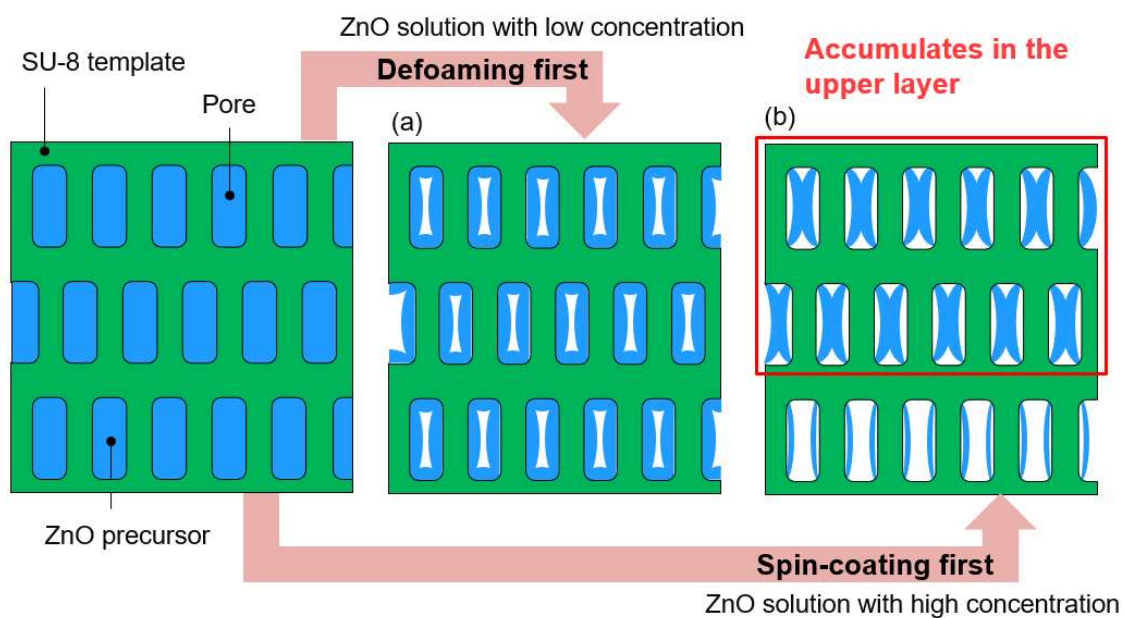

Figure 3.24 Schematic of the structural change mechanism caused by (a) low concentration solution with defoaming first, (b) high concentration solution with spin-coating first.

In Sec. 1.3.1, when the size of nanostructures are smaller than the mean free path (MFP) of phonons, it can effectively scatter phonons thus reducing the lattice thermal conductivity ($\kappa_{lattice}$). From the relationship between the cumulative $\kappa_{lattice}$ of single crystal ZnO and MFP of phonons in the

reference (Fig. 3.25), it can be observed that the MFP of phonons of ZnO are between 5 nm and 15 μm [28]. Therefore, the nanostructure formed here which has the height of the structure approximately 1000 nm in the out-of-plane direction can be expected to block the phonons with MFP greater than 1000 nm. On the other hand, since the nanostructure periodicity in the in-plane direction is around 600 nm, phonons with MFP larger than 600 nm also can be scattered and reduce the $\kappa_{lattice}$. Since the periodicity is smaller than the height, the $\kappa_{lattice}$ in the in-plane direction of the nanostructure should theoretically be lower than the $\kappa_{lattice}$ in the out-of-plane direction.

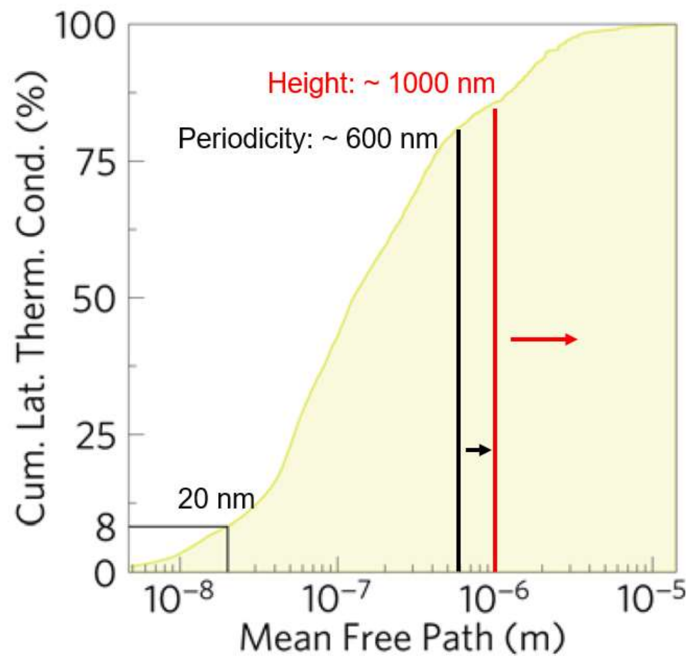

Figure 3.25 Cumulative lattice thermal conductivity against phonon mean free path for single crystal ZnO. [28]

Nevertheless, only about 25% of the $\kappa_{lattice}$ is reduced. In the future, the size of the PSM can be designed to make the nanostructure more smaller, thereby further decrease the $\kappa_{lattice}$.

3.3.2 Crystallographic analysis of ZnO nanostructure by XRD

The change in crystallinity can also affect the thermoelectric properties of the material. Hence, the crystallinity analysis of the ZnO nanostructure is also crucial. The ZnO film without nanostructure fabricated with the same solution served as a reference: a ZnO-MOD solution prepared at a concentration of 1.5 mol/L was applied to a glass substrate that was ultrasonically cleaned with acetone and ethanol, by a spin-coating method at a rotation speed of 2000 rpm for 20 sec, and dried for 5 min. The drying was carried out at 80 ºC on a hotplate and the film thickness after drying was about 50 nm. Then, UV/O_3 treatment was performed at 290 ºC after drying [29]. The purpose of the UV/O_3 treatment are to clean the surface of the film, remove impurities in the film, and accelerate the curing of the film. Since it is necessary to further increase the film thickness in order to evaluate the

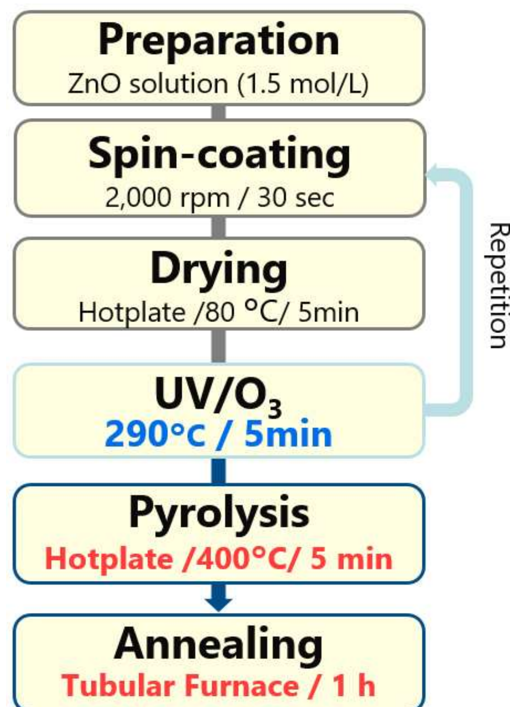

Figure 3.26 The manufacturing flow of ZnO film.

optical and thermal characteristics of the ZnO film, the above steps were repeat 6 times to fabricate a ZnO film with 100 nm thickness. Next, pyrolysis of the solvent was processed at 400ºC for 5 min. Finally, annealing the film in tubular furnace for 1 h at the same temperature for which pyrolysis was performed (Fig. 3.26). The cross-section SEM observation was used to confirm the film thickness and EDX mapping was used to confirm uniformity of the ZnO film, as presented in Fig. 3.27. A ZnO film with 100 nm thickness was successfully fabricated.

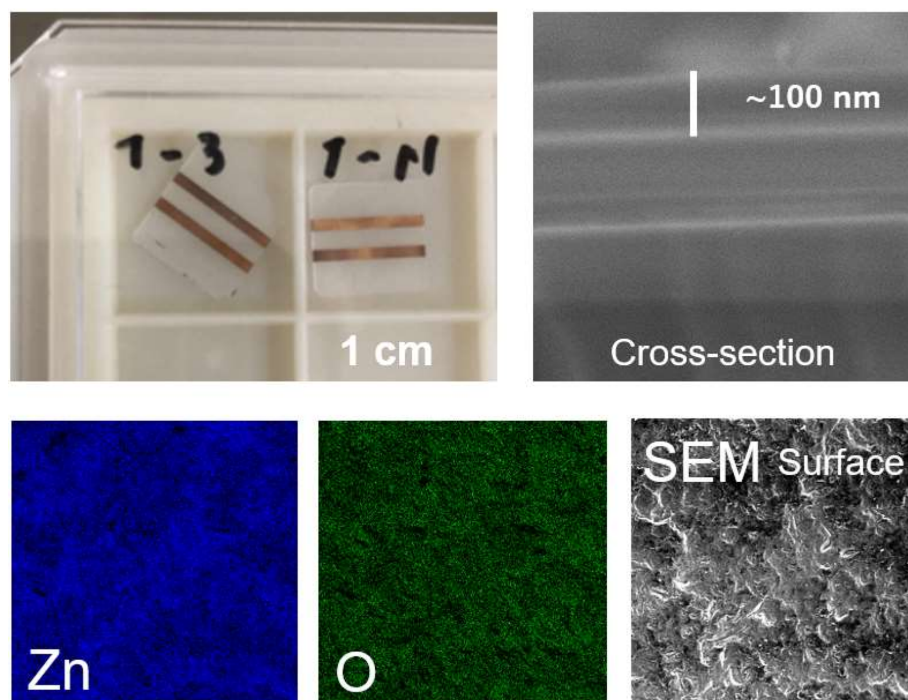

Figure 3.27 SEM observation and EDX analysis of the ZnO film.

The crystallinity of the ZnO film (control sample) and the ZnO nanostructures with different ZnO concentrations were investigated by XRD (RINT TTR3). Figure. 3.28 demonstrates that the crystallinity of ZnO did not change even under prolonged annealing at high temperature. Compared with the database of ZnO powder (57478, ICSD), the same peaks in different

crystal planes can be also obtained for both ZnO film and nanostructures.

The grain size of the three main crystallization directions with different ZnO concentrations was also calculated by Debye-Scherrer equation (Eq.

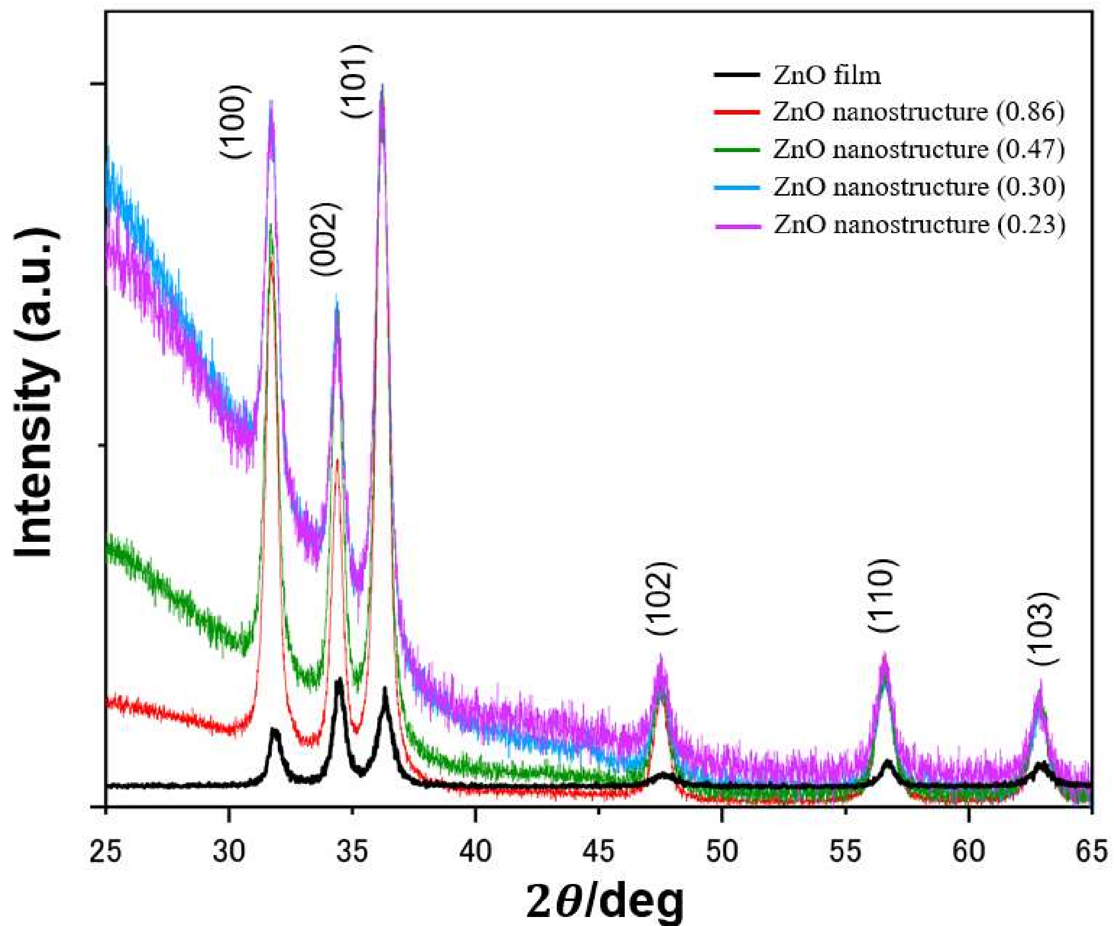

Figure 3.28 XRD spectra of ZnO film and ZnO nanostructures

3.1):

$$\tau = \frac{K\lambda}{\beta cos\theta} \quad (3.1)$$

Where τ is the mean size of the crystalline domains, K is a dimensionless shape factor (0.9), λ is the X-ray wavelength (0.154 nm), β is the line broadening at half the maximum intensity (FWHM), and θ is the Bragg angle. As summarized in Table 3.1, the grain size with different ZnO

concentration and film ranging from 12.6–23.2 nm. Similar with the phonon

Table 3.1 Grain size with ZnO nanostructures and film

Crystal direction	(100)	(002)	(101)
2θ(deg)	31.73	34.42	36.22
Grain size (ZnO nanostructure, 0.86)	15.4 nm	18.4 nm	15.0 nm
Grain size (ZnO nanostructure, 0.47)	14.9 nm	23.2 nm	17.7 nm
Grain size (ZnO nanostructure, 0.30)	14.5 nm	-	15.0 nm
Grain size (ZnO nanostructure, 0.23)	12.6 nm	17.2 nm	16.7 nm
Grain size (ZnO film)	19.7 nm	15.8 nm	14.5 nm

boundary scattering caused by porous nanostructures, phonons will also be scattered at the crystal grain boundary. Because the grain size is usually smaller than the nanostructure, it can be used to block the short MFP phonons that cannot be covered by nanostructures. With reference to the ZnO MFP in the previous section, when the grain size reaches to 20 nm, the 92% of $\kappa_{lattice}$ can be reduced due to the phonon-grain boundary scattering [28]. Therefore, there is a great possibility to further reduce thermal conductivity through improve the phonon-grain boundary scattering. Finally, because the minimum grain size (~12.6 nm) is larger than the MFP of the electron of ZnO (~ 10 nm) [30, 31], it can be considered that grain formed here will not greatly reduce the electrical conductivity.

3.4 Summary

As a summary of this chapter, the infiltration processes used to fabricate an inverse 3D periodic ZnO nanostructures with MOD solution were presented. At the same time, the results confirmed the reproducibility of the previous research, optimized the infiltration process, and successfully fabricated the inverse 3D periodic ZnO nanostructures with different

concentrations of ZnO. The observations below may be helpful for future work:

(a) The inverse 3D periodic ZnO nanostructure could be successfully fabricated with a size limitation of 1 × 0.5 cm, through the defoaming step in the infiltration process. This was carried out in advance after dropping amount of ZnO is controlled to 9 μL. It is also helpful to minimize significant change in shrinkage in the in-plane direction.

(b) EDX analysis shows that after post-baking for 4 h at 410ºC, the original template can be basically removed by high temperature gasification.

(c) Both SU8 and KMPR templates can be used to fabricate the inverse 3D periodic ZnO nanostructure, even with different ZnO concentrations.

(d) Due to gravity, vaporization and shrinkage during the baking of the ZnO solution and original template, the out-of-plane shrinkage further shrinks compared to the template. The shrinkage increases as the concentration of ZnO decreases.

(e) After high temperature treatment, the crystallinity did not change significantly, therefore this method can also be applicable for other solution-derived semiconductor materials that require high-temperature annealing.

References

[1] K. P. Ong, D. J. Singh, and P. Wu, Phys. Rev. B., 83, 115110 (2011).

[2] P. V. Gaikwad, Mater. Res. Express., 6, 056106 (2019).

[3] U. Ozgur, Y. I. Alivov, C. Liu, A. Teke, M. A. Reshchikov, S. Dogan, V. Avrutin, S. –J. Cho, and H. Morkoc, J. Appl. Phys., 98, 041301 (2005).

[4] F. M. Li, G. –W. Hsien, S. Dalal, M. C. Newtow, J. E. Stott, P. Hiralal, A. Nathan, P. A. Warburton, H. E. Unalan, P. Beecher, A. J. Flewitt, I. Robinson, G. Amaratunga, and W. I. Milne, IEEE transactions on electron devices., 55, 11, 3001 (2008).

[5] D. C. Look, Materials Science and Engineering., B80, 383 (2001).

[6] J. Huang, D. Jiang, J. Zhou, J. Ye, Y. Sun, X. Li, Y. Geng, J. Wang, Y. Du, and Z. Qian, Sensors & Actuators: B. Chemical., 327, 128911 (2021).

[7] D. Choi, Materials., 13, 3916 (2020).

[8] A. K. Singh, N. K. Chourasia, B. N. Pal, A. Pandey, and P. Chakrabarti, IEEE photonics technology letters., 32, 24, 1548 (2020).

[9] T. Tsubota, M. Ohtaki, K. Eguchi, and H. Arai, J. Mater. Chem., 7(1), 85 (1997).

[10] L. Brockway, V. Vasiraju, M. K. Sunkara, and S. Vaddiraju, ACS Appl. Mater. Interfaces., 6, 14923 (2014).

[11] P. Jood, R. J. Mehta, Y. Zhang, G. Peleckis, X. Wang, R. W. Siegel, T. B. Tasciuc, S. X. Dou, G. Ramanath, Nano Lett., 11, 4337 (2011).

[12] Y. Jun, P. Nagpal, and D. J. Norris, Adv. Mater., 20, 606 (2008).

[13] D. Shir, E. C. Nelson, Y. C. Chen, A. Brzezinski, H. Liao, P. V. Braun, P. Wiltzius, K. H. A. Bogart, and J. A. Roger, Appl. Phys. Lett., 94, 011101

(2009).
[14] D. Shir , E. C. Nelson, D. Chanda, A. Brzezinski, P. V. Braun, and J. A. Rogers, J. Vac. Sci. Technol. B., 28, 783 (2010).
[15] E. Guilmeau, P. D. –Chao, O. I. Lebedev, A. Recnik, M. C. Schafer, F. Delorme, F. Giovannealli, M. Kosir, and S. Bernik, Inorg. Chem., 56, 480 (2017).
[16] Y. R. Koh, H. Lu, A. C. Gossard, and A. Shakouri, Nanotechnology., 32, 035702 (2021).
[17] R. Yamamoto, D. Kowalski, R. Zhu, K. Wada, Y. Sato, S. Kitano, C. Zhu, Y. Aoki, and H. Habazaki, Applied Surface Science., 537, 147854 (2021).
[18] J. Oh, H. Yoo, J. Choi, J. Y. Kim, D. S. Lee, M. J. Kim, J. –C. Lee, W. N. Kim, J. C. Grossman, J. H. Park, S. –S. Lee, H. Kim, and J. G. Son, Nano. Energy., 35, 26 (2017).
[19] A. F. –Zalewska, Z. Litwicki, K. Moszak, W. Olszewski, K. Opolczynska, D. Pucicki, J. Serafinczuk, D. Hommel, and A. Jezowski, Nanotechnology., 32, 075707 (2021).
[20] K. Kim, J. Park, S. Hong, S. H. Park, S. G. Jeon, C. Ahn, J. Y. Song, and S. Jeon, Nanoscale., 10, 3046 (2018).
[21] K. –M. Huang, C. –L. Ho, H. –J. Chang, and M. –C. Wu, Nanoscale Research Letters, 8, 306 (2013).
[22] M. Miyake, Y. –C. Chen, P. V. Braun, and P. Wiltzius, Adv. Mater., 21, 3012 (2009).
[23] S. –G. Park, T. Y. Jeon, and S. –M. Yang, Langmuir., 29, 31, 9620

(2013).

[24] Y. Xu, X. Zhu, Y. Dan, J. H. Moon, V. W. Chen, A. T. Johnson, J. W. Perry, and S. Yang, Chem. Mater., 20, 1816 (2008).

[25] A. Shinji, Y. Ishikawa, X. D. F. Wang, M. Uenuma, D. Cho, S. Jeon, and Y. Uraoka, Nanoscale Research Letters., 12, 419 (2017).

[26] Kojundo Chemical Laboratory Co., LTD. Http://www.kojundo.co.jp/

[27] X. D. F. Wang, Y. Ishikawa, S. Araki, M. Uenuma, and Y. Uraoka, Jpn. J. Appl. Phys., 58, SDDF08 (2019).

[28] K. B. Spooner, A. M. Ganose, and D. O. Scanlon, J. Mater. Chem. A., 8, 11948 (2020).

[29] Min Zhang, Nara Institute of Science and Technology Master’s Thesis (2012).

[30] S. LeBlanc, S. Phadke, T. Kodoma, A. Salleo, and K. E. Goodson, Appl. Phys. Lett., 100, 163105 (2012).

[31] J. Steinhauser, S. Fay, N. Oliveira, E. Vallat-Sauvain, and C. Ballif, Appl. Phys. Lett., 90, 142017 (2007).

Chapter.4 Fabrication of 3D periodic a-Si:H nanostructure via infiltration process

4.1 Introduction

Amorphous silicon (a-Si) is an amorphous semiconductor mainly composed of silicon. In contrast to the crystalline silicon, it has a large energy gap and high extinction coefficient, which is also can form a film easily. The a-Si solar cells generally feature low efficiency, but due to the absence of toxic heavy metals it is comparatively one of the most environmentally friendly photovoltaic technologies. Nowadays, it is mainly applied to thin-film transistors and solar cells [1–3]. Nevertheless, unhydrogenated a-Si possesses unattractive semiconductor properties because of high defect densities. Although the electronic performance of a-Si is lower than that of polycrystalline silicon, it still has many advantages, such as flexibility and very low temperature deposition. Thus, a-Si is an ideal candidate for roll-to-roll processing techniques [4]. To improve the semiconductor properties for certain use-case scenarios, hydrogen was introduced during the fabrication of a-Si. This type of silicon (appropriately called hydrogenated amorphous silicon (a-Si:H)) was first fabricated by Chittick, Alexander and Sterling by deposition through a silane gas (SiH_4) precursor in 1969. Their results showed increased conductivity with a lower defect density which was confirmed due to impurities [5]. In 1981, Pauls' group found hydrogen concentrations of about 10 atomic % by using IR spectroscopy, thus playing an important role in reducing defects [6].

The most attractive feature of a-Si thin films is their potential application to thermoelectric materials. This can be attributed to relatively low thermal conductivities ranging from 1.2 to 1.8 $Wm^{-1}K^{-1}$ at room temperature. [7,8] At room temperature, the thermal conductivity of a-Si:H varies from 1.1 to 2.5 $Wm^{-1}K^{-1}$. The reason why a-Si film (or a-Si:H film) has low thermal conductivity is because of the disorder of a-Si, which is strongly attributed to scattering the dominant high-energy vibrations. The scattering of phonons at the boundary with the substrate also plays a crucial role [8−11]. By using of the 3D nanostructures, phonon boundary scattering could be further improved leading to ultralow thermal conductivities for a-Si (or a-Si:H).

In this study, with the aim of reducing processing costs, solution-derived silicon was used. Polydihydrosilane was synthesized by a photo-induced ring-opening polymerization process of cyclopentasilane (Si_5H_{10}; CPS) [12−16]. In the case of a 3D nanostructure template and solution-derived silicon, the results in the previous chapters suggest that the same infiltration process with solution-derived ZnO can be realized. Therefore, there is a great possibility that a 3D inverse silicon nanostructure with an ultralow thermal conductivity can be fabricated.

4.2 Fabrication of 3D periodic a-Si:H nanostructure via infiltration process

4.2.1 Fabrication of the a-Si:H film by a solution-derived silicon

Firstly, in order to make a a-Si:H film without nanostructures as a reference, liquid-source vapor deposition (LVD) was used. Other works have used this approach to fabricate a-Si:H film with this kind of solution-derived silicon [16–18]. It takes advantage of the vaporization, solidification and conversion of solutions at high temperatures so that the a-Si:H can be deposited on the surface of the substrate uniformly [19]. To verify whether the a-Si:H films on different substrates could be formed or not and facilitate the further evaluation, the same glass substrate with 3D nanostructure

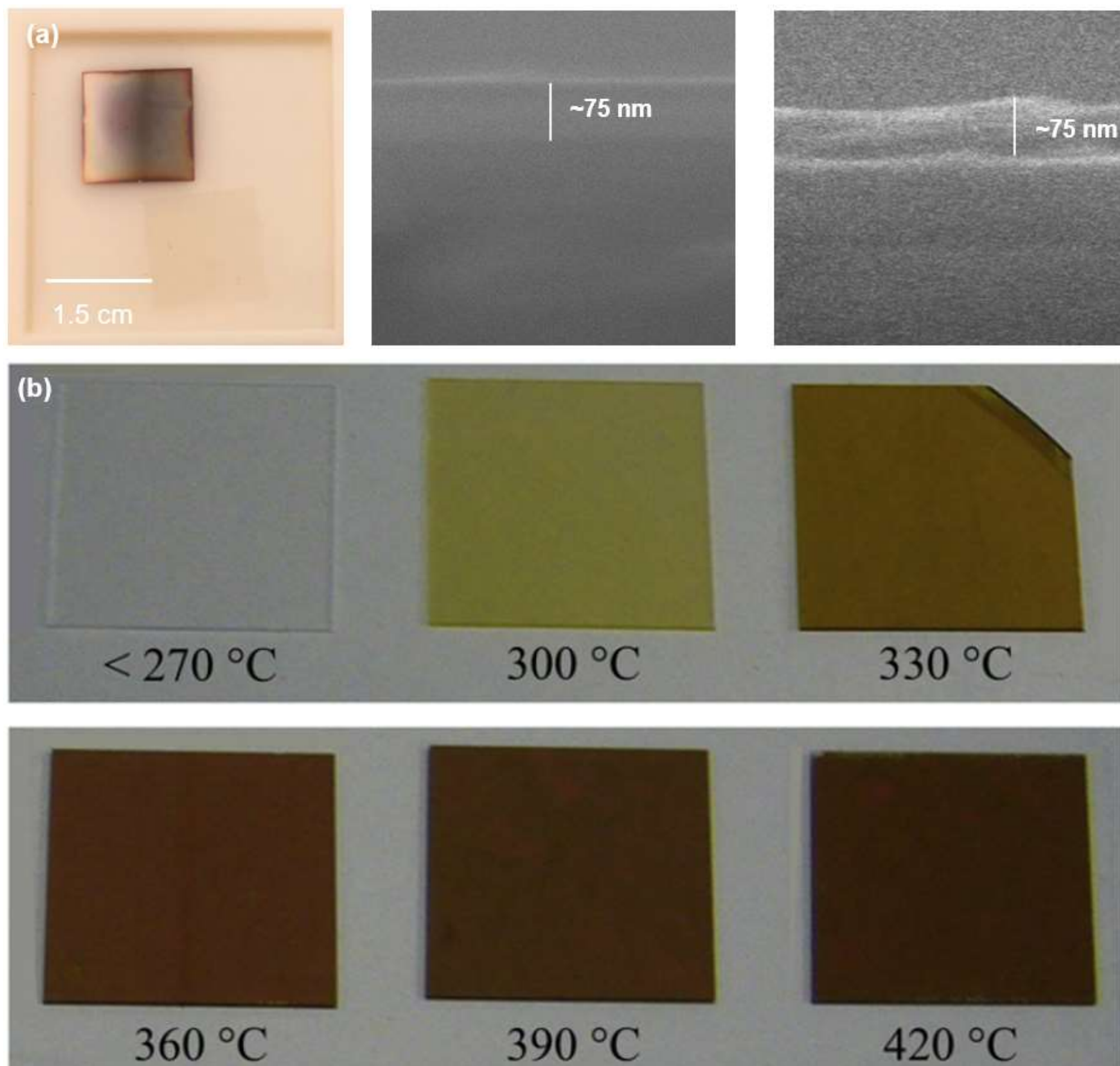

Figure 4.1 The a-Si:H film formed with LVD method.
(a): The a-Si:H film formed with glass substrate, (b): Reference films [12].

template was used. The condition of pyrolysis conversion was set at 540ºC for 30 min. Figure. 4.1 presents the a-Si:H films fabricated with an approximate thickness of 75 nm. The results suggest that the a-Si:H films are not evenly formed when compared with the reference. This is caused by the different substrates and excessive pyrolysis temperature [12]. To confirm the element of the a-Si:H film, energy-dispersive X-ray (EDX) spectral analysis was measured as shown in Fig. 4.2, it can be seen that the carbon element in the film is basically 2%, and the very small amount of carbon observed here can be attributed to the carbon tape, which is needed to prevent the charging up. Therefore, it is inferred that the carbon element from the solution-derived material is assumed to be null.

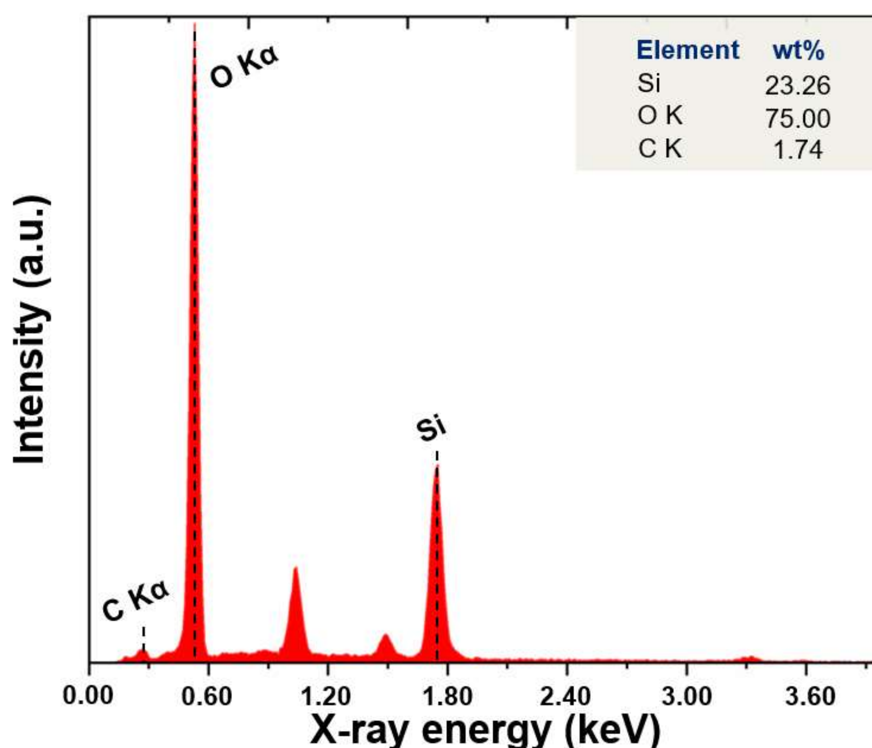

Figure 4.2 Element distribution ratio of a-Si:H film

For the fabrication of a-Si:H 3D nanostructures, LVD was used and the pyrolysis conditions was adjusted at 400ºC for 30 min. However, from the

SEM observation (Fig. 4.3) the nanostructures cannot be observed due to the high pyrolysis temperature which evaporates and removes the original

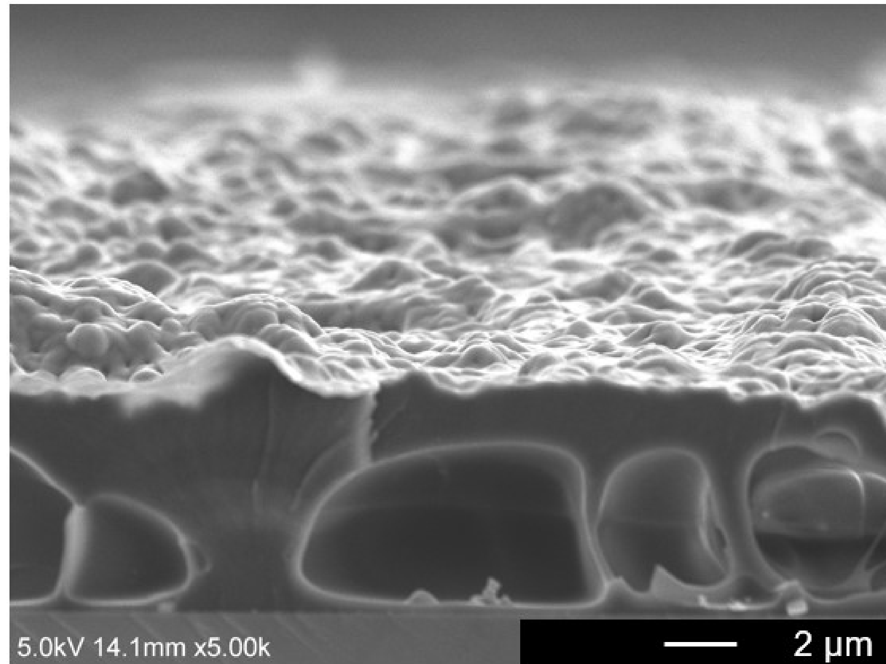

Figure 4.3 Cross-sectional SEM image of the a-Si:H nanostructure formed with LVD method.

nanostructure template before the skeleton of the a-Si:H nanostructure can be formed. Therefore, the LVD method is not applicable for fabrication. After the successful fabrication of ZnO by the infiltration process in Chap. 3, the infiltration process was the most viable candidate which can be applied to solution-derived silicon.

4.2.2 Fabrication procedures of 3D periodic a-Si:H nanostructure

Firstly, dispensing only 1.0 μL of solution without any other treatment was done to confirm whether the infiltration caused by the capillary action was

still effective or not. Afterward, pyrolysis was done on the solution-derived silicon at 400ºC for 15 min. Figure. 4.4 shows that the shape of the

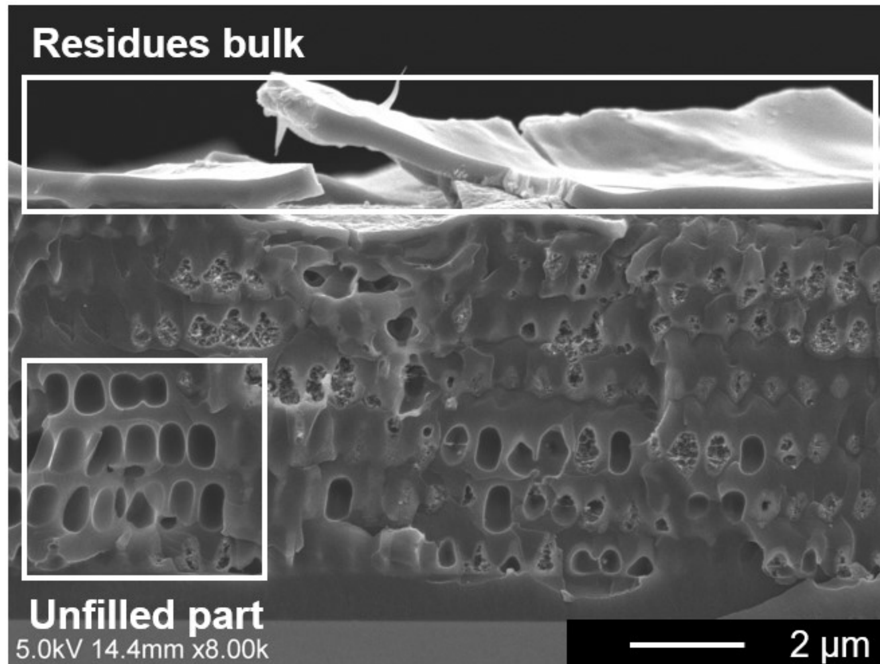

Figure 4.4 Cross-sectional SEM image of the a-Si:H nanostructure formed with infiltration process.

nanostructure can be preserved, and also shows that the infiltration process is still effective with solution-derived silicon. On the other hand, the unfilled areas and bulky residues were observed at the same time, which illustrates the fact that spin-coating and defoaming steps are necessary. From the summary of the Chap. 3, several important conditions of the infiltration process are summarized: amount of filling cycle, spin-coat, defoam and pre-bake temperature which will facilitate the fabrication of the nanostructure skeleton, thus making the nanostructure more complete.

The spin-coat is carried out at high spin-speed and low spin-speed. For the defoaming step, it was set for 7 min in a vacuum chamber so that the solution-derived silicon can penetrate the nanostructure template as deep as

possible.

The prebaking step was set at 120ºC for 1 min to facilitate the formation of the skeleton of the a-Si:H nanostructure without destroying the original template structure. The reason why is that the silicon hydride compounds inside the solution-derived silicon starts cross-linking from 120ºC, then solidify the solution-derived silicon [19]. The TG-DTA data (Fig. 4.5) from the reference shows that the pyrolyzation temperature is around 300ºC and the polymer will be transformed to a-Si:H. When it exceeds 360ºC, the a-Si:H becomes more stable [15,17]. After the prebaking step, a post-baking step was done at 400ºC for 15 min to induce pyrolytic transformation, thus transforming the solution-derived silicon to a-Si:H.

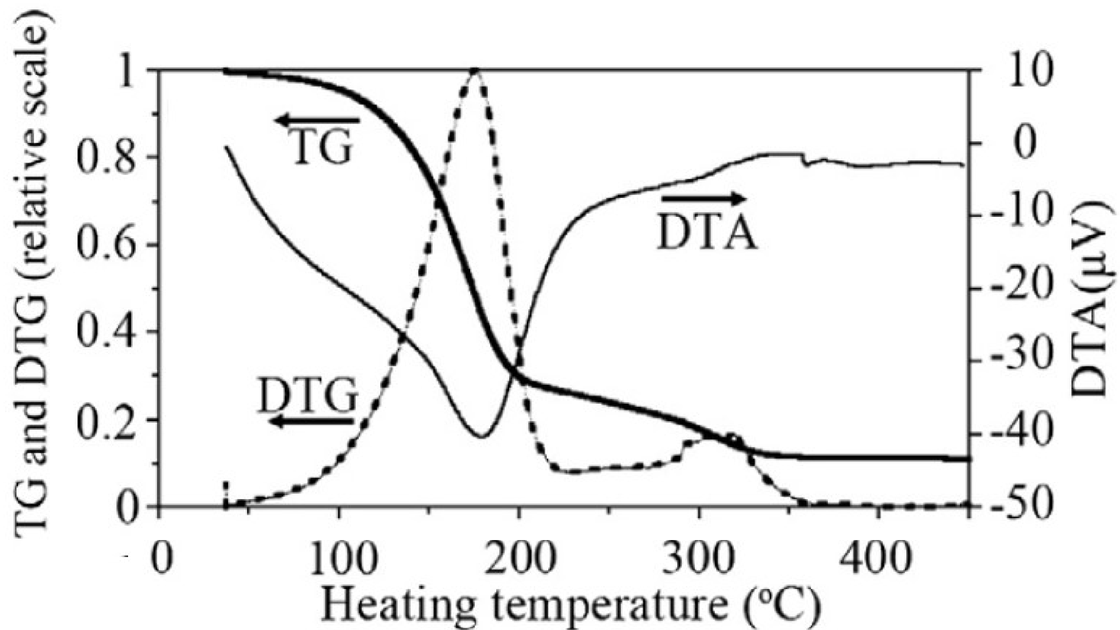

Figure 4.5 TG (blue line), DTA (black line), and DTG (red line) curves of the solution-derived silicon [15,17].

In addition, by adjusting the filling cycles, the film thickness of the nanostructure can be kept as same as that of the template and the shrinkage of the structure can also be reduced as described in the previous research [20].

Therefore, the filling cycles in this process was also be controlled from 3 to 1 cycles. Finally, to remove the original template, samples were annealed at 400ºC for 4 h in a furnace, which was also applied in Chap. 3. The fabrication flow is shown in Fig. 4.6.

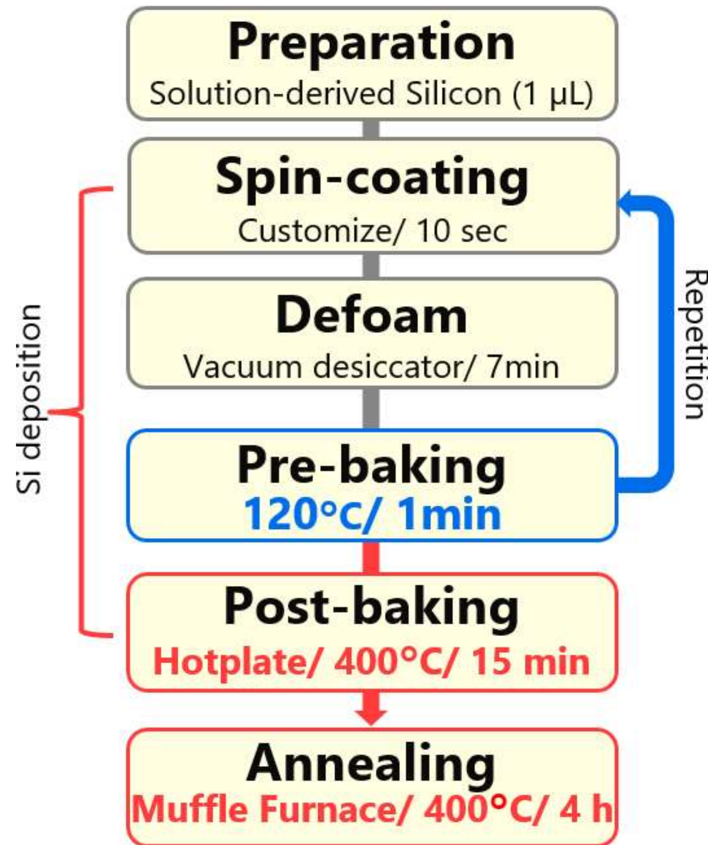

Figure 4.6 Fabrication flow of the a-Si:H nanostructure.

4.2.3 Fabrication of 3D periodic a-Si:H nanostructure with KMPR template

3 filling cycles at high spin speed was first used to fabricate the a-Si:H nanostructure with a KMPR template as represented in Fig. 4.7. The SEM observation before annealing was obtained to confirm the permeability of the

solution-derived silicon. There is a part of the nanostructure that cannot be filled in before the annealing as shown in Fig. 4.7(a). After the annealing, the shape of the nanostructure in Fig. 4.7(b) shows a big difference with the ZnO nanostructure formed in Chap. 3. Since the solution-derived silicon used is

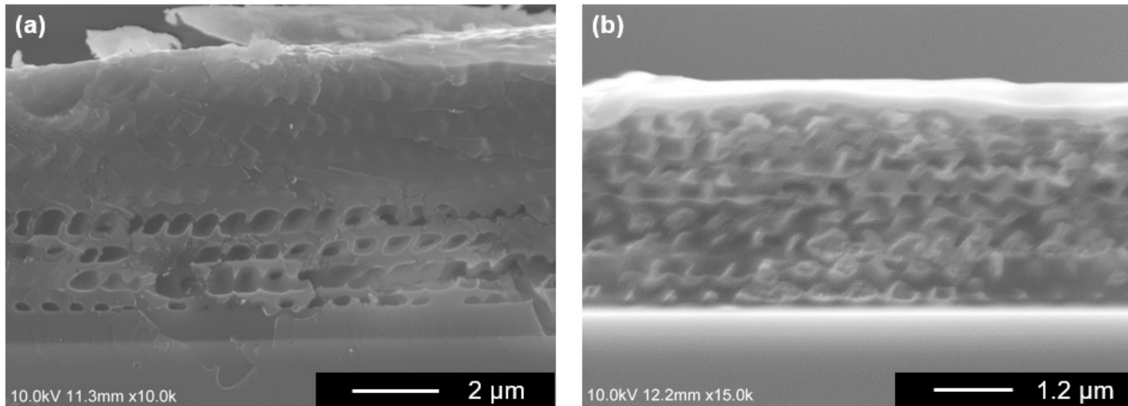

Figure 4.7 Cross-sectional SEM images of the a-Si:H nanostructures, (a): Before annealing, (b): After annealing (3 filling cycles, high spin speed, defoam/7min).

not a polymer, excessive weight will cause greater shrinkage and deformation of the nanostructure. Both these observations show that the a-Si:H residues still exist, but the thickness of the residue is significantly reduced compared to one in Fig. 4.4.

Then, the number of filling cycles was decreased to 2 to further remove the a-Si:H residue and optimize the process. The defoaming time was increased to 10 min at the same time. In Fig. 4.8, the template thickness and nanostructure changed a lot which is attributed to the different KMPR templates being used. By increasing the defoaming time, the residues became thinner as compared to previous samples. The low spin speed was used to fabricate the reference samples. This is because even if the samples fabricated at a high spin speed had no surface residues, the nanostructure becomes warped and distorted (Fig. 4.9).

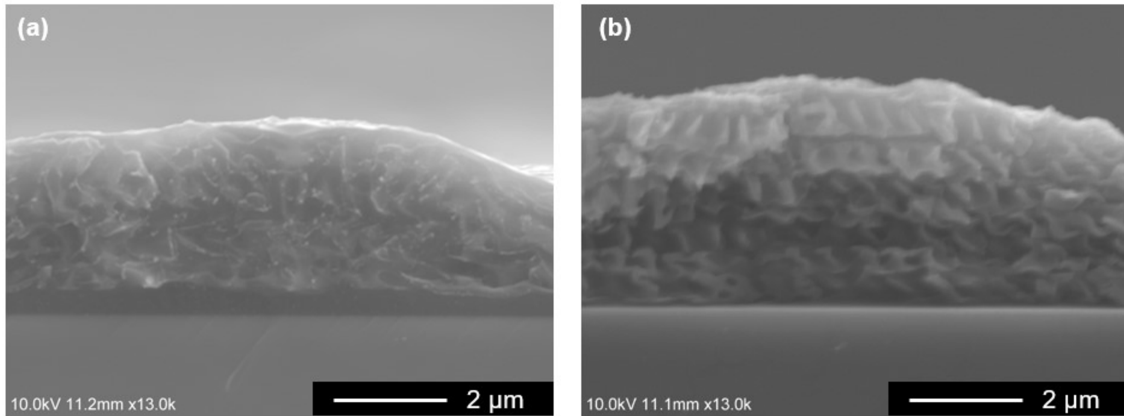

Figure 4.8 Cross-sectional SEM images of the a-Si:H nanostructures, (a): Before annealing, (b): After annealing (2 filling cycles, high spin speed, defoam/10min).

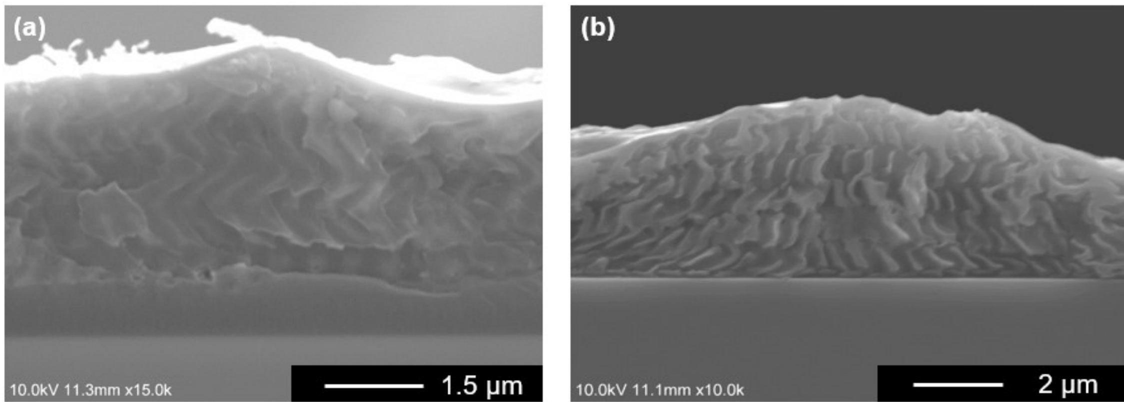

Figure 4.9 Cross-sectional SEM images of the a-Si:H nanostructures, (a): Before annealing, (b): After annealing (2 filling cycles, low spin speed, defoam/10min).

Next, with 1 filling cycle, as observed in Fig. 4.10(a) and Fig. 4.11(a), the solution-derived silicon can completely penetrate the whole nanostructure template, and the thickness of the nanostructure did not show significant shrinkage. Therefore, the 1 filling cycle was considered to be one of the best conditions at the current stage. After annealing, the same shrinkage of the nanostructure happened, and it was clearly deformed. There are several reasons as to why deformation still occurs with 1 filling cycle. Firstly, the 3D nanostructure cannot support itself when the solution is dispensed. Secondly, the nanostructure of the template is soft which can be deformed

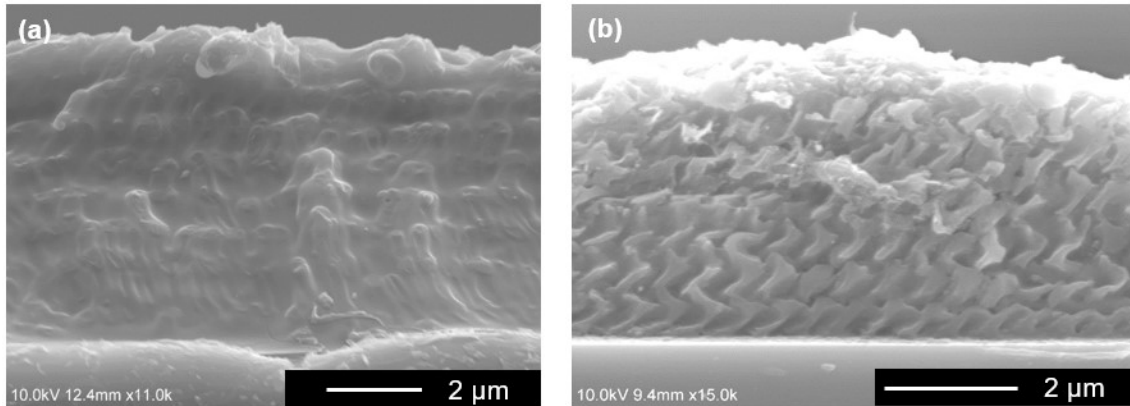

Figure 4.10 Cross-sectional SEM images of the a-Si:H nanostructures, (a): Before annealing, (b): After annealing (1 filling cycle, high spin speed, defoam/10min).

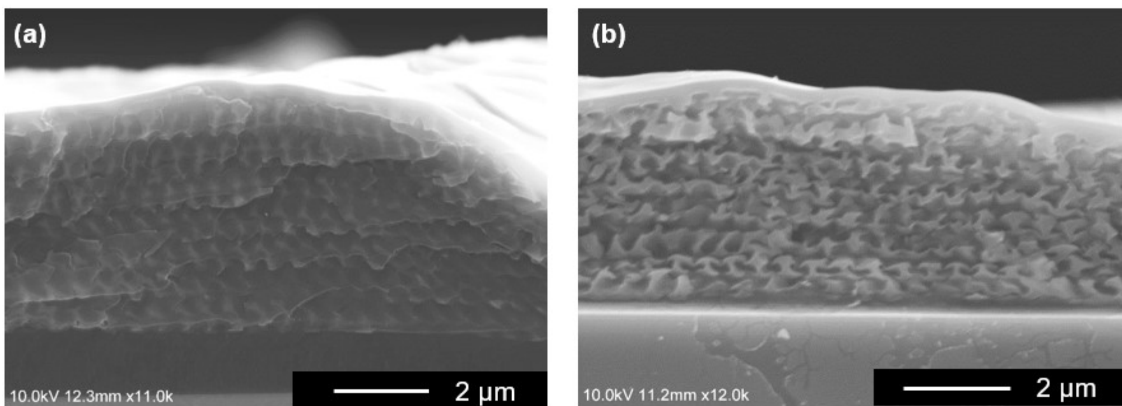

Figure 4.11 Cross-sectional SEM images of the a-Si:H nanostructures, (a): Before annealing, (b): After annealing (1 filling cycle, low spin speed, defoam/10min).

easily. Finally, the stress which occurs inside the nanostructure during the post-baking process was considered as another influential factor that can be observed from the bending of the nanostructure as seen in the SEM observation in Fig. 4.12.

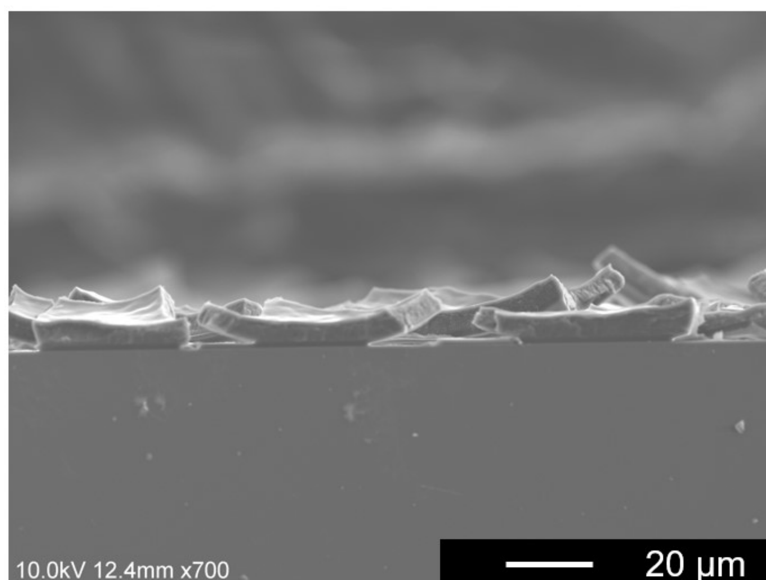

Figure 4.12 Cross-sectional SEM image of the a-Si:H nanostructures (1 filling cycle, low spin speed, defoam/10min).

The best settings used as the defoaming step prior to spin-coating as described in Chap. 3 were also applied to this process. The nanostructure before the annealing shown in Fig. 4.13(a) shows that the deformation happened before the annealing as well. EDX mapping of the silicon elements substantiates that solution-derived silicon can completely infiltrate into the entire nanostructure and EDX mapping of the carbon elements after annealing affirmed that the nanostructure template was basically removed (Fig. 4.13). To further confirm the amount of carbon from the template, elemental analysis was performed at the same time by EDX. Figure. 4.14 expressed that the amount of carbon decreased to 30% from 41% after annealing, which proved that the nanostructure template was partly removed.

To minimize the effect of high temperature on crystallinity, the KMPR nanostructure template removed by solution method was also attempted. Unfortunately, the a-Si:H nanostructure was peeled off from the glass

substrate together with the nanostructure template, which was caused by the similar effect found in Chap. 3.

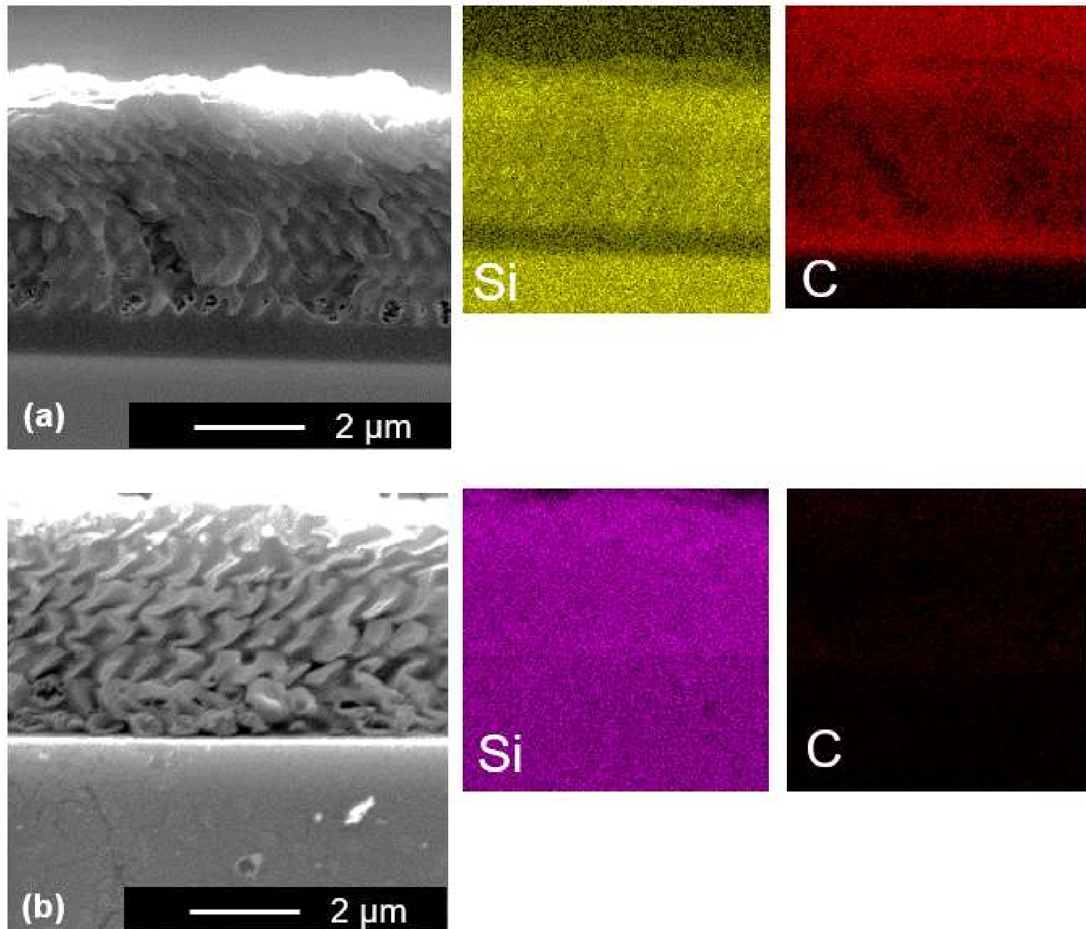

Figure 4.13 Cross-sectional SEM images of the a-Si:H nanostructures formed with infiltration process, (a): Before annealing, (b): After annealing (2 filling cycles, defoam/10min/3times, high spin speed).

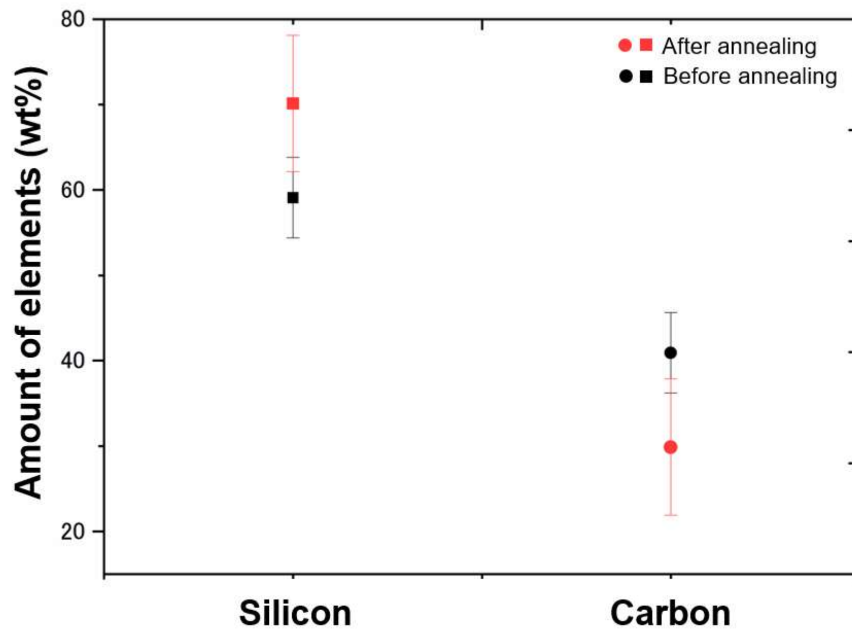

Figure 4.14 Comparison of silicon and carbon amount before and after annealing.

4.2.4 Fabrication of 3D periodic a-Si:H nanostructure with SU8 template

The same experimental procedure was applied to SU8 template as well. As compared to the KMPR template, the solution-derived silicon can entirely penetrate inside the SU8 nanostructure from the top to the bottom with 3 filling cycles before the annealing process as presented in Fig. 4.15(a). However, the deformation and shrinkage happened after the annealing as well (Fig. 4.15(b)). With 2 filling cycles, the solution-derived silicon can perfectly infiltrate the nanostructure, but the a-Si:H nanostructure still had a large shrink and the collapsed structures were much more increased than before (Fig. 4.16, Fig. 4.17).

As for 1 filling cycle, all different conditions were perfectly penetrated by solution-derived silicon, and without surface residues, even for the low spin-

speed sample (Fig. 4.18–4.20). After the annealing step, the same

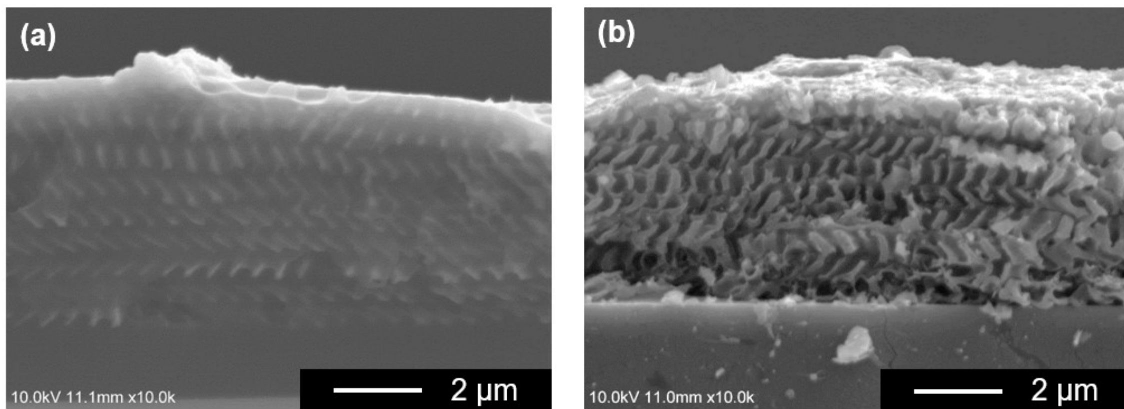

Figure 4.15 Cross-sectional SEM images of the a-Si:H nanostructures, (a): Before annealing, (b): After annealing (3 filling cycles, high spin speed, defoam/7min).

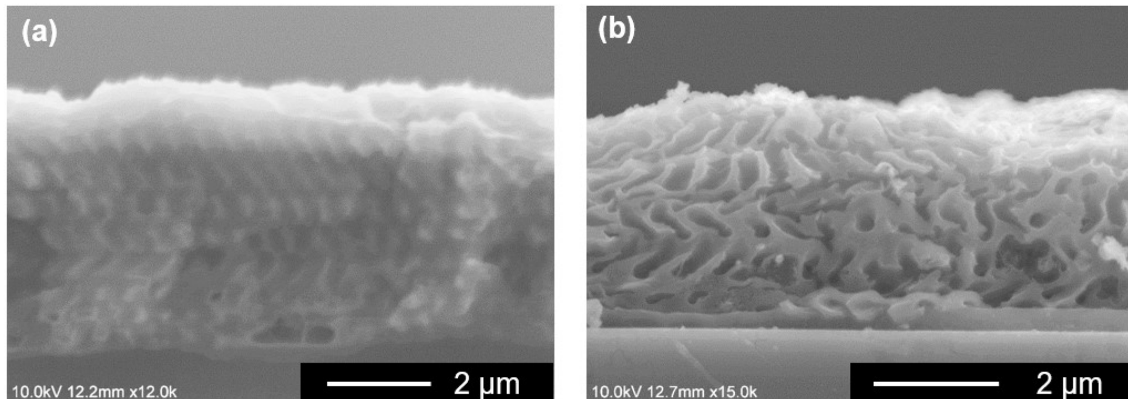

Figure 4.16 Cross-sectional SEM images of the a-Si:H nanostructures, (a): Before annealing, (b): After annealing (2 filling cycles, high spin speed, defoam/5min/3times).

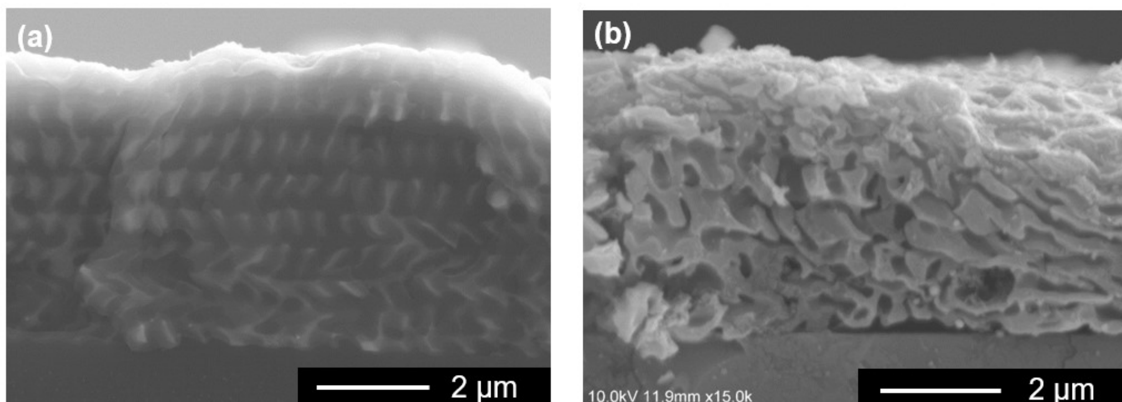

Figure 4.17 Cross-sectional SEM images of the a-Si:H nanostructures, (a): Before annealing, (b): After annealing (2 filling cycles, low spin speed, defoam/5min/3times).

deformation happened only slightly compared to the previous results.

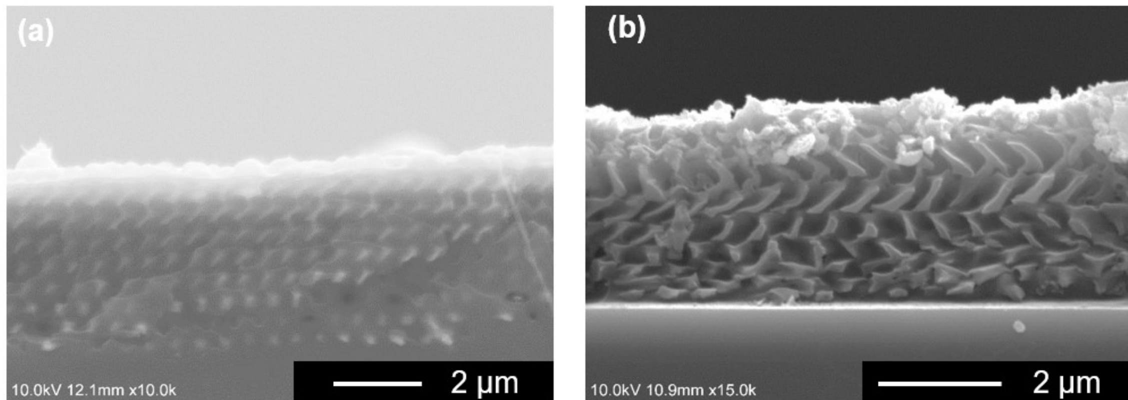

Figure 4.18 Cross-sectional SEM images of the a-Si:H nanostructures, (a): Before annealing, (b): After annealing (1 filling cycle, high spin speed, defoam/5min/3times).

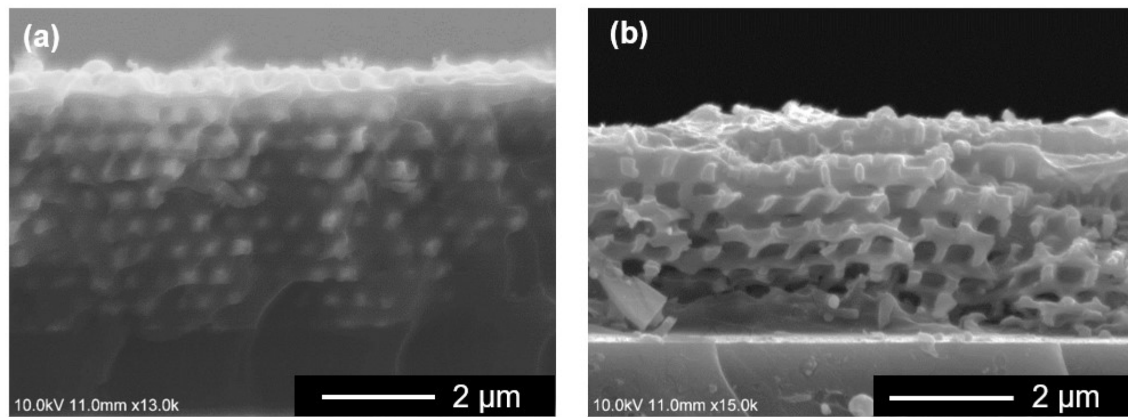

Figure 4.19 Cross-sectional SEM images of the a-Si:H nanostructures, (a): Before annealing, (b): After annealing (1 filling cycle, low spin speed, defoam/5min/3times).

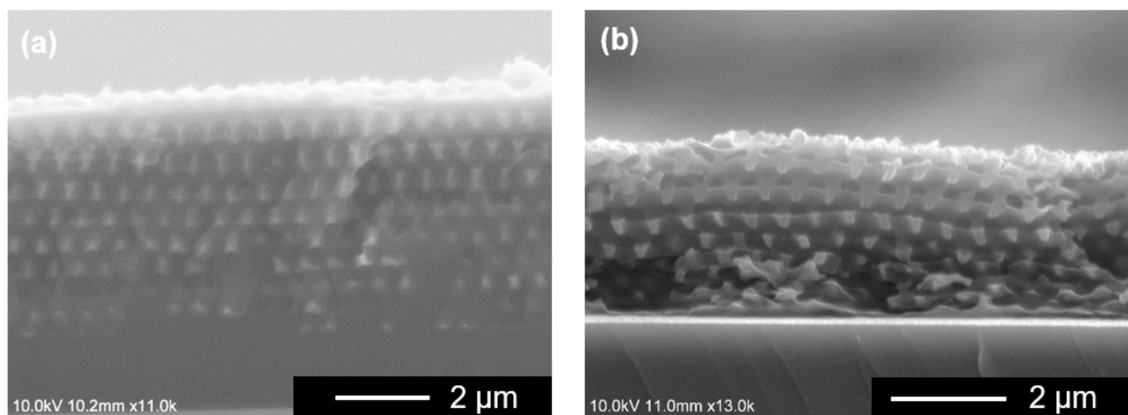

Figure 4.20 Cross-sectional SEM images of the a-Si:H nanostructures, (a): Before annealing, (b): After annealing (1 filling cycles, low spin speed, defoam/10min).

Especially, when the low spin speed was used, the shape of some nanostructures is comparable with the original structure as shown in Fig. 4.19(b) and Fig. 4.20(b). Therefore, it is considered as one of the two best conditions. The other best condition is by using 2 filling cycles with a defoaming step processed previous to the low spin coat step. This can also reduce the shrinkage of the out-of-plane direction. However, the residues still existed. Similarly, the amount of the silicon and carbon measured by EDX mapping in Fig. 4.21 again proved the successful infiltration of the solution-derived silicon and removal of the original nanostructure template. The amount of carbon from the template here is lower than that of KMPR, which is decreased to 26% from 44% after annealing (Fig. 4.22). This section explains that silicon nanostructures made with SU8 template can maintain a

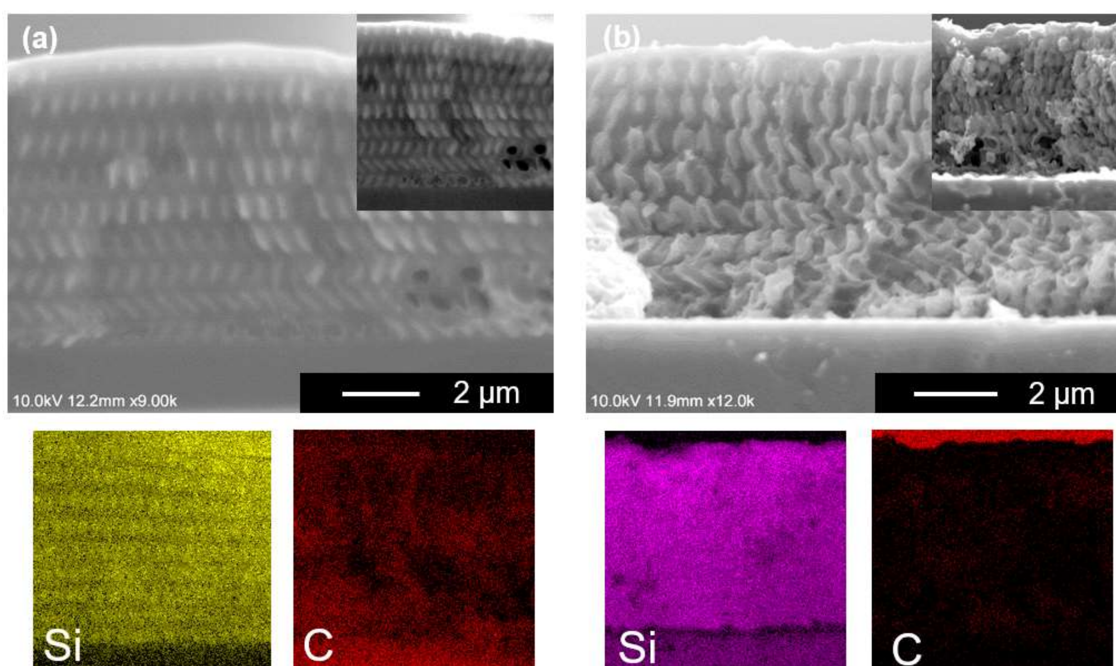

Figure 4.21 Cross-sectional SEM images of the a-Si:H nanostructures, (a): Before annealing, (b): After annealing (2 filling cycles, defoam/5min/3times, low spin speed).

better nanostructure shape. Moreover, after high temperature treatment, the carbon element of SU8 template was less than KMPR, which will facilitate accurate measurement of characteristics.

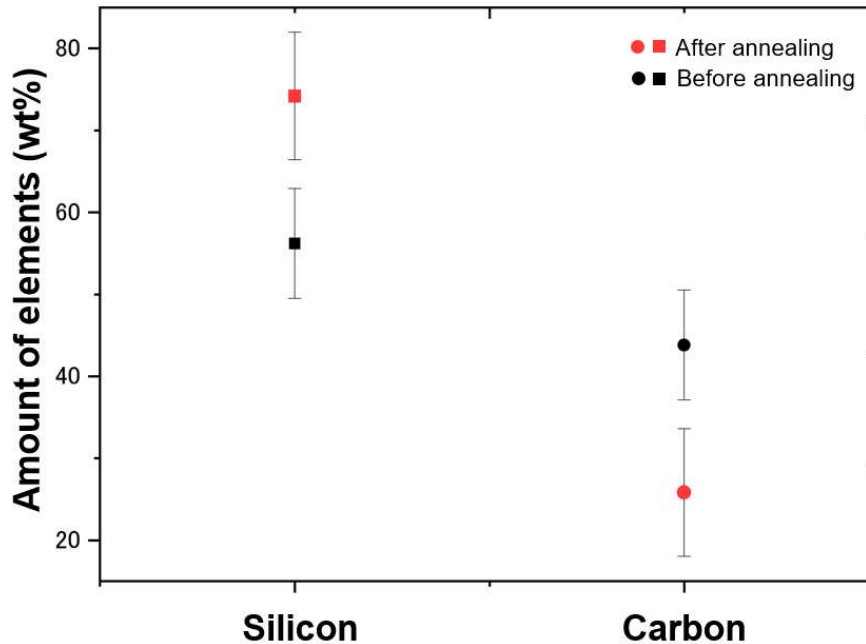

Figure 4.22 Comparison of silicon and carbon amount before and after annealing.

4.2.5 Reproducibility of the a-Si:H 3D nanostructures

The two best conditions in Fig. 4.20 and 4.21 are repeated to verify the reproducibility. Unfortunately, with 1 filling cycle, low spin speed, and 10 min defoam time, the a-Si:H nanostructure cannot be reproduced, which is probably caused by slightly different nanostructure templates used every time. For the 2 filling cycles with the 5 min defoam step processed prior to the low spin speed, similar a-Si:H nanostructures can be obtained as Fig. 4.23, but because of the excessive amount of the solution-derived silicon with 2 cycles, the a-Si:H residues still existed in a large area. It indicates that

further optimization is still required in future work.

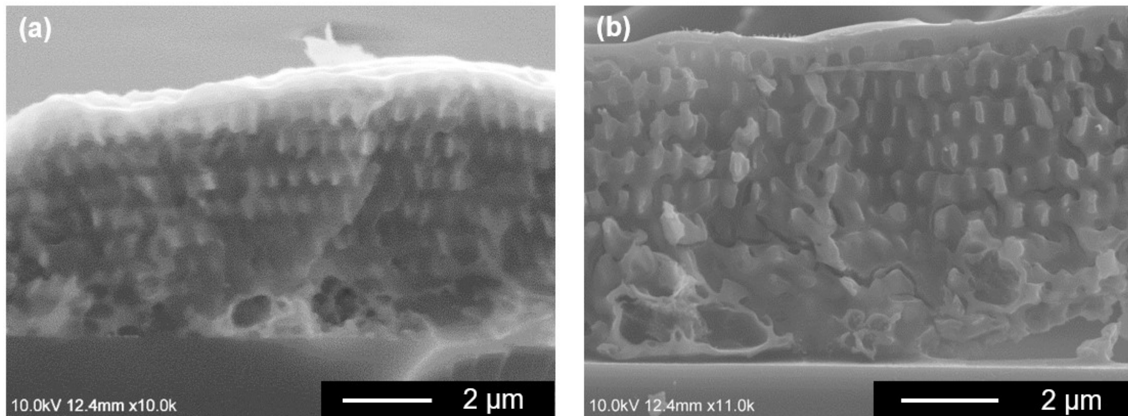

Figure 4.23 Cross-sectional SEM images of the a-Si:H nanostructures, (a): Before annealing, (b): After annealing (2 filling cycles, defoam/5min/3times, low spin speed).

4.3 Characteristics of 3D periodic a-Si:H nanostructure

4.3.1 Comparison between calculation of shrinkage rate by structural size evaluation and theoretical calculation

The a-Si:H nanostructures fabricated with the KMPR template have large deformation that cannot be evaluated as usual. Therefore, the a-Si:H nanostructure formed with SU8 template was used as the main sample to be evaluated. The same evaluations of the nanostructure's Talbot distance (Z_T), height and periodicity are summarized in Fig. 4.24 and Fig. 4.25. The 48.9% shrinkage of the Z_T occurred in the out-of-plane direction compared to the SU8 template, which was around 1.187 ± 0.235 μm. Therefore, the height of the nanostructure had comparable shrinkage, thus decreasing the height to 597 ± 86 nm. It is presumed that the two post-baking steps and the stress

changes during the post-baking are the main problems. Only 6.7% shrinkage happened in the periodicity of the a-Si:H nanostructures in the in-plane

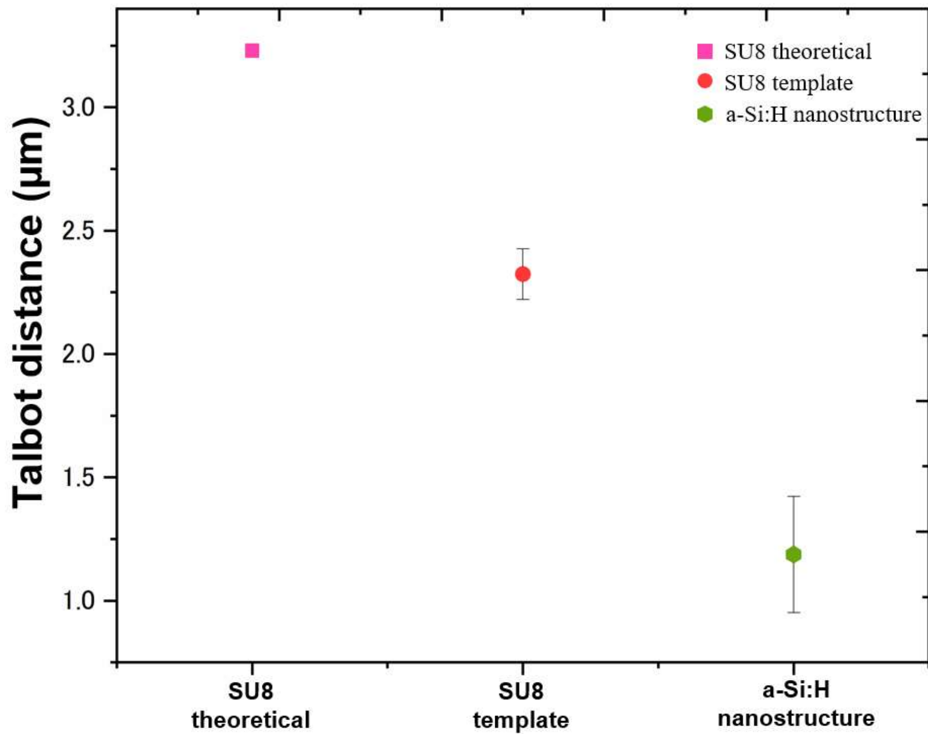

Figure 4.24 Distribution of the Talbot distance

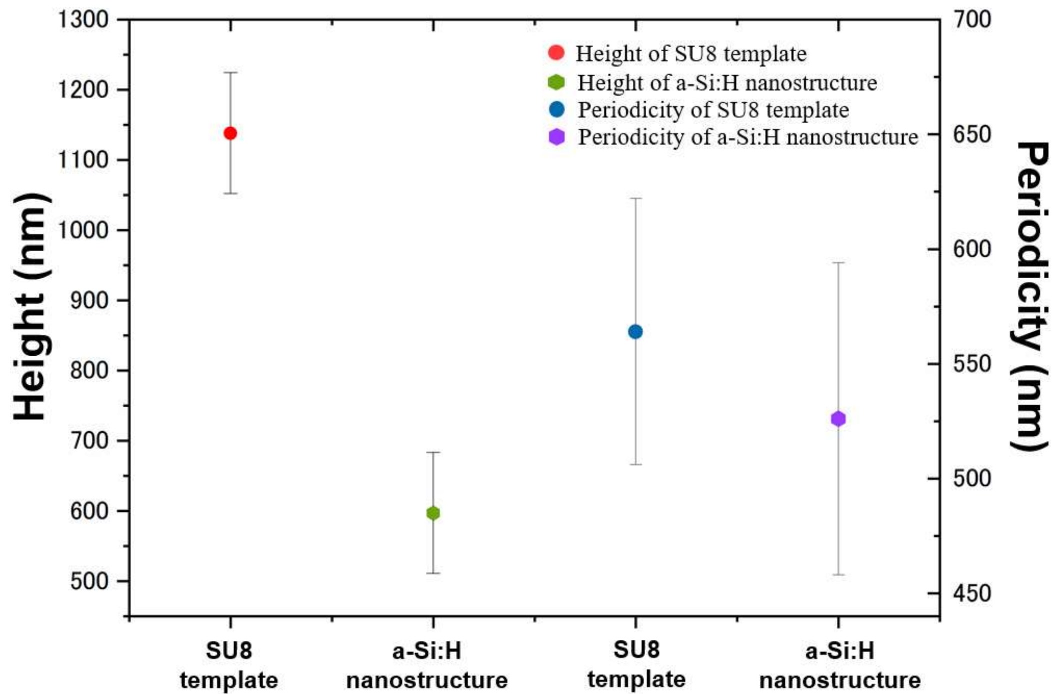

Figure 4.25 Distribution of the height and periodicity.

direction, indicating that the infiltration process with a solution-derived silicon can be effective in maintaining the periodicity in the in-plane direction, without strong deformation of the nanostructure. Since the mean free path (MFP) of the phonons of a-Si:H has not been studied at current stage, the influence of nanostructures on the thermal conductivity cannot be quantitatively identified.

4.3.2 Crystallographic analysis of a-Si:H nanostructure by XRD

Since the solution-derived silicon used here is amorphous, the XRD spectra of the Si thin film and Si nanostructure shown in Fig. 4.26 also shows

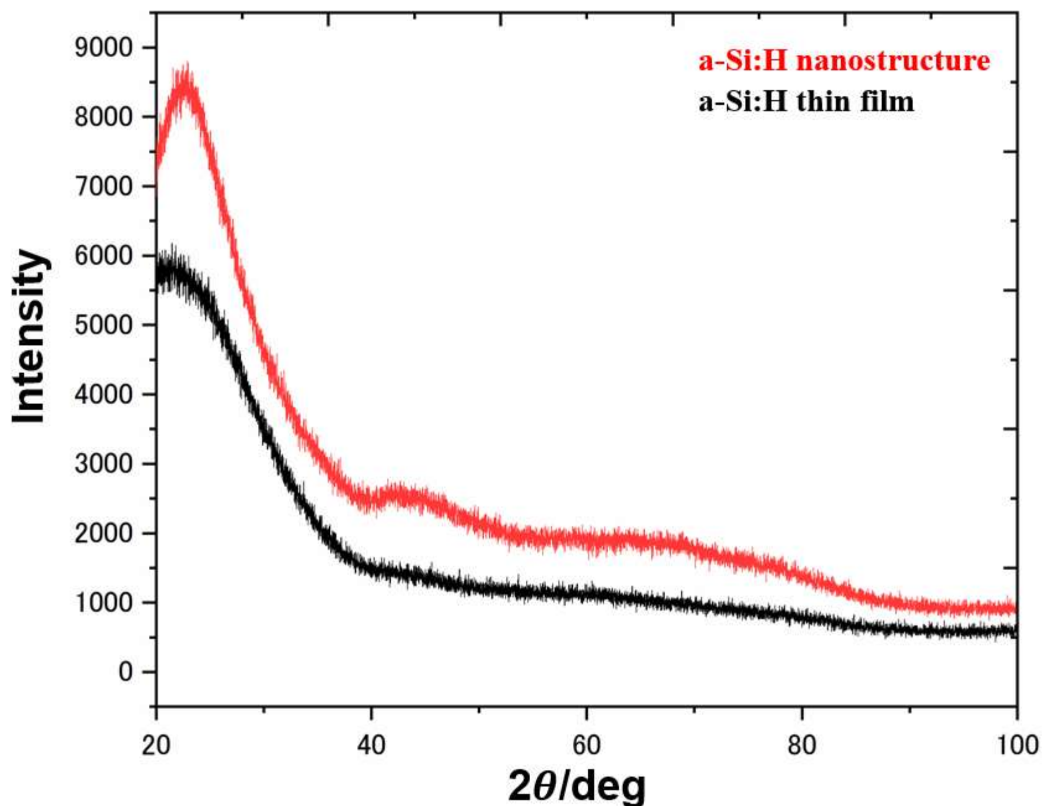

Figure 4.26 XRD analysis of the a-Si:H film and a-Si:H nanostructure.

that the formed Si film and nanostructures are amorphous. The noise in the XRD spectra originates from the carbon element which are not completely removed as abovementioned. At the same time, there are some broad peaks can be observed, showing that the crystallinity is likely to change very slightly due to the high temperature post-baking and annealing. Therefore, the transmission electron microscope (TEM) observation was used to reconfirm the crystallinity. From the observation in Fig. 4.27, the thickness of the a-Si:H film was affirmed to be 88.47 nm. From analysis of the diffraction patterns, it seems that both amorphous and polycrystalline structures exist in the same Si film of different positions. Here, it demonstrates that the crystallinity partly changes under high temperature

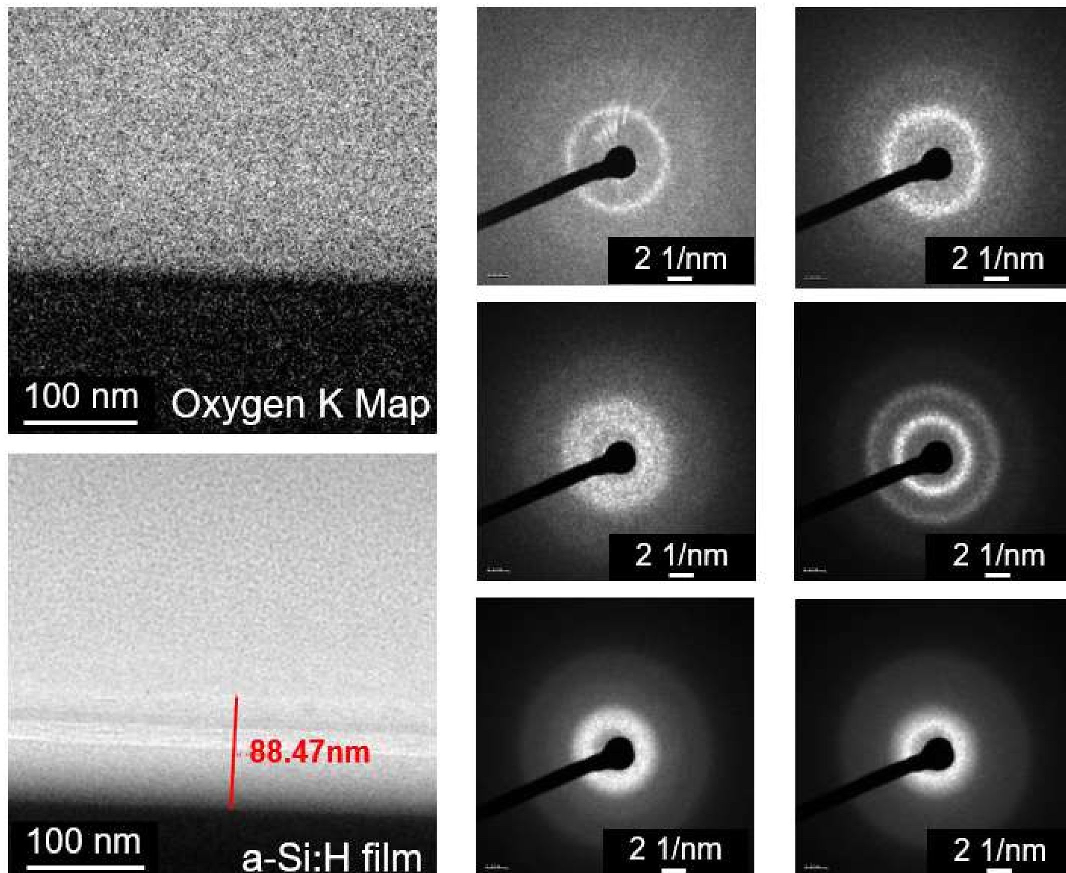

Figure 4.27 Cross-sectional TEM images and diffraction images of the a-Si:H film.

post-baking. Unfortunately, because of the porous network structure on the surface of the nanostructure, results in the TEM observation of nanostructure was not possible to be performed.

4.4 Summary

The inverse 3D periodic a-Si:H nanostructure was successfully fabricated via an infiltration process with a monomer solution-derived silicon in this chapter. The following useful conclusions are obtained through repeated and optimization experiments:

(a) The inverse 3D periodic a-Si:H nanostructures formed with the KMPR template are not successful due to large and unexpected deformations.

(b) The inverse 3D periodic a-Si:H nanostructures with the surface residues are successfully fabricated with the SU8 template by using the defoaming step prior to the spin-coat step via 2 filling cycles.

(c) The hardness of the SU8 nanostructure template is higher than KMPR nanostructure template, which will be helpful for the infiltration of high concentration solution.

(d) The solution-derived silicon can perfectly penetrate the SU8 and KMPR nanostructure template, which is affirmed by EDX analysis. 26-30% of the carbon residue from the template is trapped in silicon that cannot be removed completely.

(e) The large shrinkage of the out-of-plane direction is confirmed, which is caused by the solution itself, high temperature post-baking, and annealing.

(f) The XRD and TEM data suggests that the crystallinity of a-Si:H slightly changes under high temperature post-baking.

References

[1] R. W. Collins, A. S. Ferlauto, G. M. Ferreira, C. Chen, J. Koh, R. J. Koval, Y. Lee, J. M. Pearce, C. R. Wronski, Solar Energy Materials & Solar cells., 78, 143 (2033).

[2] R. A. Street, Hydrogenated amorphous silicon, Cambridge University press Cambridge, 1991.

[3] A. Shah, W. Beyer, Thin-Film Silicon Solar Cells, EEPL Press, 17 (2010).

[4] A. Shan, M. Fried, G. Juhasz, C. Major, O. Polgar, A. Nemeth, P. Petrik, L. R. Dahal, J. Chen, Z. Huang, N. J. Podraza, and R. W. Collins, IEEE Joural of Photovoltaics., 4, 1, 355 (2014).

[5] R. C. Chittick, J. H. Alexander, and H. F. Sterling, J. Electrochem. Soc., 116, 77 (1969).

[6] W. Paul, D. A. Anderson, Solar Energy Materials., 5, 3, 229 (1981).

[7] H. Wada, and T. Kamijoh, Jpn. J. Appl. Phys., 35, 648 (1996).

[8] S. Moon, M. Hatano, M. Lee, C. P. Grigoropoulos, International Joural of Heat and Mass Transfer., 45, 2439 (2002).

[9] D. G. Cahill, M. Katiyar, and J. R. Abelson, Physical Review B., 50, 9 (1994).

[10] N. Attaf, M. S. Aida, and L. Hadjeris, Solid State Communications., 120, 525 (2001).

[11] X. Liu, J. L. Feldman, D. G. Cahill, R. S. Crandall, N. Bernstein, D. M. Photiadis, M. J. Mehl, and D. A. Papaconstantopoulos, Physical Review Letters., 102, 035901 (2009).

[12] T. Masuda, Y. Matsuki, T. Shimoda, Thin Solid Films., 520, 6603 (2012).

[13] T. Masuda, Y. Matsuki, and T. Shimoda, Polymer., 53, 2973 (2012).

[14] T. Masuda, and T. Shimoda, Jpn. J. Appl. Phys., 53, 02BA01 (2014).

[15] T. Masuda, H. Takagishi, K. Yamazaki, and T. Shimoda, ACS Appl. Mater. Interfaces., 8, 9969 (2016)

[16] T. Shimoda, Y. Matsuki, M. Furusawa, T. Aoki, I. Yudasaka, H. Tanaka, H. Iwasawa, D. Wang, M. Miyasaka, and Y. Takeuchi, Nature, 440, 6 (2006).

[17] T. Masuda, H. Takagishi, Z. Shen, K. Ohdaira, and T. Shimoda, Thin Solid Films., 589, 221 (2015).

[18] Z. Shen, T. Masuda, H. Takagishi, K. Ohdaira, and T. Shimoda, Chem. Commun., 51, 4417 (2015).

[19] T. Masuda, N. Tatsuda, K. Yano, and T. Shimoda, Scientific Reports, 6, 37689 (2016)

[20] S. Araki, Y. Ishikawa, X. D. F. Wang, M. Uenuma, D. Cho, S. Jeon, and Y. Uraoka, Nanoscale Research Letters., 12, 419 (2017)

Chapter.5 Characteristics of the ZnO and a-Si:H 3D nanostructures

5.1 Optical characteristics of the ZnO and a-Si:H 3D nanostructures

In order to evaluate the optical characteristics such as the formation of photonic bandgap, the reflectance and transmittance spectra of the ZnO 3D nanostructure and a-Si:H 3D nanostructure were measured using a ultraviolet visible (UV-Vis, V-570, JASCO Corporation) spectrometer.

5.1.1 Reflectance and transmittance of the ZnO 3D nanostructures

The reflection spectra in Fig. 5.1(a) illustrates that the ZnO film (thickness: ~100 nm) has a reflectance around 18% at 390 nm. The small decrease in reflectance was confirmed on the shorter wavelength side (~340 nm) which

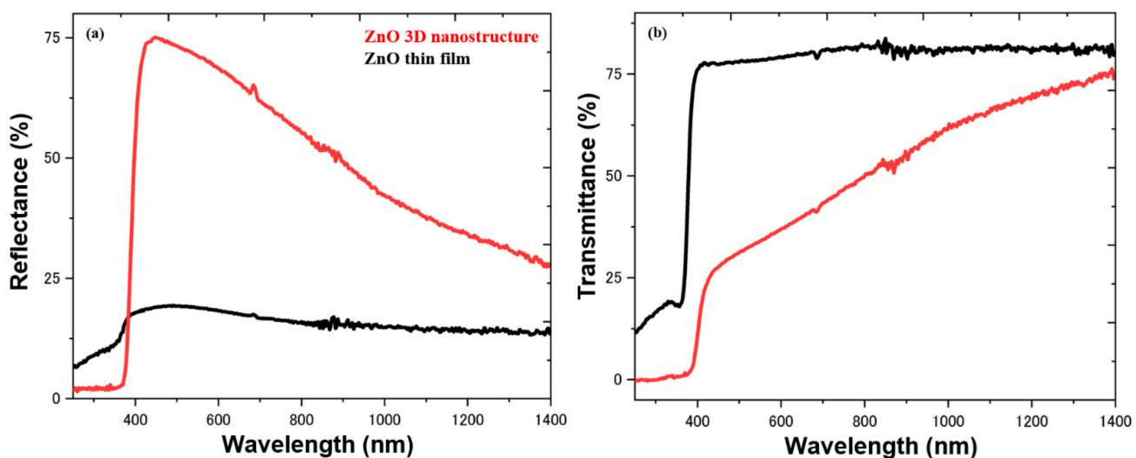

Figure 5.1 The reflectance (a) and transmittance (b) of the ZnO film and ZnO 3D nanostructures.

is considered to be ZnO absorption. For the ZnO 3D nanostructures (thickness: ~8 μm), the reflection peak was observed at 440 nm, and the absorption was also confirmed with a sharp decrease at around 400 nm. The reason why ZnO 3D nanostructures have a higher refection is because the incident light was effectively scattered through the 3D periodic nanostructures [1]. However, with the increasing wavelength the reflectance decreased, which is possibly caused by the high porosity of the structure [2]. It has been experimentally proved that the formation of the photonic bandgap will result in the reflectance of a specific wavelength region reaching 100% [3]. However, the maximum reflectance peak in Fig. 5.1(a) is around 75%, which was possibly caused by the disorder and defects located in the ZnO 3D nanostructure. The transmittance spectra (Fig. 5.2(b)) of the ZnO film shows good transmittance properties (around 76%) from 405 nm. However, the transmittance decreased for the 3D nanostructures, due to the scattering caused by the periodic nanostructures.

5.1.2 Reflectance and transmittance of the a-Si:H 3D nanostructures

The reflectance of the a-Si:H film (thickness: ~88 nm) in Fig. 5.2(a) shows a peak around 700 nm, and it is higher than the a-Si:H 3D nanostructures (thickness: ~3 μm) in the whole measurement wavelength. The reason is that the surface reflectance is reduced due to the load of the concave-convex structures on the surface of a-Si:H, which has a high refractive index.

Moreover, this also can be possibly attributed to defects of the nanostructure and the material used, which causes an increase in the light absorption and reduction of the reflection [4]. It can be also inferred from the absorption and scattering in the 3D nanostructures that the transmittance of the a-Si:H 3D nanostructure is lower than the film as shown in Fig. 5.2(b). The difference in the transmittance and reflectance spectra can be attributed to the difference in the fabrication method of the film and the nanostructures.

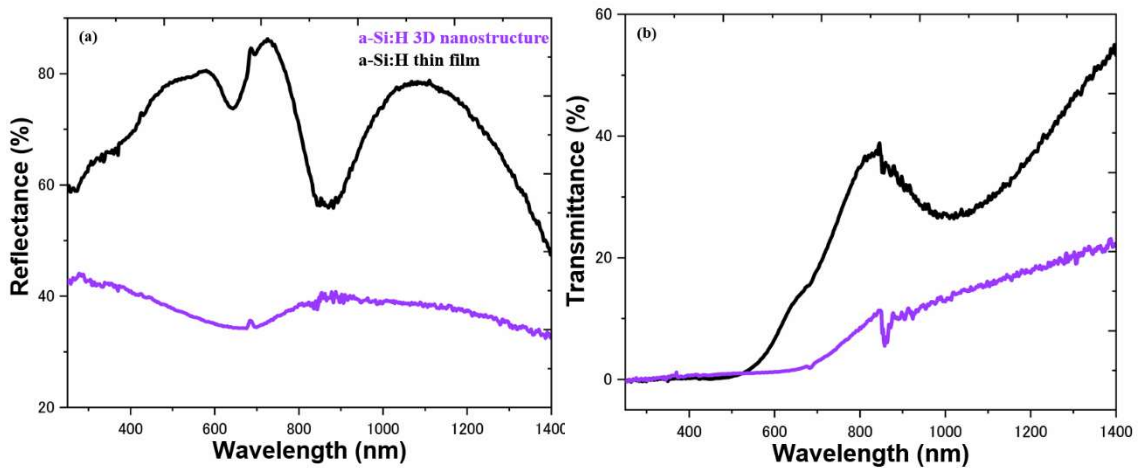

Figure 5.2 The reflectance (a) and transmittance (b) of the a-Si:H film and a-Si:H 3D nanostructures.

5.2 Seebeck coefficient and electric conductivity of the ZnO and a-Si:H 3D nanostructures

5.2.1 Evaluation methodology

Assuming that, the cross-section and physical composition of the materials are assumed to be uniform across the sample, the electric conductivity (σ) can be calculated by:

$$\sigma = \frac{1}{\rho} = \frac{l}{RA} \tag{5.1}$$

where ρ is the electrical resistivity, R is the electrical resistance, l is the length of the specimen, and A is the cross-sectional area of the specimen. As for the Seebeck coefficient (S), it is can be defined as:

$$S = -\frac{\Delta V}{\Delta T} \tag{5.2}$$

when the temperature gradient of the two ends of a material is small. Here, ΔV is the thermoelectric voltage shift measured at the electrodes, and ΔT is the temperature gradient. In this study, the samples measured were treated as ideal models to reduce the difficulty of measurement. In order to obtain the ΔT, the sample was placed on a platform with a pair of Peltier devices which induces ΔT by applying a voltage with a power supply. Using an infrared heat generation analyzer (QFI: Infrascope II), a temperature value accurately to six decimal places can be achieved in real time. Two probes from the semiconductor parameter analyzer (Agilent Technologies: 4156C) are used to measuring the ΔV from I-V curve. The photograph of the device and the schematic diagram of each part are shown in Fig. 5.3.

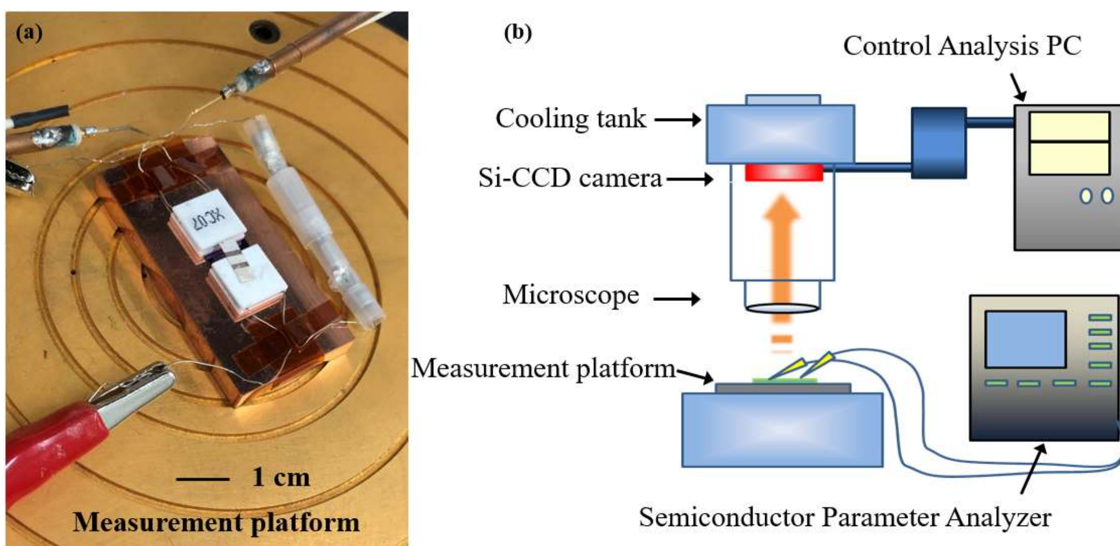

Figure 5.3 Photograph of measured device (a) and schematic diagram of the measurement system (b)

5.2.2 Preparation of electrodes

In this evaluation, the electrodes are shown in Fig. 5.4(a) wherein the four electrodes are parallel to each other with an intermediate interval of 10.6 mm, and the adjacent electrodes have an interval of 1.7 mm. Evaluation of the physical properties of materials and thin films can be done using a physical property measurement system (PPMS). However, PPMS is not suitable to measure this sample because the adhesive used diffuses inside the nanostructure. In order to reduce the error from the unformed part of the nanostructures, two electrodes adjacent to each other are selected for the determination by using the system mentioned in Sec. 5.2.1 (Fig. 5.4(b)). Furthermore, the Au electrodes with the thickness of 250 nm were made with electron-beam (EB) deposition, which can effectively reduce the resistance of the samples.

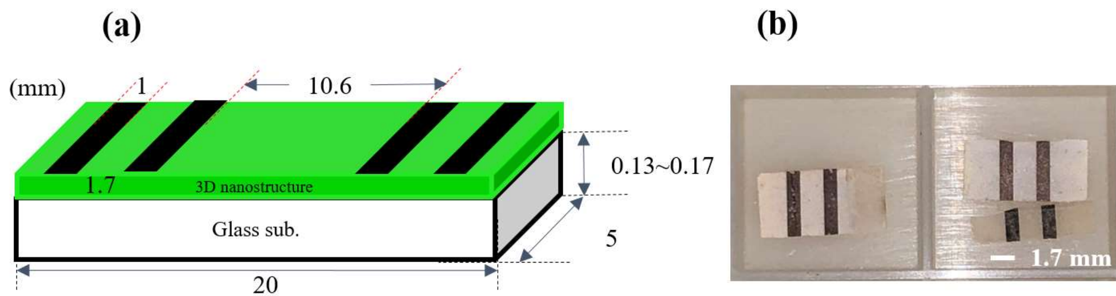

Figure 5.4 The electrodes setting of the measurement (a) and final setting with samples (b).

In Chap. 3, ZnO is post-baked in an oxygen environment to reduce the change in refractive index [5], but this increases the resistance of ZnO. Therefore, before measurement, further annealing was performed in a tube furnace at 400ºC for 2h under a flow of a gaseous mixture of H_2 (2%) and N_2 (98%) to reduce the oxygen in the structure. Annealing with H_2 creates

an equilibrium of defect concentration, which can effectively stabilize the chemically derived films, thus eliminating hysteresis during thermoelectric measurements [6].

5.2.3 Seebeck coefficient and electric conductivity of the ZnO 3D nanostructure

After the H_2 annealing mentioned in last section, measurements in the kΩ range were carried out for the ZnO 3D nanostructure. Using of the measurement system introduced in Sec. 5.2.1, I-V curves were measured as follows with different ZnO concentrations and at different heater voltages (0V, 0.7V, 1.4V, 2.1V, 2.8V and 3.5V) to make a temperature gradient (Fig. 5.5(a-c)). The voltage shift direction in Fig. 5.5(a) is opposite to that of the other two samples, which is caused by the opposite direction of the probe connection during measurement. At the same time, the temperature change corresponding to the voltage change was also measured by the infrared microscope. (Fig. 5.5(d))

Therefore, the relationship between the ΔV and ΔT were plotted in Fig. 5.6. And From Eq. 5.1 and 5.2, the σ and S were calculated and summarized in Table 5.1. It is demonstrated that the $|S|$ increases when the ZnO concentration increased. This may be attributed to the decrease in ZnO concentration leading to an increase in porosity resulting in an increase of carrier concentration. Among three samples, the sample with the ZnO concentration of 0.30 mol/L has the highest conductivity. This is due to the

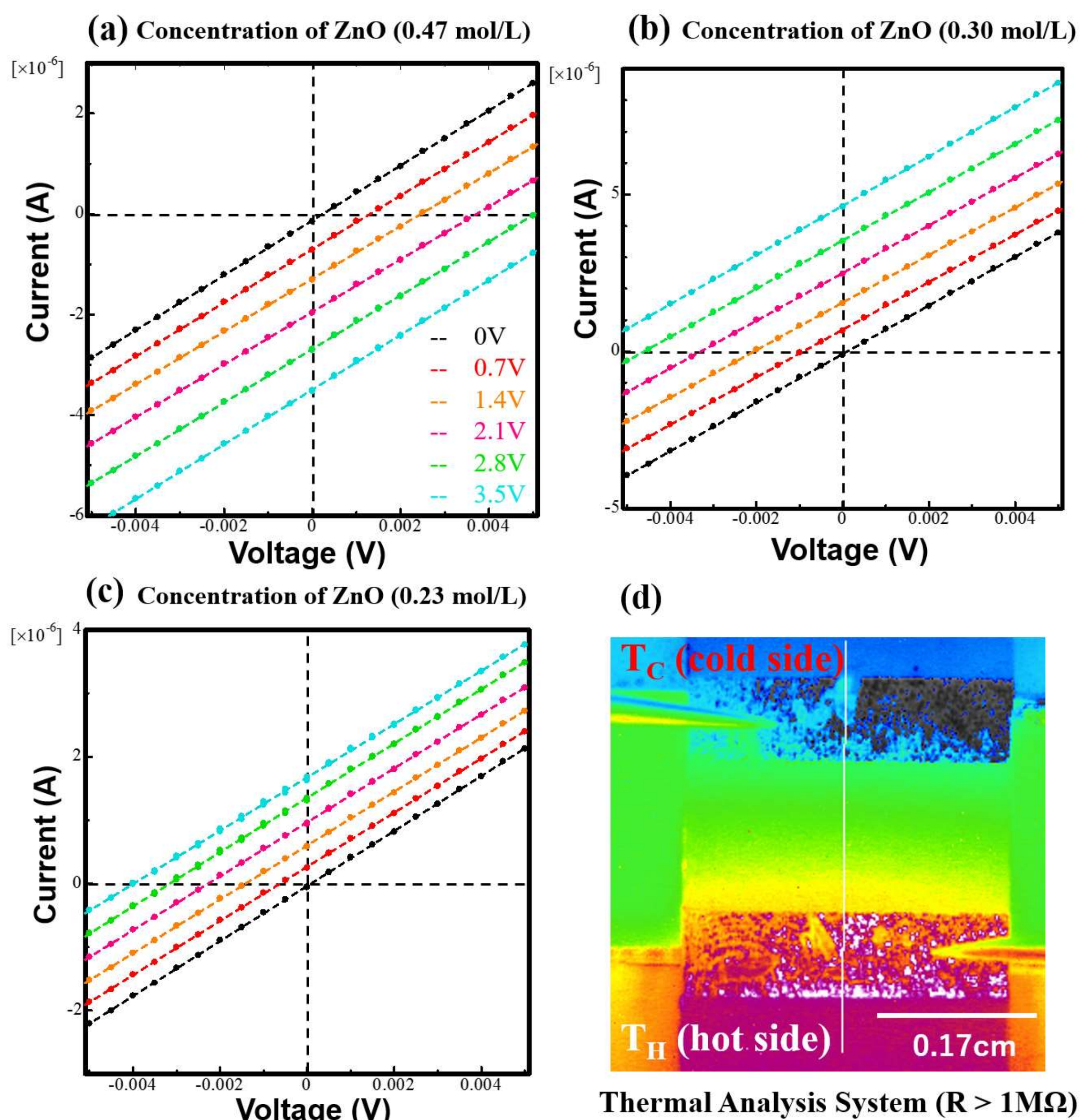

Figure 5.5 The I-V curves with different ZnO concentrations (a): 0.47 mol/L, (b): 0.30 mol/L, (c): 0.23 mol/L, and (d): image of temperature gradient.

difference in resistance caused by the concave-convex surface structure formed by periodic nanostructures, as well as the collapse or missing of nanostructures, make accurately measuring the resistance difficult. Unfortunately, the resistance of the ZnO film fabricated in this study is too high to be measured. It is highly recommended to re-measure the properties after the uniformity of the film can be maintained, which will result in more

accurate measurements brought about by the introduction of nanostructures.

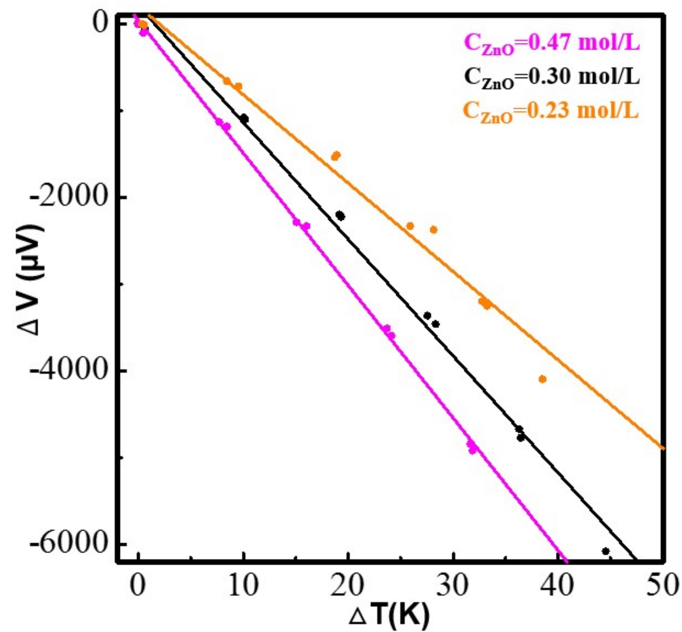

Figure 5.6 The ΔV-ΔT curves of the ZnO 3D periodic nanostructures with different concentration.

Table 5.1 Summary of the related parameters of ZnO.

Concentration of ZnO (mol/L)	0.47	0.30	0.23
R Before annealing (Ω)	270M	430M	160M
R After annealing (Ω)	1.6k	1.2k	2.4k
Distance of two electrodes (cm)		0.17	
Thickness (μm)	8.9	8.9	8.4
Electric conductivity (S/cm)	0.268	0.329	0.196
Seebeck coefficient (μV/K)	-155	-135	-102
Power factor (μW/mK^2)	0.644	0.600	0.204

5.2.4 Seebeck coefficient and electric conductivity of the a-Si:H 3D nanostructure

The same measurement without H_2 annealing as above is also used to evaluate the S and σ of the a-Si:H 3D nanostructure. The I-V curves and ΔV - ΔT curves were plotted in Fig. 5.7. Table 5.2 shows that the nanostructures of a-Si:H have a low electrical conductivity and S, which may be caused by structural defects, surface residues and low hydrogen content. In addition, a large amount of carbon residues from the temple also can bring the large influence. Therefore, further evaluation is needed.

Table 5.2 Summary of the related parameters of a-Si:H.

a-Si:H 3D nanostructure	
R After annealing (Ω)	1111
Distance of two electrodes (cm)	0.17
Thickness (μm)	4.2
Electric conductivity (S/cm)	0.729
Seebeck coefficient (μV/K)	-12
Power factor (μW/mK^2)	0.0105

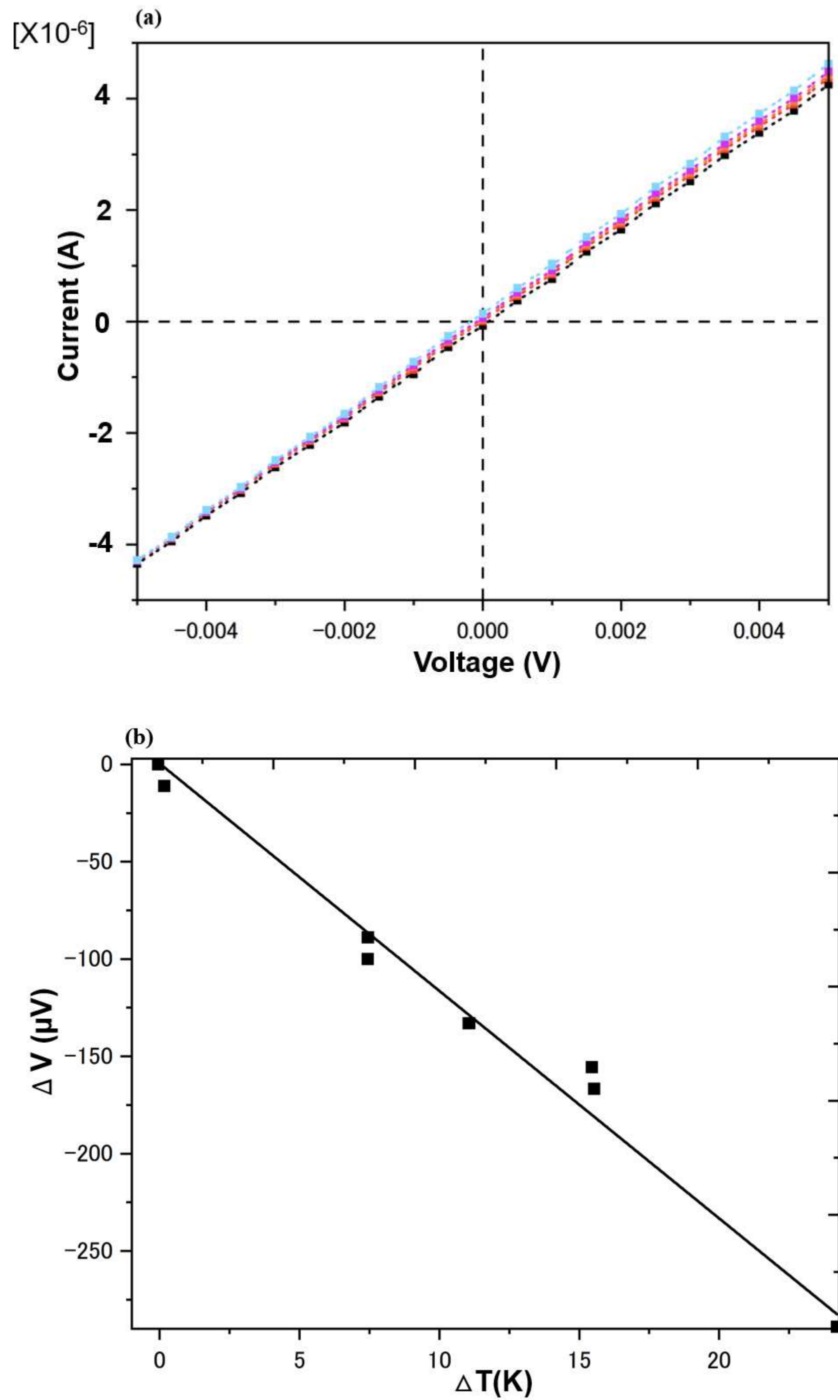

Figure 5.7 The I-V curves (a) and ΔV-ΔT curve (b) of the a-Si:H 3D periodic nanostructure.

5.3 Thermal conductivity of the ZnO 3D nanostructures

5.3.1 Effective thermal conductivity simulation by COMSOL

In this section, the multiphysics simulation software (COMSOL, COMSOL Inc) was used to analyze the effective thermal conductivity (κ_{eff}) under an ideal model of the 3D periodic nanostructures. The schematic diagram of the simulation is shown in Fig. 5.8. After setting the top to

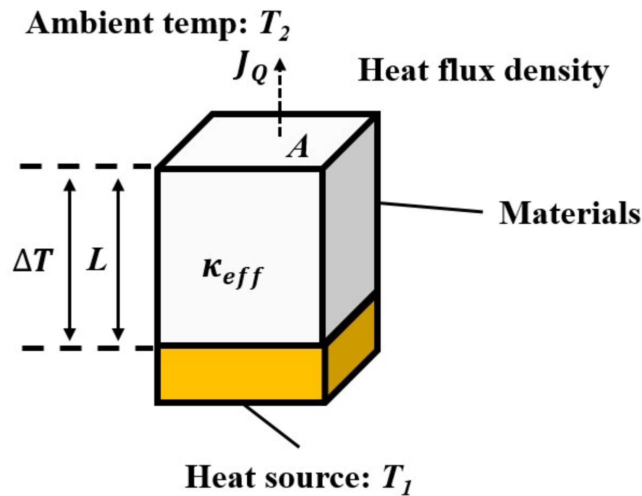

Figure 5.8 Simulation calculation principle diagram.

ambient temperature (T_2), a heat source (T_1) is added to the bottom of the structure to simulate the temperature gradient of the structure (ΔT). Therefore, the κ_{eff} can be calculated from:

$$\kappa_{eff} = \frac{L}{\Delta T} J_Q \quad (5.3)$$

where L is the height of the structure, J_Q is the heat flux density that can be expressed as:

$$J_Q = Q/A = \frac{T_1 - T_2}{\frac{L}{\kappa_{eff}} + \frac{1}{h}} \quad (5.4)$$

where h is the heat transfer coefficient. Because the inside of the

nanostructures in this study is considered to be filled with air, the forced convective heat transfer of the gas is applied here. As a result, after knowing the L, h, and ΔT, the κ_{eff} can be evaluated by:

$$\kappa_{eff} = \{\frac{[(T_1 - T_2) - \Delta T]hL}{\Delta T}\} \tag{5.5}$$

The geometries for simulation was build up as shown in Fig. 5.9(a). The blue part in Fig. 5.9(a) is defined as the ZnO nanostructure, and the rest is air. Table 5.3 and Fig. 5.10 show all the parameters set of the simulation. As in there, the thermal conductivity of the ZnO is set at 3.8 Wm^{-1}K^{-1}, which is obtained from the ZnO thin film fabricated with the sol-gel method [7]. Moreover, the relationship between the κ_{eff} and porosity was evaluated by

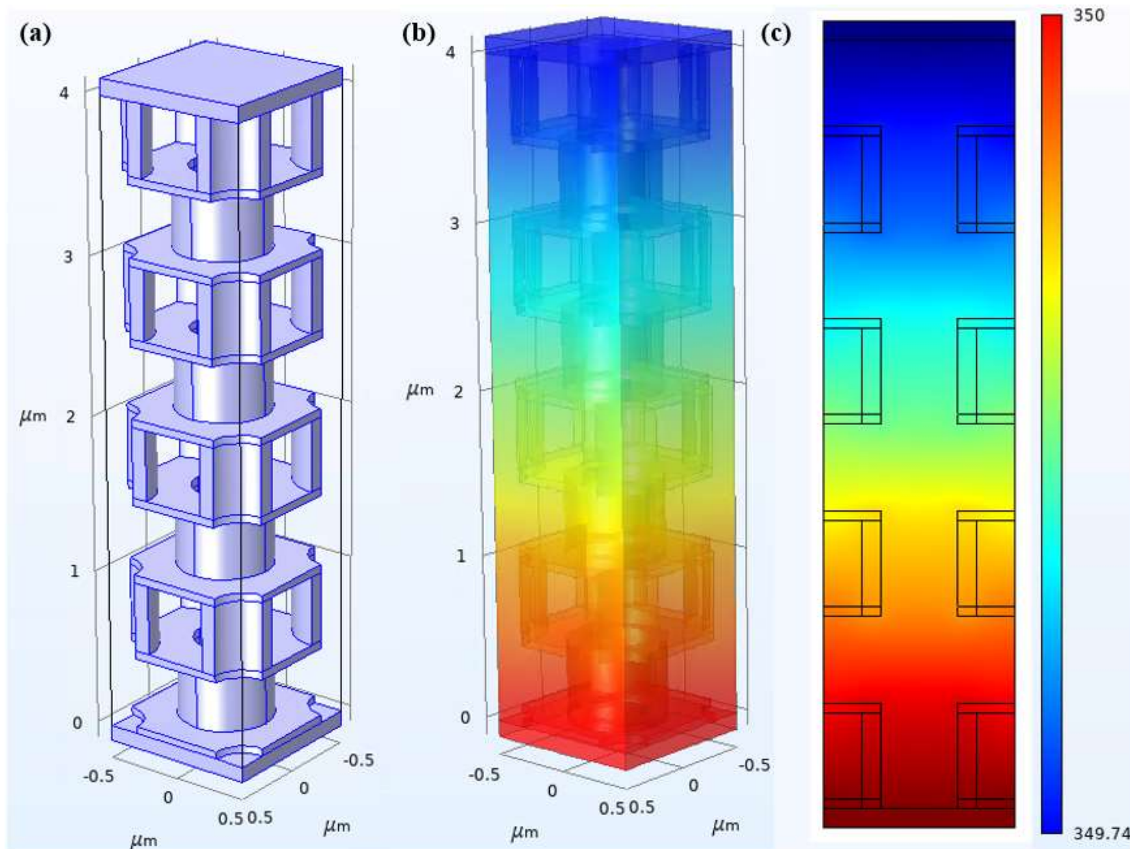

Figure 5.9 Simulation geometries (a), 3D temperature distribution (b), and y-z plane temperature distribution.

adjusting the thickness of the nanostructure, which can also be achieved in the actual nanostructure. As seen in Fig. 5.11, the κ_{eff} decreases with the increase of porosity, and they are generally smaller than the theoretical model [8,9] under the same porosity, which are possibly due to an ordered arrangement of nanostructures.

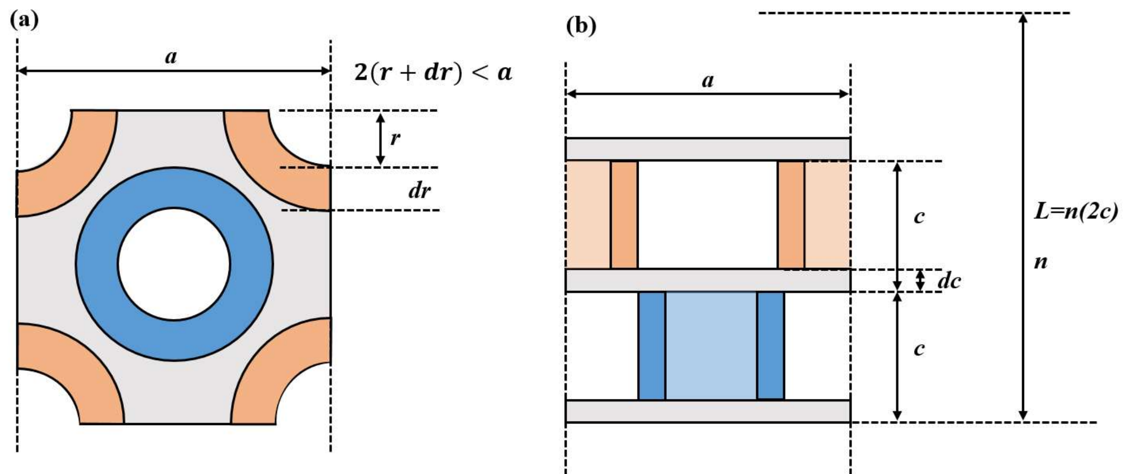

Figure 5.12 Horizontal plane (a), and cross plane (b) of geometries.

Table 5.3 Detailed setting parameters of the geometry.

Parameters	Value (μm)
L	n*2*c=4
a	1
r	0.2
c	0.5
n	4
dc	0.05
dr	0.1

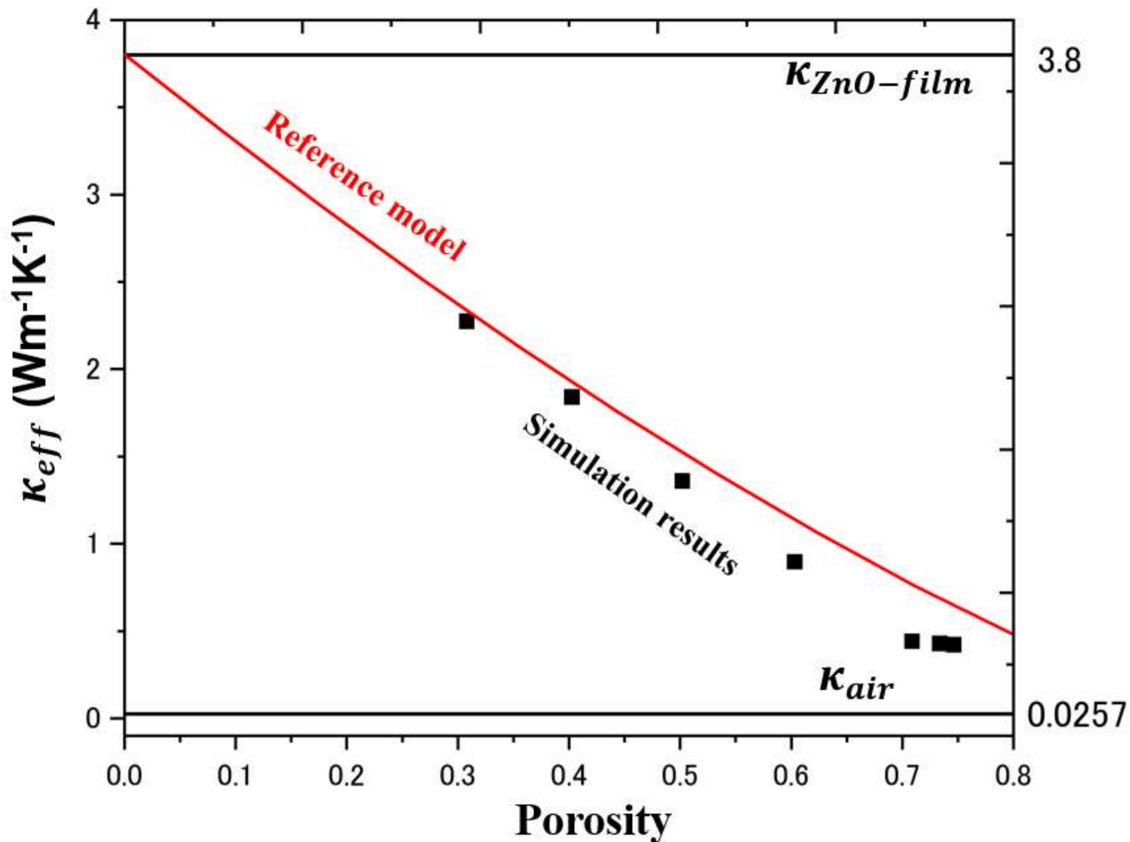

Figure 5.11 The relationship between the κ_{eff} and porosity.

5.3.2 Evaluation methodology of thermal conductivity

Thermal conductivity measurements for thin film and nano-scale structures is very difficult due to the lack of precision of the measurement device to accurately measure the ΔT. Nevertheless, there are still some methods which can measure the thermal conductivity (κ):

① Laser flash method: The laser flash method is a method that can calculate the κ through measured thermal diffusivity of samples in the out-of-plane direction. It is based upon the measurement of the temperature rise at the rear face of the sample produced by a short energy pulse on the front face. However, this method has a large error because it requires

multiple parameters to be measured (thermal diffusivity, specific heat, and density), and it is also difficult to measure samples with a thickness lower than 100 nm.

② Time-domain thermoreflectance (TDTR) method: The TDTR method derive the thermal properties by measuring the surface reflectance change, which caused by the material being heated. Generally, it can be applied to most thin film materials, except anisotropic thin-films.

③ 3ω method: The 3ω method is a well-known thin-film measurement of the out-of-plane and in-plane thermal conductivity. The heater and sensor of the measurement system belong to the same part which is realized by depositing the metal pattern on the film. It is a method that calculates κ through the relation between the metal electrode's temperature and the voltage frequency, which is from the metal electrode pattern on the surface that is heated up from a voltage signal measured at a specific frequency [10-14].

Among the aforementioned methods, the 3ω method is the most ideal approach for this study, which can accurately measure the κ for isotropic and anisotropic structures.

5.3.3 Mechanism and implementation of 3ω method

In this study, the function generator is used to output the electric signal at a frequency ω by setting the probes on the metal electrode (Fig. 5.12). The

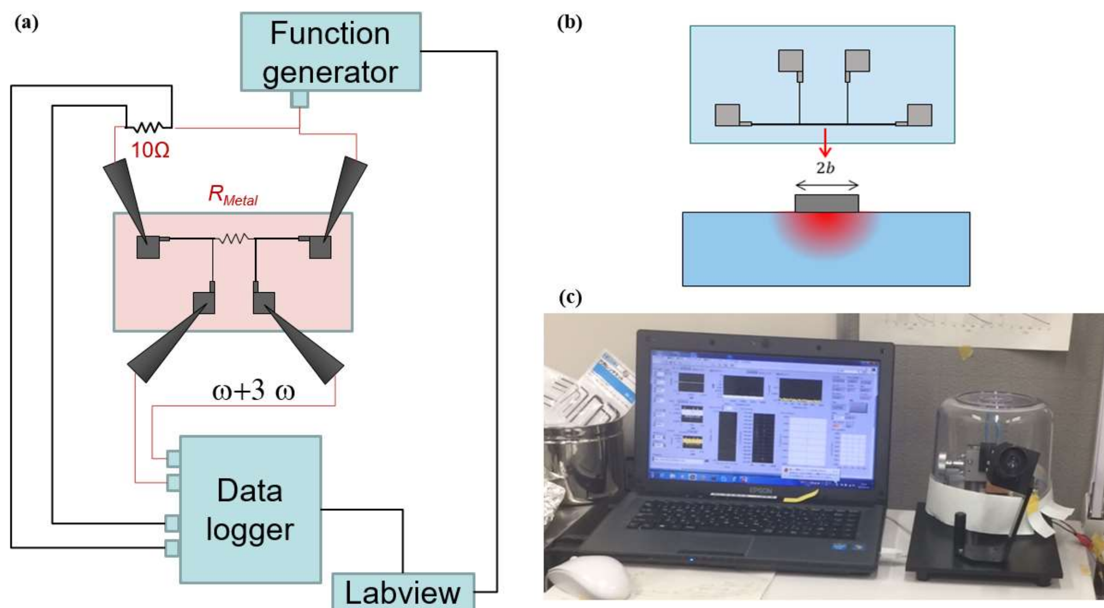

Figure 5.12 Measurement system diagram of 3ω method (a), measurement principle diagram (b), and physical map of the system (c) [16].

relation between the electric signal and temperature can be obtained from this electric signal, which will help approximate the electric signal frequency region that depends on the substrate. Next, calculate the thermal power's signal at 2ω frequency according to Ampere's law. The reason for calculating the thermal power's signal is because the increase of the resistance should include the 2ω frequency due to the dependence of temperature on electric resistance. Then, the temperature of the electrode can be obtained from the voltage signal at 3ω frequency, which can be found after multiplying the changed electric resistance with the electric current at a frequency of ω. The Fourier transform is utilized to divide measured

voltage signals into 1ω and 3ω signals. Afterward, the connections between temperature and thermal conductivity are evaluated by solving the simultaneous equations of thermal diffusion equation and electric power equation at frequency 3ω. The control and calculation processing of all operations are completed using a prepared LabVIEW programs [15].

Among these methods, the relationship between electric signal frequency changes and temperature changes can be expressed as Eq. 5.6,

$$\Delta T(\omega) = \frac{P}{\pi \kappa_S} \int_0^{\infty} \frac{sin^2(kb)}{\sqrt{(kb)^2 (k^2 + \frac{2i\omega}{D_{sub}})}} dk + \frac{P d_f}{2b\kappa_f} \tag{5.6}$$

under two restriction conditions as:

$$b \ll \sqrt{\frac{D_{sub}}{2\omega}},\ \kappa_f < \kappa_S \tag{5.7}$$

where P is the electric current power, κ_S is the thermal conductivity of substrate, κ_f is the thermal conductivity of thin film, d_f is the thickness of thin film, $2b$ is the width of metal line, D_{sub} is the thermal diffusivity of substrate.

In general, Eq. 5.6 can be approximated as:

$$\Delta T = -\frac{P}{4l\pi\kappa} ln(w) + \frac{P d_f}{2b\kappa_f} \tag{5.8}$$

Through the measurements and calculations of the substrate and substrate with thin film, the κ_f can be calculated as

$$\kappa_f = \frac{P d_f}{2b[\Delta T_f(\omega) - \Delta T_S(\omega)]} \tag{5.9}$$

5.3.4 Preparation of the electrodes on the ZnO 3D nanostructures

As mentioned in the last section, the electrodes for the 3ω measurement is set as presented in Fig. 5.13. The total sample size was controlled with 1 × 0.5 cm. Nevertheless, due to the very small width of the metal line (20 μm) connecting the electrodes, it is easy to cause disconnection or poor contact of the electrodes due to problems such as high roughness and voids on the surface, which will lead to the deviation of the measurement results.

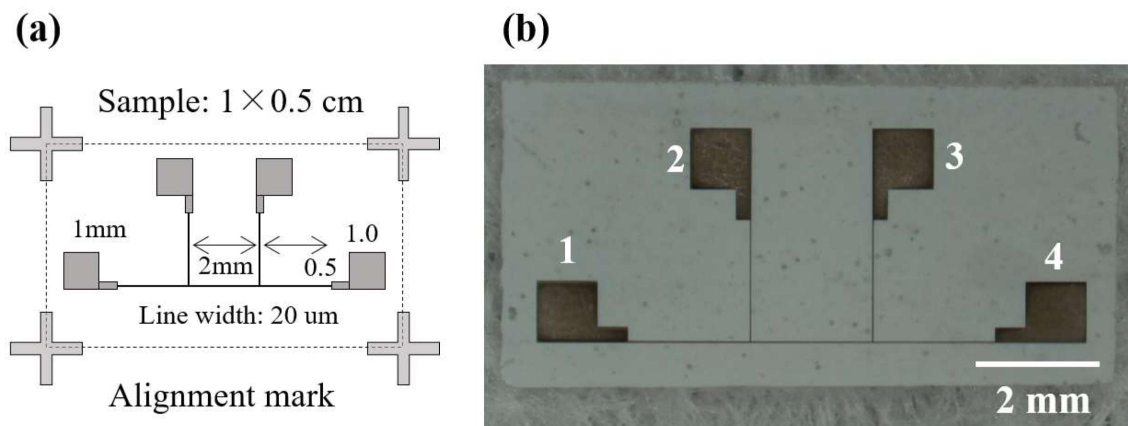

Figure 5.13 The electrode of 3ω method (a), and physical map of the sample (b).

The first iteration of the deposited electrodes was by using Al with 1 μm thickness. However, the resistance of those samples were as high as tens to hundreds of MΩ, which is hard to measure (Table 5.4). After the observation of the electrodes by optical microscopy, it was found that the high resistance was caused by electrode fractures, which are due to a cavity in the formed structure itself (Fig. 5.14). This kind of cavity originates from the structure fabricated in this study which cannot have 100% perfect periodic nanostructures, as already mentioned in Chap.2. The following methods are

suggested to solve the problem:

Table 5.4 The resistances of the ZnO 3D nanostructures with different concentrations. (Unit: Ω)

		R_{1-4}	R_{2-4}	R_{3-4}
2000 rpm	0.47 mol/L	36.4M	22M	7.4M
	0.30 mol/L	9.45M	7.43M	5.58M
	0.23 mol/L	6.68M	5.47M	4M
4000 rpm	0.47 mol/L	51M	19M	17M
	0.30 mol/L	60M	59M	14M
	0.23 mol/L	11.3k	12.3k	15.8k
Glass		56	60	43

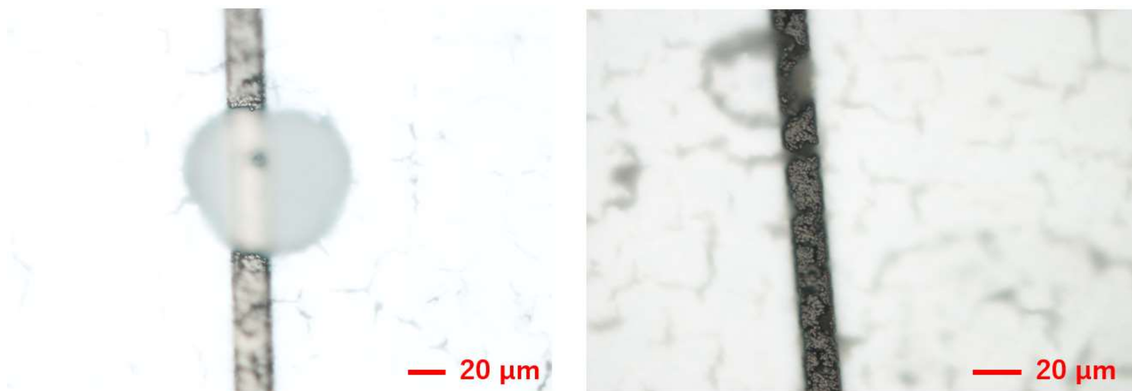

Figure 5.14 The electrodes fractured due to the cavity of the nanostructures.

① Make an independent film of ZnO 3D nanostructure by cutting, which is very challenging. Even if the film can be cut, it will affect the performance due to the errors and skills in the cutting process.

② Spin-coat an insulating film on the ZnO 3D nanostructure, then deposit the electrodes again, which must be done quickly. Nevertheless, because the nanostructures fabricated in this study are all highly porous structures,

when the material is spin-coated, it will penetrate into the nanostructures and cannot form a complete insulating film.

③ Increasing the thickness of electrodes to reduce the high resistance caused by the structural defects. By increasing the electrode thickness to 3 μm, the resistance of the ZnO 3D nanostructure was successfully reduced to a range of tens of Ω (Table 5.5). The energy dispersive X-ray (EDX) mapping in Fig. 5.15 illustrates that the electrodes deposited by electron beam does not enter inside of the nanostructures. However, the R_{Metal} of the reference glass substrate is too low to be measured accurately. This is because the measured resistance is lower than the lowest resistance (10 Ω) as shown in Fig. 5.12 that can be measured by the system. The experiment in the future is to control the resistance of the sample and substrate within the range of accurate measurement by adjusting the thickness of the electrodes, so as to measure the accurate thermal conductivity.

Table 5.5 The resistances of the ZnO 3D nanostructures with different concentrations after increasing electrode thickness. (Unit: Ω)

		$R_{1\text{-}4}$	$R_{2\text{-}4}$	$R_{3\text{-}4}$
4000 rpm	a	27	31	31
	b	39	36	27
	c	30	32	24
Glass	1	14	14	9

④ Deposit the electrodes before removal of the photoresist template, which will help reduce the influence from the substrate. Since the whole

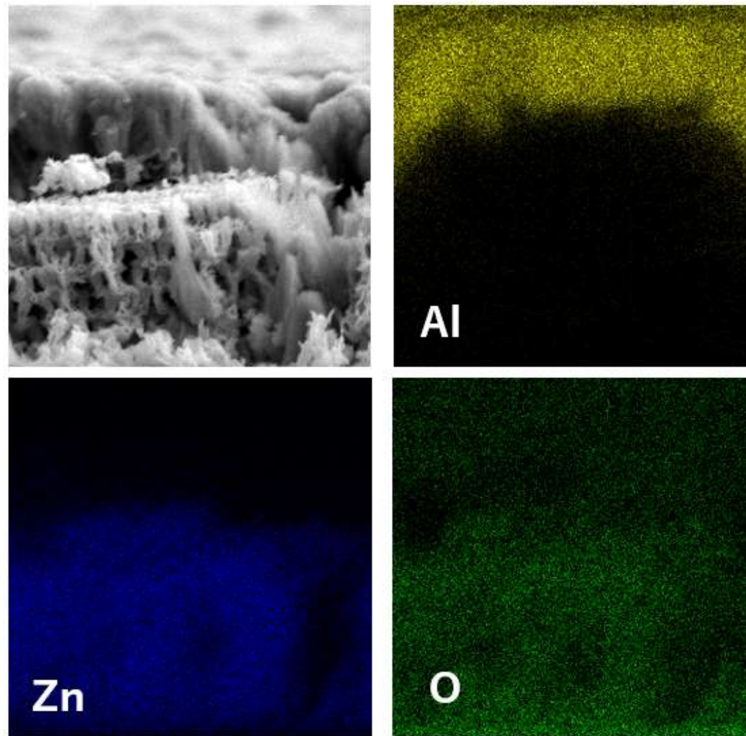

Figure 5.15 The EDX mapping of the cross-section image.

structure is basically complete before removing the original template, this method has high feasibility. In order to reduce the oxidation of the electrodes during the high temperature removing process, the Au with 600 nm thickness, which is difficult to oxidize, was used as the electrodes. After the removal process, some resistances cannot be measured due to

Table 5.6 The resistances of the ZnO 3D nanostructures with Au electrodes. (Unit: Ω)

(a)

		R_{1-4}	R_{2-4}	R_{3-4}
4000 rpm	a	-	-	-
	b	49	51	39
	c	62	65	46
6000 rpm	a	-	34	23
	b	39	220	28
	c	51	48	27
Glass	1	16	17	11
ZnO film	2	18	17	11

Before the final annealing

(b)

		R_{1-4}	R_{2-4}	R_{3-4}
4000 rpm	a	-	-	-
	b	31	-	17
	c	26	41	-
6000 rpm	a	-	-	-
	b	27	-	17
	c	31	28	17
Glass	1	15	16	10
ZnO film	2	16	16	10

After the final annealing

electrode damage, and the problem of low resistance still exists (Table .5.6). In the same method mentioned in last approach, the control of resistance can be expected to be within the measurable range.

⑤ Optimize the laser system by expanding the exposure range, so that the energy of exposure spot can be evenly distribute within the sample range. Therefore, a nanostructure with a completeness close to 100% can be obtained. This is to fundamentally eliminate the influence of this kind of nano-cavity.

⑥ As shown in Fig. 5.12, a smaller the electrode pattern is also an effective way. Due to the influence of the concave-convex surface structure in this research, the electrode must be thick. However, both electrodes metal (Al

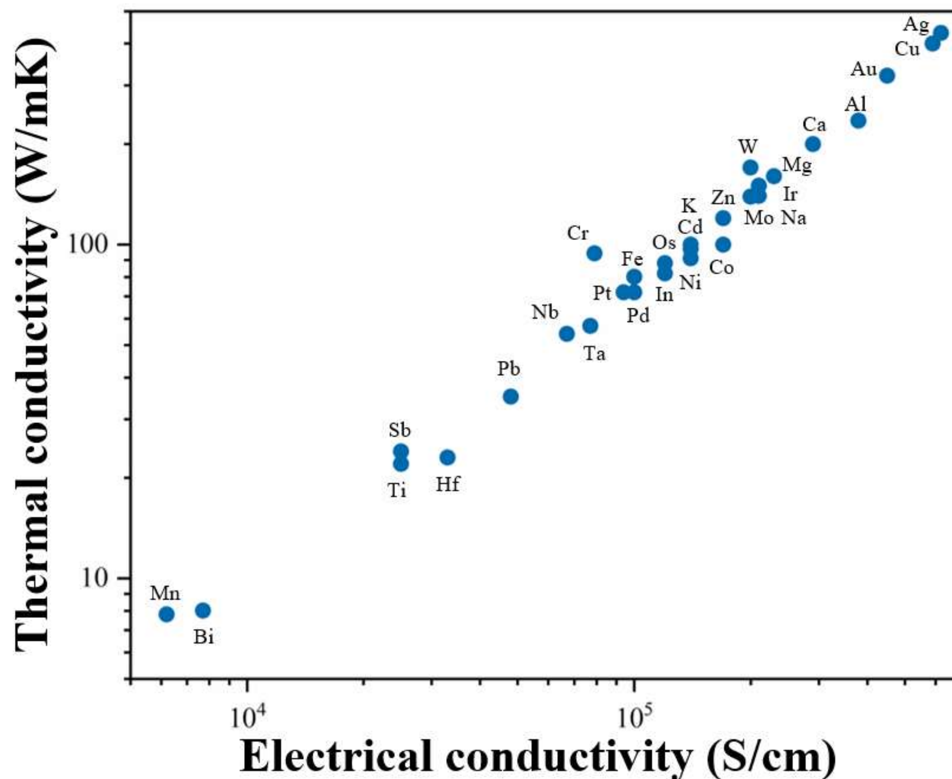

Figure 5.16 Relationship between thermal conductivity and electrical conductivity with different metals.

and Au) used here possess high electrical conductivity with low resistance as shown in Fig. 5.12. Therefore, considerations should be made in using other metal materials in the future, such as Mo, Ni, Bi, so that the thermal conductivity can be accurately measured.

5.4 Summary

In this chapter, the following conclusions are obtained by evaluating the optical and thermoelectric properties of ZnO and a-Si:H 3D periodic nanostructures:

(a) The 3D periodic nanostructures scattering can reduce transmittance and increase reflectivity effectively.

(b) The ZnO 3D periodic nanostructure can maintain the same electrical conductivity and obtain a higher S at the same time in contrast with the reference ZnO film at room temperature.

(c) The simulation results show that the high porosity 3D nanostructure can effectively reduce the effective thermal conductivity.

(d) The thermal conductivity cannot be measured due to resistance problems, but from the proposed method, it is can be expected to perform the accurate thermal conductivity measurements after optimization processes.

References

[1] H. Kim, and K. Yong, Phys. Chem. Phys., 15, 2109 (2013).

[2] M. Miyake, M. Suginohara, N. Narahara, T. Hirato, and P. V. Braun, Chem. Mater., 29, 9734 (2017).

[3] K. Ishizaki, and S. Noda, Nature., 460, 367 (2009).

[4] C. I. Yeo, J. H. Choi, J. B. Kim, J. C. Lee, and Y. T. Lee, Optical Materials Express., 4, 2, 346 (2014).

[5] S. Araki, Y. Ishikawa, M. Zhang, T. Doe, L. Lu, M. Horita, T. Nishida, and Y. Uraoka, Jpn. J. Appl. Phys., 52, 03BA02 (2013).

[6] A. Z. Barasheed, S. R. S. Kumar, and H. N. Alshareef, J. Mater. Chem. C., 1, 4122 (2013).

[7] Z.X. Huan, Z. A. Tang, J. Yu, and S. Bai, Physica B, 406, 4, 818 (2011).

[8] F. G. Cuevas, J. M. Montes, J. Cintas, and P. Urban, J. Porous Mater., 16, 675 (2009).

[9] I. Sumirat, Y. Ando, and S. Shimamura, J. Porous Mater., 13, 439 (2006).

[10] D. G. Cahill, Rev. Sci. Instrum., 61, 802 (1990).

[11] S. M. Lee and D. G. Cahill, J. Appl. Phys., 81, 2590 (1997).

[12] J. H. Kim, A. Feldman, and D. Novotny, J. Appl. Phys., 86, 3959 (1999).

[13] R. Venkatasubramanian, Phys. Rev. B., 61, 3091 (2000).

[14] S. T. Huxtable, A. R. Abramson, C. –L. Tien, A. Majumdar, C. Labounty, X. Fan, G. Zeng, J. E. Bowers, A. Shakouri, and E. T. Croke, Appl. Phys, Lett., 80, 1737 (2002).

[15] Chao He, Nara Institute of Science and Technology Doctor’s Thesis (2016).

Chapter.6 Conclusions and future works

6.1 Conclusions

The requirement for energy continues to grow with the progress and development of science and technology. Therefore, it is urgent to improve the efficiency of various energy sources usages. This research suggests that 3D periodic nanostructures can improve the efficiency of thermoelectric devices by reducing the thermal conductivity while maintaining a high power factor (*PF*). Therefore, this study concentrates on the fabrication process of the 3D periodic nanostructures, and aims to establish a new fabrication process for 3D periodic nanostructures by a non-vacuum process using solution-derived semiconductor materials. As a result of working on four interrelated research ideas, the following conclusions were reached:

In Chap.2, in order to fabricate the 3D periodic nanostructure, four setups of laser system were constructed, and the corresponding fabrication conditions were examined. After the process optimization, the 3D periodic nanostructures were successfully fabricated with KMPR and SU8 negative photoresists at 25 and 10 mJ/cm^2 total exposure doses, respectively. The reproducibility of the two different kinds of photoresist nanostructures has been successfully verified by repeated experiments. Moreover, the shrinkage in in-plane and out-of-plane directions, which caused by the cross-linking density and shrinkage of the photoresist itself were confirmed. The two nanostructures have different degrees of shrinkage in all directions, but the shrinkage factor of KMPR is lower than SU8, which is possibly caused by

the high crosslinking density of KMPR.

In Chap.3, the inverse 3D periodic ZnO nanostructure that cannot be reproduced with the previous fabricate conditions was successfully remade with a size limitation of 1 cm × 0.5 cm, through the controlled dropping amount of ZnO, and defoaming step carried out before the spin-coating step. The results also show that the nanostructures can be fabricated at different ZnO concentrations using both SU8 and KMPR templates. Moreover, it was also confirmed that the fully cured KMPR nanostructures could be completely removed by the solution process. However, due to the excessive swelling and strong oxidation in the solution process, all the structures peeled off from the substrate during the removal process after ZnO penetrates the nanostructure.

On the basis of the original shrinkage of photoresist, the out-of-plane direction shrink is caused by gravity, vaporization and shrinkage during the baking of the ZnO solution was confirmed. It is observed that the shrinkage of the in-plane direction is consistent with that of the SU8 nanostructure, which is attributed to the amount of dispensed ZnO solution as well as the defoaming step. Moreover, the grain sizes with different ZnO nanostructures were evaluated, which are smaller than the phonon mean free path of ZnO.

In Chap.4, the inverse 3D periodic a-Si:H nanostructures with the surface residues are successfully fabricated with a SU8 template after the fabrication process was optimized with 2 filling cycles, defoaming 3 times for total 15 min, and at low spin speed. The large shrinkage in the out-of-plane direction was confirmed from the solution itself, high temperature post-baking, and

annealing. Moreover, the slightly changed crystallinity of a-Si:H was observed in the XRD and TEM data.

In Chap.5, the measured transmittance and reflectance spectra demonstrated that the scattering from the 3D periodic nanostructures could reduce transmittance and increase reflectivity. Moreover, the ZnO 3D periodic nanostructure can maintain the same electrical conductivity and higher Seebeck coefficient can be obtained at the same time compared to the reference ZnO film at room temperature. The simulation with COMSOL illustrates that the high porosity 3D nanostructure can decrease the effective thermal conductivity effectively. Unfortunately, the thermal conductivity cannot be experimentally measured yet, but accurate measurements is under investigation after optimization processes.

6.2 Suggestions for future works

To conclude of this paper, future works and prospects are described below:

① Use of photoresist that can be removed by a non-swelling and non-oxidizing solution process.

In Sec. 3.2.4, the KMPR nanostructure that can be removed by the solution method which need strongly oxidized and swelled structures causing the inverse nanostructure to be peeled off from the substrate. For this reason, future work should consider introducing some photoresists that can be dissolved under very simple conditions (such as the cured photoresists that can be dissolved after cleaning with alcohol or acetone), which will facilitates the low-temperature formation process of the inverse

nanostructures. Moreover, the 3D nanostructure template produced by different photoresists are likely to be beneficial to the infiltration of other solution-derived semiconductor materials.

② Fabricate 3D periodic nanostructures on different substrates.

After successfully fabricating 3D nanostructures, various performance tests are needed to be performed. Although the 0.13–0.15 mm-thick glass substrate used in this research is within a measurable range, when the thickness of the substrate is lower than 0.13 mm, the performance test may be affected and it may even directly lead to large deviations in the results. For example, when using the 3ω method to measure the κ, because the substrate is too thin, the heat may diffuse to the test platform, which makes the measurement results inaccurate. Therefore, it is necessary to fabricate nanostructures on different substrates such as silicon wafer, sapphire substrate and so on. Different substrates will not only make performance testing easier, but also lay the foundation for future device manufacturing.

③ Fabricate a thermoelectric device with the inverse 3D periodic ZnO nanostructure.

In Chap.5, *PF* with inverse 3D periodic ZnO nanostructure has been confirmed to be able to maintain the same level as that of ZnO film. After confirming the decrease in thermal conductivity, it is possible to consider using the same method to make a 3D nanostructure of another material (or depositing another material to form a p-n junction by using traditional

photolithography techniques), and then combine those two different materials to form a p-n junction to produce a high-efficiency thermoelectric device.

④ Evaluation of thermoelectric conductivity of a-Si:H 3D nanostructure formed in this process.

The a-Si:H nanostructure fabricated in Chap.4 was too small to fabricate electrodes on the surface, therefore the thermoelectric properties could not be evaluated. Increasing the sample size will facilitate the successful evaluation of the thermoelectric properties of the device. It will not only help the formation of thermoelectric devices, but also facilitate the evaluation of other related properties.

⑤ Fabricate inverse 3D periodic a-Si:H with other kinds of solution-derived silicon.

In Chap.4, the periodic nanostructure of a-Si:H was successfully fabricated. However, because the monomer solution-derived silicon is used, it causes large shrinkage in the out-of-plane direction, and most of the nano-holes are completely filled. In the subsequent research, it is highly suggested using the polymer solution-derived solution to make 3D nanostructures, which have a high possibility to reduce shrinkage and retain nano-holes.

⑥ Try to make 3D periodic nanostructures with other different solution-derived semiconductor materials

In this study, the inverse 3D periodic nanostructure is fabricated by filling the 3D template of the photoresist, therefore the constituent material can be selected by changing the solution-derived materials. Therefore, there is a very high possibility to form various inverse 3D periodic nanostructures using these solution-derived semiconductor materials. It can be expected that these specially structured semiconductors can have very excellent characteristics, especially in the phonon engineering.

List of publications

I. Academic journals

1. Xudongfang Wang, Yasuaki Ishikawa, Shinji Araki, Mutsunori Uenuma, and Yukiharu Uraoka, "Removing process of the three-dimension periodic nanostructure fabricated from KMPR photoresist," Japanese Journal of Applied Physics 58, SDDF08, 2019.

II. International conferences

1. Xudongfang Wang, Yasuaki Ishikawa, Mutsunori Uenuma and Yukiharu Uraoka, "Removing process of the three-dimension periodic nanostructure fabricated from KMPR photoresist," 31st International Microprocesses and Nanotechnology Conference (MNC), 16P-11-45, Sapporo Hotel, 16/11/2018.

III. Domestic conferences

1. Xudongfang Wang, Yasuaki Ishikawa, Shinji Araki, Yukiharu Uraoka and Seokwoo Jeon, "Three-dimension periodic nano-structure fabricated by proximity nano-patterning process (PnP)", The Institute of Electronics, Information and Communication Engineers, Silicon Device and Materials (SDM), Kyoto University, 22/12/2017.

2. Xudongfang Wang, Yasuaki Ishikawa, Mutsunori Uenuma, and Yukiharu Uraoka, "Three-dimensional periodic ZnO nanostructures fabricated by

templating process using solution-derived ZnO," The 81th Japan Society of Applied Physics Spring Meeting (JSAP), 14p-A405-6, 2020.

IV. Research grant

1、王旭東方、高効率熱電変換素子を目指した三次元周期的ナノ構造の創製、平成 30 年度競争的研究支援、25 万円、2018 年.

V. Associated announcement

1. Shinji Araki, Yasuaki Ishikawa, Xudongfang Wang, Mutsunori Uenuma, Donghwi Cho, Seokwoo Jeon, and Yukiharu Uraoka, "Fabrication of 3D Periodic Structures using ZnO Solution with Non-Vacuum Process," The 64th Japan Society of Applied Physics Spring Meeting (JSAP), 14p-423-14, 14/3/2017.

2. Shinji Araki, Yasuaki Ishikawa, Xudongfang Wang, Mutsunori Uenuma, Donghwi Cho, Seokwoo Jeon and Yukiharu Uraoka, "Fabrication of Nanoshell-Based 3D Periodic Structures by Templating Process using Solution-derived ZnO," Nanoscale Research Letters 12:419, 2017.

3. Naoyoshi Noda, Yasuaki Ishikawa, Mutsunori Uenuma, Xudongfang Wang, and Yukiharu Uraoka, "Fabrication of ZnO phononic crystal toward high efficiency thermoelectric devices," The 16th Thin Film Materials & Devices Meeting, 09P16, 2019.

4. Pongsakorn Sihapitak, Yasuaki Ishikawa, Xudongfang Wang, Mutsunori Uenuma, and Yukiharu Uraoka, “Effect of phase shift mask design on three-dimension nanostructure fabrication,” The 81th Japan Society of Applied Physics Spring Meeting (JSAP), 13a-PB3-8, 2020.

5. Pongsakorn Sihapitak, Yasuaki Ishikawa, Xudongfang Wang, Mutsunori Uenuma, and Yukiharu Uraoka, “Relationship of phase shift mask design and size of three-dimension nanostructures,” The 27th International Workshop On Active-Matrix Flat Panel Displays and Devices (AM-FPD), P-4, online, 4/9/2020.

Acknowledgement

This research was conducted under the cooperation of many people. I would like to express my gratitude to everyone who supported this research.

First and foremost I would like to express my sincere to my research supervisor Prof. Yukiharu Uraoka, for his valuable advice, invaluable guidance on research, kindly encouragement and continuous support in my research and life throughout this five years.

I wish to express my deepest thanks and appreciation to Assoc. Prof. Yasuaki Ishikawa for providing me with all the necessary facilities. His valuable advice, suggestions, and critical comments help me overcome many difficulties. I am very grateful for each instruction and ideas he taught me, and it was a great honor to work and study under his guidance. And I would like to convey thanks to Prof. Hisao Yanagi for fruitful discussions and for giving me useful advice after every evaluation meeting. I would also like to thank as well Assoc. Prof. Nobuyoshi Hosoito for his patience, expert knowledge and encouragement extended to me.

I place on record my sincere gratitude and special thanks to Assoc. Prof. Mutsunori Uenuma and Asst. Prof. Michael Paul Jallorina for providing guidance, methodology knowledge, English revision and training in measurement with patience. Their opinions and suggestions are an important step to make my research successful.

I would like to express my heartfelt appreciation to Prof. Seokwoo Jeon, MSc. Donghwi Cho, MSc. Kisun Kim, and all members of Flexible Devices and Metamaterials Laboratory in KAIST (Korea) for their support and

technical advice while I was staying in Daejeon. At the same time, I also sincerely thank Senior Lecturer Masuda Takashi for his kindly guidance and advices during my experiments in JAIST.

I also very much appreciate the helpful advice, technical help and discussions I had with Asst. Prof. Juan Paolo Soria Bermundo and Asst. Prof. Mami Fuji. Their advices and insightful comments make me study and understand more about the research.

And sincerely thanks to Ms. Yukiko Morita for her wonderful support and kindness during my study life in the lab. Also very thankful for the technical assistance and advice I received from Mr. Noritake Koike, Mr. Masahiro Fujihara, Mr. Syouhei Katao and Mr. Kazuhiro Miyake.

My sincere thanks also goes to all the members of Information Devices Science Laboratory for their help, assistance and encouragement, especially the thermoelectric device group's member Ms. Jenichi Clairvaux Escubio Felizco, Mr. Sihapitak Pongsakorn, Mr. Ikeguchi Yoku, for their advice and supporting.

Finally, I am very much thankful to my parents for their understanding encouragement, support caring and love. I am also thankful to relatives and friends for their support and love. Special thanks to Ms. Tong Wang, and Mr. Masaaki Furukawa.

Xudongfang Wang

01/07/2020